Gravity Waves in the Lower Atmosphere in Mountainous Regions and the Role of the Tropopause

Sonja Gisinger

München 2018

Gravity Waves in the Lower Atmosphere in Mountainous Regions and the Role of the Tropopause

Sonja Gisinger

Dissertation
an der Fakultät für Physik
der Ludwig–Maximilians–Universität
München

vorgelegt von
Sonja Gisinger
aus Bregenz

München, den 01.03.2018

Erstgutachter: Prof. Markus Rapp
Zweitgutachter: Prof. Martin Riese
Tag der mündlichen Prüfung: 15.05.2018

Have no fear of perfection - you'll never reach it.
—Salvador Dali (1904-1989)

Zusammenfassung

Die Hintergrundbedingungen in der Atmosphäre sind selten konstant und variieren sowohl zeitlich als auch räumlich. Das beeinflusst die Ausbreitung von atmosphärischen Schwerewellen und deren Implus- und Energietransport in der Atmosphäre. Im Bereich der unteren Atmosphäre (Troposphäre, untere Stratosphäre) finden sich ausgeprägte Dichte- und Temperaturänderungen vor allem in der unteren Troposphäre und an der Tropopause. Gebirgswellen breiten sich daher nicht nur, wie von der zweidimensionalen und linearen hydrostatischen Lösung der Bewegungsgleichungen beschrieben, vertikal direkt über dem Gebirge aus. Sie können an der Grenzschichtinversion in der unteren Troposphäre gefangen sein, wobei sie dann als Grenzflächenwellen bezeichnet werden (Vosper 2004, Sachsperger et al. 2015). Anhand von idealisierten Simulationen wird in dieser Arbeit gezeigt, dass Gebirgswellen auch an der Tropopauseninversion gefangen sein können, wenn die Inversionsstärke, welche durch die Änderung der potentiellen Temperatur über die Tropopause hinweg beschrieben wird, ausreichend groß ist. Damit wird die Gültigkeit der linearen Abschätzung zum Auftreten von gefangenen Wellen auch für die Tropopauseninversion bestätigt. Im Falles eines mit der Höhe konstanten Windes, muss die Stärke der Tropopauseninversion aufgrund der stabiler geschichteten Stratosphäre doppelt so groß sein wie für eine Inversion in der unteren Troposphäre. Wenn höhere Windgeschwindigkeiten vorherrschen, muss die Tropopauseninversion sogar noch stärker sein. Die horizontale Wellenlänge der Grenzflächenwellen reduziert sich mit zunehmender Stabilität oberhalb der Inversion. Des Weiteren zeigen die Simulationen, dass reflektierten Wellen stromabwärts des Gebirges in der Troposphäre existieren, obwohl der Scorer Parameter nicht mit der Höhe abnimmt. Ein mit der Höhe abnehmender Scorer Parameter ist die Voraussetzung für den klassischen Fall von gefangenen Wellen in der Troposphäre. Die Amplituden der reflektierten Wellen in der Troposphäre größer, wenn anstatt des normalen Übergangs von troposphärischer zu stratosphärischer Stabilität an der Tropopause eine Tropopauseninversion vorhanden ist. Darüber hinaus vergrößert sich die horizontale Wellenlänge der sich ausbreitenden Wellen, der Grenzflächenwellen und der reflektierten Wellen bei höheren Windgeschwindigkeiten.

Die Gegebenheiten in der realen Atmosphäre werden anhand umfangreicher Analysen der atmosphärischen Bedingungen während der DEEPWAVE Kampagne evaluiert. Die Kampagne fand im Südwinter 2014 in und um Neuseeland statt. Durch die Kombination von unterschiedlichen Datensätze und Diagnostiken werden die Eigenschaften der Hintergrundatmosphäre von der Troposphäre bis zur unteren Stratosphäre bestimmt. Die vorgefundenen Wetterregime und atmosphärische Zustände werden sowohl mit den klimatologischen Bedingungen als auch mit flugzeuggetragenen und bodengebundenen Schwerewellenbeobachtungen in Verbindung gesetzt. Hauptergebnisse dieser Analyse sind das dominante Auftreten von troposphärischem Blocking sowie südwestlicher Anströmung über Neuseeland in den Monaten Juni/Juli/August 2014. Der Subtropenjet befand sich oft südlich seiner klimatologischen Position auf

30° S und war meist in Wellenevents mit starker Anregung an den Südalpen involviert. Der Polarfrontjet sorgte typischerweise für eine moderate bis schwache Anregung der Gebirgswellen. Die variablen, mittels WRF simulierten, vertikalen Energieflüsse zeigen eine Abhängigkeit von der unterschiedlich stark ausgeprägten Tropopauseninversion. Die Tropopauseninversion spielt daher eine wichtige Rolle bei der Abschwächung von nach oben propagierenden Gebirgswellen.

Anhand von Radiosondendaten wird die Aktivität der Schwerewellen und deren Eigenschaften während DEEPWAVE bestimmt. Es zeigt sich, dass die Vertikalwindstörungen der Radiosondenaufstiege von Gebirgswellen, genauer gesagt nicht-hydrostatischen Gebirgswellen, dominiert werden. Auch die Trägheitsschwerewellen in Horizontalwindstörungen der Stratosphäre zeigen im Wesentlichen eine Verbindung zu den Gebirgswellen. Die Trägheitsschwerewellen in der Stratosphäre propagieren hauptsächlich nach oben, haben vertikale Wellenlängen von 2 bis 4 km und horizontale Wellenlängen von einigen hundert Kilometern. Die nicht-hydrostatischen Gebirgswellen zeichnen sich durch horizontale und vertikale Wellenlängen von einigen Zehnerkilometern und stromabwärtige Energieausbreitung aus. Obwohl Reflexion und Gefangensein von Gebirgswellen an der Tropopause mit den Radiosonden nicht direkt gemessen werden kann, zeigen sie vorherrschende Tropopausenbedingungen, welche zur Reflexion und wahrscheinlich auch zum Gefangensein der Gebirgswellen an der Tropopauseninversion geführt haben. Bei einer multiplen linearen Regression unter Einbeziehung der Anregungsbedingungen und der Stärke der Tropopauseninversion zeigt sich zumindest eine kleine Abhängigkeit der stratosphärischen Gebirgswellenaktivität in den Radiosondendaten von der Stärke der Tropopauseninversion. Außerdem, zeigt das Auftreten der nicht-hydrostatischen Gebirgswellen in der Stratosphäre, dass diese von der Troposphäre über die Tropopause hinweg in die Stratosphäre entweichen können.

Abstract

Background conditions in Earth's atmosphere are rarely constant, neither in time nor in space, which affects the propagation of atmospheric gravity waves and their way of distributing momentum and energy in the atmosphere. Changes of density and temperature in the lower atmosphere (troposphere and lower stratosphere) are most pronounced in the lower troposphere and at the tropopause. Mountain waves do not only propagate vertically above the mountains as described by the 2-dimensional, linear hydrostatic solution of the equations of motion. They can be trapped at boundary-layer inversions in the lower troposphere, i.e. interfacial waves (Vosper 2004, Sachsperger et al. 2015). This thesis shows by means of idealized numerical simulations that mountain waves can also be trapped on the tropopause inversion layer (TIL) if the strength of the inversion, which is defined as the change in potential temperature across the tropopause, is large enough. The applicability of the linear estimate of the existence of trapped mountain waves for the TIL can be confirmed. For vertically constant wind, the strength of the TIL must be twice as large as for inversions in the lower troposphere due to the larger stability of the stratosphere. The TIL must be even stronger for higher wind speed. The horizontal wavelength of the interfacial waves decreases with increasing stability above the inversion. Moreover, the simulations show that reflected waves exist downstream of the mountain in the troposphere even without a decrease of Scorer parameter with altitude, which is the classical condition for trapped waves in the troposphere. The amplitudes of the reflected waves are larger if a TIL is present at the tropopause compared to just a jump from tropospheric to stratospheric stability. In addition, horizontal wavelengths of propagating, interfacial, and reflected waves increase with increasing wind speed.

The situation in the real atmosphere is evaluated by means of a comprehensive analysis of the atmospheric conditions during the Deep Propagating Gravity Wave Experiment (DEEPWAVE) campaign. The campaign took place in the region of New Zealand in austral winter 2014. Different datasets and diagnostics are combined to characterize the background atmosphere from the troposphere to the lower stratosphere. How weather regimes and the atmospheric state compare to climatological conditions is reported upon and how they relate to the airborne and ground-based gravity wave observations is also explored. Key results of this analysis are the dominance of tropospheric blocking situations and low-level southwesterly flows over New Zealand during June/July/August 2014. The subtropical jet was frequently diverted south from its climatological position at 30° S and was most often involved in strong forcing events of mountain waves at the Southern Alps. The polar front jet was typically responsible for moderate and weak tropospheric forcing of mountain waves. A varying TIL is found to be connected to varying vertical energy fluxes in WRF model simulations and is, therefore, an important feature with respect to the attenuation of upward propagating mountain waves.

Gravity wave activity and properties during DEEPWAVE are computed from

radiosonde data. It is shown that vertical velocity perturbations from soundings are dominated by mountain waves, namely non-hydrostatic mountain waves. The inertia-gravity waves in the horizontal velocity perturbations in the stratosphere are also largely connected to mountain waves. The inertia-gravity waves in the stratosphere show dominant upward propagation of wave energy, vertical wavelengths of mainly 2 to 4 km, and horizontal wavelengths of some hundreds kilometers. The non-hydrostatic mountain waves have horizontal and vertical scales of tens of kilometers and downstream energy propagation. Although the radiosonde measurements do not allow to directly observe wave reflection and trapping of mountain waves at the tropopause, they revealed tropopausal conditions which should cause reflection and likely also allow for trapping on the TIL. Multiple linear regression, which includes low-level forcing and TIL strength, reveals at least a small dependence of the stratospheric mountain wave activity in the sounding data on the strength of the TIL. In addition, the occurrence of non-hydrostatic mountain waves in the stratosphere shows the propagation or leakage of these waves from the troposphere across the tropopause into the stratosphere.

Publications

Parts of the methods and results presented in this thesis have been published in the following articles:

Gisinger, S., A. Dörnbrack, V. Matthias, J. D. Doyle, S. D. Eckermann, B. Ehard, L. Hoffmann, B. Kaifler, C. G. Kruse, and M. Rapp, 2017:. Atmospheric Conditions during the Deep Propagating Gravity Wave Experiment (DEEPWAVE). *Mon. Weath. Rev.*, **145 (10)**, 4249–4275,doi:10.1175/MWR-D-16-0435.1.

S. Gisinger did the analyses of the low atmosphere (troposphere and tropopause region) and wrote the paper. A. Dörnbrack and V. Matthias did the analyses of the middle atmosphere. S. D. Eckermann provided NAVGEM reanalyses. B. Ehard and B. Kaifler conducted and provided lidar measurements and analyses. L. Hoffmann did the analyses of the AIRS data. C. G. Kruse did the WRF simulations. A. Dörnbrack, J. D. Doyle and M. Rapp contributed in structuring and writing the paper. A. Dörnbrack supervised the study.

Sections 3.1.2, 4.2 and parts of section 6 of this thesis are literal excerpts of the paper © Copyright 2017 AMS[1].

Dörnbrack, A., S. Gisinger, M. C. Pitts, L. R. Poole, and M. Maturilli, 2017: Multilevel cloud structures over Svalbard. *Mon. Weath. Rev.*, **145 (4)**, 1149–1159, doi:10.1175/ MWR-D-16-0214.1.

S. Gisinger did the analyses of the radiosonde data and contributed in writing the paper. A. Dörnbrack analysed and compared CALIOP and ECMWF data and wrote the paper. M. C. Pitts and L. R. Poole processed and provided the CALIOP data. M. Maturilli analysed the polar stratospheric clouds in the CALIOP measurements.

The approach used to analyse the radiosonde data in the paper is presented in Section 3.2.4 and applied on the DEEPWAVE sounding data in Section 4.3.1.

[1] © Copyright 2017 American Meteorological Society (AMS). Permission to use figures, tables, and brief excerpts from this work in scientific and educational works is hereby granted provided that the source is acknowledged. Any use of material in this work that is determined to be "fair use" under Section 107 of the U.S. Copyright Act or that satisfies the conditions specified in Section 108 of the U.S. Copyright Act (17 USC §108) does not require the AMS's permission. Republication, systematic reproduction, posting in electronic form, such as on a website or in a searchable database, or other uses of this material, except as exempted by the above statement, requires written permission or a license from the AMS. All AMS journals and monograph publications are registered with the Copyright Clearance Center (http://www.copyright.com). Questions about permission to use materials for which AMS holds the copyright can also be directed to permissions ametsoc.org. Additional details are provided in the AMS Copyright Policy statement, available on the AMS website (http://www.ametsoc.org/CopyrightInformation).

Contents

1 Introduction

1.1 Atmospheric Gravity Waves

Two fundamental elements for all wave motions in solids, liquids and gases are a physical restoring force and a medium for propagation (Lin 2007). The buoyancy force ("gravity") acts as restoring force on an air parcel vertically displaced from its initial position in a stably stratified atmosphere. Unable to stop at its equilibrium position on the way back, the air parcel starts to oscillate around this position (Fig. 1.1). An atmospheric gravity wave (GW), which may propagate through the atmosphere, is generated. Besides the buoyancy force, the Coriolis force due to Earth's rotation can act as an additional restoring force, which causes also a horizontal oscillation. The resulting mixed waves are called inertia-GWs (Lin 2007).

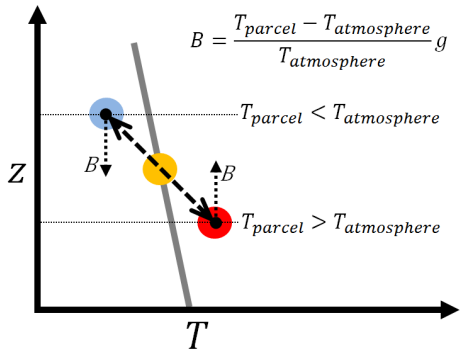

Figure 1.1: Schematic diagram of an oscillating air parcel in a stably stratified atmosphere, whose temperature changes with altitude as shown by the grey line. The temperature of the air parcel follows the dry adiabatic lapse rate $\Gamma_d \equiv \frac{g}{c_p} = -\left(\frac{\mathrm{d}T}{\mathrm{d}z}\right)_{dryparcel}$ (e.g., Eq. (3.52) Wallace and Hobbs 2006). Buoyancy (B) acts as restoring force and is calculated from the temperature (T) difference between atmospheric and air parcel temperature and the acceleration by gravity (g).

GWs are an important coupling mechanism between the lower and the middle and upper atmosphere. Propagating GWs transport momentum and energy and deposit them in regions where breaking and dissipation occurs. Moreover, even without GW breaking

direct GW-mean flow coupling ("transience") can be important (Bölöni et al. 2016). As such, GWs account for example for the well known upper mesospheric wind reversals as well as the cold polar summer mesopause and the warm winter stratopause (Dunkerton 1978, Lindzen 1981). So far, different sources for GWs in the troposphere have been identified, e.g., orography, convection, jets and fronts as well as secondary generation in the region of GW breaking (Smith 1979, Gill 1982, Baines 1995, Fritts and Alexander 2003, Sutherland 2010, Plougonven and Zhang 2014, Vadas et al. 2003). Breaking GWs cause turbulence, which could be a hazard to aviation in the troposphere and lower stratosphere (Sharman et al. 2012). The horizontal spatial scales of atmospheric GWs cover tens to hundreds of kilometers. According to linear theory, the intrinsic frequencies, i.e. the frequencies measured by an observer drifting with the mean flow, for vertically propagating GWs are limited by the Brunt-Väisälä frequency and the inertial (Earth) frequency (Nappo 2012).

"While we cannot see atmospheric GWs we can see the effects the waves have on the atmosphere" (Nappo 2012). In mountainous regions, the probably most prominent visible phenomena caused by GWs are lenticular and rotor clouds (Fig. 1.2a,b). Also polar stratospheric clouds (PSCs, Fig. 1.2c) can be caused or modified by orographic GWs (e.g., Dörnbrack et al. 2017b). Sometimes cirrus clouds reveal even smaller scale wave structures (Fig.1.2d). Wave structures in noctilucent clouds show the presence of GWs in the middle atmosphere at around 80 km altitude (Fig. 1.2e, e.g., Rapp et al. 2002).

Measurements systematically show GW activity in the middle and upper stratosphere and mesosphere but with varying intensity (e.g., Hines 1960, Chanin and Hauchecorne 1981, Weinstock 1996, Fritts and Alexander 2003, and references therein). Based on the properties of the GWs in this part of the atmosphere it is concluded that GWs are propagating upward from the troposphere and the tropopause region (Sato et al. 2009, Fritts et al. 2016). However, the atmospheric temperature and wind structure influences the propagation of GWs and alters their properties. The distance from the lower troposphere to the mesosphere is about 60 km in the vertical, where changes in wind and temperature occur (Eckermann 1995, Doyle and Jiang 2006, Eckermann et al. 2007). There are, for example, the tropopause as a discontinuity in stability, a wind maximum (jet) often occurring in its vicinity, or the stratospheric wind minimum at around 20 km altitude at mid-latitudes. Different measurement techniques can provide only information about GWs in a limited altitude range. Moreover, they are sensitive to particular parts of the GW spectrum, i.e. observational filter (Alexander 1998). Therefore, the tracking of GWs from the troposphere to the mesosphere by measurements is not straightforward. Currently much activity is going on to get a complete picture of the GW activity and distribution around the globe and to enhance the understanding of source and propagation processes. All this is necessary to adequately model and parameterize atmospheric GWs in weather and climate models.

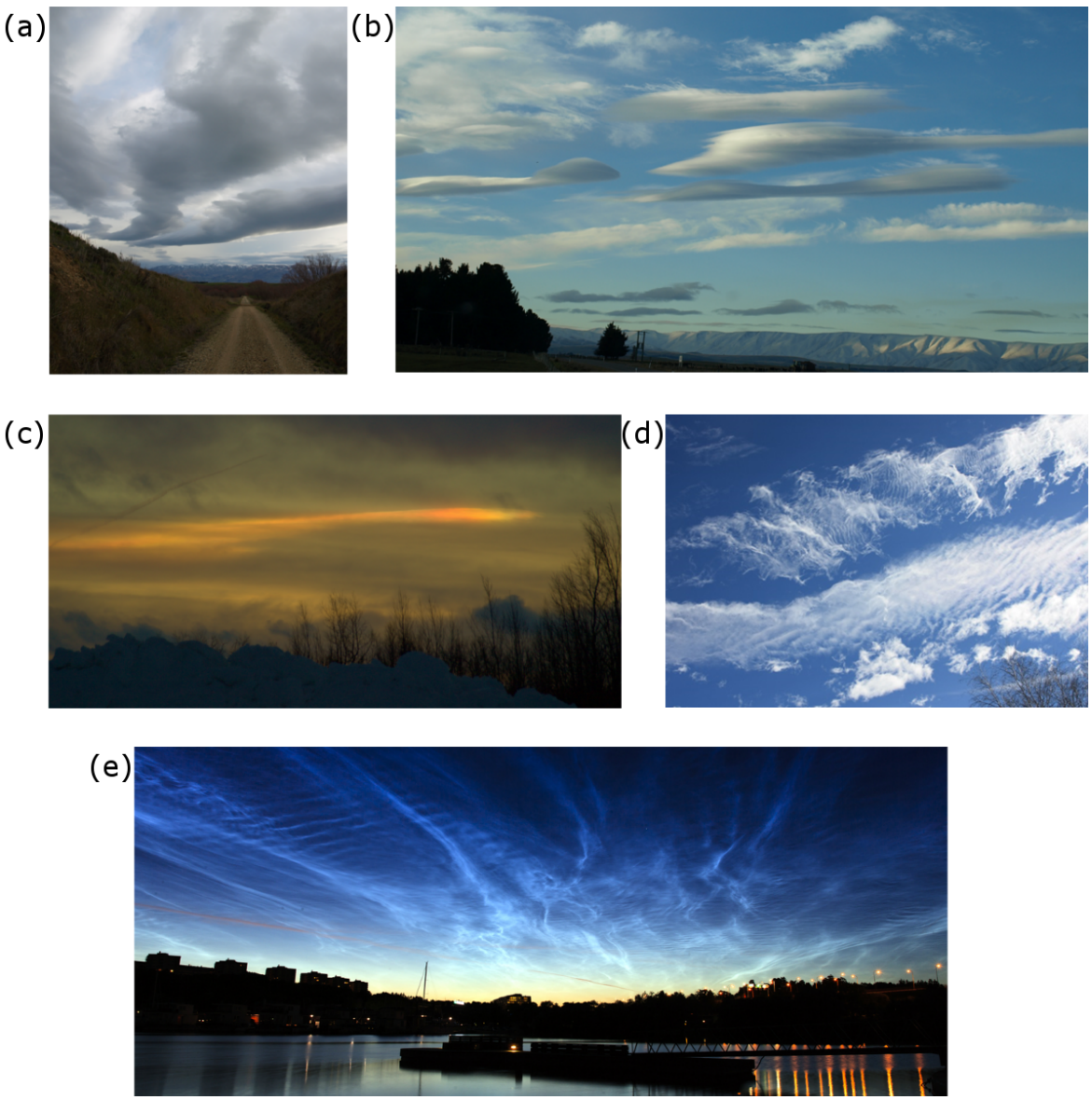

Figure 1.2: Visible phenomena influenced by GWs : (a) rotor and (b) lenticularis clouds over the Southern Alps of New Zealand (NZ), (c) PSCs over northern Scandinavia, (d) small scale structures in cirrus clouds over New Zealand (photo by B. Kaifler) and (e) wave structures in noctilucent clouds over Stockholm (photo by K. Cho, taken from Wikipedia)

1.2 Mountain Waves

Early studies dealing with flow and GW propagation behaviour over a hilly surface go back to the late 1930s (Küttner 1938, Queney 1948, Scorer 1949). Different mountain

wave (MW) regimes occur, which depend on background stability and wind conditions and horizontal wave scales(Lin 2007). Either a MW is able to propagate vertically or its amplitude decreases with altitude, i.e. the wave disturbance is evanescent. The latter is more likely if the horizontal wave scales are small, wind speed is high and/or the atmosphere is less stable. Vertically propagating waves are further separated into non-hydrostatic and hydrostatic MWs. Horizontal scales are clearly larger than vertical scales for hydrostatic MWs. The vertical pressure gradient force and the buoyancy force are roughly in balance (Lin 2007). The vertical acceleration can be ignored ($\frac{\mathrm{D}w'}{\mathrm{D}t} = 0$) in case of hydrostatic waves, but not in case of non-hydrostatic waves. Horizontal and vertical scales are similar for non-hydrostatic waves. 2-dimensional hydrostatic MWs which are not influenced by Coriolis force are found directly above the mountain (Lin 2007).

Since the works of Queney (1948) and Scorer (1949), different theoretical and numerical methods were used to study MW propagation in an atmosphere of vertically varying wind and stability. Those methods are ray tracing, determination of reflection and transmission coefficients, numerical solutions of the vertical structure equation for single wave components, analytical models, and asymptotic analysis (see Wurtele et al. (1987) and references therein). An important result of those follow-up investigations is that the stratospheric solution in a model taking into account a vertically varying background is not dominated by the classical solution of Queney (1948), but by reflected and downstream propagating (trapped) waves in the troposphere (Wurtele et al. 1987, Keller 1994). This makes the wave spectrum (i.e. wavelengths) being determined by the vertical varying wind and stability and not by the topography spectrum, which affects the relative amplitudes (Keller 1994, Ralph et al. 1997). Two sources of reflection for upward propagating waves in the lower atmosphere (troposphere and lower stratosphere) are the tropospheric wind shear and the discontinuity in stability at the tropopause (Wurtele et al. 1987). Models using equations based on the hydrostatic assumption do not allow for trapped, partially trapped, and non-hydrostatic waves propagating downstream. It was also found, that the longer wave modes of the trapped waves in the troposphere are not fully trapped but leak wave energy into the stratosphere (Wurtele et al. 1987, Keller 1994, Durran et al. 2015). The number of trapped modes, their ability to leak into the stratosphere, and the altitude where they contribute to the momentum budget considerably depends on the incoming flow, i.e. wind speed on the ridge (Georgelin and Lott 2001). If partially trapped waves are present a larger percentage of the total integrated momentum flux (Eliassen and Palm 1960) is contributed further downstream and not directly above the obstacle (Keller 1994). Fine scale structures in the atmosphere, such as sharp temperature inversions at the top of the boundary layer (Vosper 2004, Sachsperger et al. 2015) or in the mesosphere (Fritts et al. 2018) can be wave guides leading to trapped waves, which propagate horizontally on the inversions, i.e. interfacial waves. All those findings are in contrast to the fundamental characteristics of the hydrostatic approximation. They are the absence

of a mechanism which allows a wave to propagate horizontally and the consequent upward propagation of energy directly above the obstacle, no matter whether linear or non-linear and regardless of the generating terrain (Wurtele et al. 1996). It can be expected that weather and climate models which are based on the hydrostatic approximation miss a fundamental characteristic of the propagation of mountain waves in the real atmosphere, where stability and wind conditions vary with altitude. In this context, it seems reasonable to investiagte the possible existence of interfacial waves at the tropopause inversion layer (TIL) similar to their existence on an inversion in the troposphere. Moreover, it is necessary to investigate the mountain waves in the real atmosphere by means of measurements and how the findings match the depiction by linear theory.

So far, observational indications of GW behaviour in the tropopause region such as reflection and trapping are rare due to lack of observations below and above the tropopause. Using aircraft measurements, which were taken during the Terrain-Induced Rotor Experiment (T-REX, Grubišić et al. (2008)), Smith et al. (2008) were able to measure partial reflection of MWs at the tropopause for the first time. They computed momentum fluxes and the equipartition ratio of potential and kinetic GW energies at different flight altitudes. Using their linear model, they identified two levels of reflection, one at the altitude where the Scorer parameter changes due to changes in static stability and the other at the altitude with a discontinuity in wind speed but constant Scorer parameter. In addition, Smith et al. (2008) and Woods and Smith (2010) found trapped waves with a horizontal wavelength of about 15 km on the TIL during T-REX. Smith et al. (2008) and Woods and Smith (2010) regard the Sierra mountain range as an unlikely source for those 15-km waves. They do not expect those waves to reach the tropopause altitude from below because the background conditions caused a considerable evanescent decay. Instead, they suggest that those waves were generated by a nonlinear steepening process.

The measurement campaigns DEEPAVE (Deep Propagating gravity WAVe Experiment, Fritts et al. (2016)) in NZ and GW-LCYCLE 1 & 2 (Life Cycle of Gravity Waves) in Scandinavia were conducted between 2013 and 2016 and provide new comprehensive data to study GWs in the vicinity of the tropopause. Recent publications of Bossert et al. (2015), Kaifler et al. (2015), Pautet et al. (2016), Smith et al. (2016), Ehard et al. (2017), Kaifler et al. (2017), Bramberger et al. (2017), and Portele et al. (2018) focus on middle atmospheric wave response in ground-based and airborne lidar, airglow, mesospheric temperature, and aircraft insitu measurements during DEEPAVE. Smith and Kruse (2017) highlight the broad range of MWs triggered by the Alps of NZ. Their analyses of aircraft insitu measurements revealed non-hydrostatic MWs, which have horizontal wavelengths of 8-40 km, in vertical velocity measurements and larger scale MWs, which have horizontal wavelengths of 200-400 km, in the horizontal wind and temperature measurements in the lower stratosphere. Similar MWs scales were found by Witschas et al. (2017) and Wagner et al. (2017) in airborne lidar measurements and

WRF model simulations in the troposphere and lower stratosphere over Scandinavia during GW-LCYCLE.

Furthermore, radiosondes provide point-measurements, which can be analyzed for GWs, from the surface up to 35 km. They are released at places all over the world on daily basis and are used in intensive measurements campaigns such as DEEPAVE and GW-LCYCLE 1 & 2. Therefore, different analysis methods were developed in the past to derive GW properties from radiosonde measurements (Lane et al. 2000, Vincent et al. 1997, Eckermann 1996, Zink and Vincent 2001, Murphy et al. 2014, Vincent and Alexander 2000, Geller and Gong 2010). Gravity wave climatologies were created for various places (e.g., Gong and Geller 2010, Guest et al. 2000, Murphy et al. 2014, Yoshiki and Sato 2000). Here, radiosonde measurements of the DEEPWAVE campaign are used to study GWs in the troposphere and the stratosphere. The focus is on MWs and the influence of the tropopause on MW propagation.

In the altitude range from above the maximum flight altitude of the aircraft (approx. 11 km for the DLR Falcon and 13 km for the NSF/NCAR Gulfstream V (GV)) to where the ground based lidar measurements started (approx. 25 to 30 km), the only measurements came from the radiosondes. Therefore, radiosondes not only cover the altitude range in the troposphere closest to the source of the MWs but also an adequate altitude range above the tropopause region in the stratosphere. This qualifies radiosondes as a tool to study GWs by means of their activity and propagation in troposphere and stratosphere and across the tropopause.

1.3 Goals and Hypothesis

Atmospheric GWs have been studied extensively during the last decades. Web of Science[2] core collection database, which goes back to 1970, lists 6223 scientific papers containing the term "gravity wave(s)" in the title and 863 papers containing also "atmosphere/atmospheric". 463 papers contain the term "mountain wave(s)" and 95 papers contain the term "orographic wave(s)" in the title. The papers contain a huge amount of theoretical and observational studies. But still, improvements of GW parametrization schemes in global circulation models need more detailed observational information and constraints on the properties of GWs, which are radiated from various tropospheric sources and reach the middle atmosphere (McLandress and Scinocca 2005, Alexander et al. 2010). The main goal of this thesis is to gain and increase the knowledge about GWs in mountainous regions in Earth's real (not idealized) atmosphere. As already mentioned above, the target of interest are MWs in the lower atmosphere (troposphere and lower stratosphere) including the tropopause, which is an interesting region with respect to wave propagation due to change in stability and vertical shear

[2] http://apps.webofknowledge.com, accessed August 2017

of the horizontal wind (Wurtele et al. 1987, Keller 1994). So far, associated processes such as wave reflection, trapping, and horizontal propagation are not resolved by state of the art numerical weather forecast and climate models. Those processes can be expected to gain influence due to the ongoing increase of model resolution and more distinct prescription of the sources of stratospheric GWs. Therefore, it not only is necessary to investigate wave propagation from the troposphere into the stratosphere from a theoretical point of view but also to evaluate the conditions and the GW behaviour in the real atmosphere by means of measurements. Moreover, climate models currently simulate too cold stratospheric winter and spring temperatures compared to observations in the Southern Hemisphere high latitudes. This "cold-pole bias" is believed to be largely caused by a missing gravity wave drag in the Southern Hemisphere. Garcia et al. (2017) showed that changes in the orographic GW fluxes ameliorate the Southern Hemisphere cold pole bias in the Whole Atmosphere Community Climate Model and highlight the crucial role of orographic gravity waves, especially in the Southern Hemisphere. Therefore, "careful examination of observational evidence and model performance will be required to establish which gravity wave sources are dominant in the real atmosphere" (Garcia et al. 2017).

In this thesis, the topics are addressed by combining theory and idealized simulations with findings from operational model analyses and measurements for the region of NZ, which is a hot spot for stratospheric GWs in the Southern Hemisphere. Based on the expected dominant contribution of MWs mainly from the Southern Alps and the presence of a TIL in this region at mid-latitudes, the following two hypotheses are investigated:

- Measurements of GWs by radiosondes in a mountainous region can be uniquely assigned to orographic sources
- The impact of the tropopause on MW propagation as predicted by theory can be confirmed by radiosonde measurements

The structure of the thesis is as follows. The next section 2 gives an overview of GW propagation in the troposphere and low stratosphere based on the linear theory of GWs. Section 3 introduces the numerical models, the dataset of radiosonde measurements, and the methods, which are used to analyse the radiosonde measurements for atmospheric GWs. In the first part of section 4, idealized numerical simulations, which evaluate the impact of the tropopause on MW propagation and the occurrence of interfacial waves at the TIL under well defined conditions, are presented. Then, the second part of section 4 leaves the idealized world behind and gives a comprehensive overview of the atmospheric conditions which prevailed during DEEPWAVE. This includes the tropospheric circulation and forcing conditions as well as the tropopause region (TIL, tropopause jets). In the last part of section 4, GW characteristics are determined from radiosonde measurements during DEEPAVE. The results of section 4 are then used

in section 5 to investigate and discuss the two hypotheses of this thesis. Section 6 summarizes the findings and conclusion. A short outlook is given in section 7.

2 Theory

2.1 Wave Propagation

Atmospheric GWs are seen as perturbations in wind, (potential) temperature, pressure and density (u', v', w', T', θ', p', ρ') with respect to a background state (U, V, T_0, θ_0, ρ_0). A general GW solution can be derived for the linearized form of the fundamental conservation equations:

$$\frac{Du'}{Dt} + w'\frac{\partial U}{\partial z} - fv' + \frac{\partial}{\partial x}\left(\frac{p'}{\rho_0}\right) = 0, \tag{2.1}$$

$$\frac{Dv'}{Dt} + w'\frac{\partial V}{\partial z} + fu' + \frac{\partial}{\partial y}\left(\frac{p'}{\rho_0}\right) = 0, \tag{2.2}$$

$$\frac{Dw'}{Dt} + \frac{\partial}{\partial z}\left(\frac{p'}{\rho_0}\right) - \frac{1}{H}\left(\frac{p'}{\rho_0}\right) + g\frac{\rho'}{\rho_0} = 0, \tag{2.3}$$

$$\frac{D}{Dt}\left(\frac{\theta'}{\theta_0}\right) + w'\frac{N^2}{g} = 0, \tag{2.4}$$

$$\frac{D}{Dt}\left(\frac{\rho'}{\rho_0}\right) + \frac{\partial u'}{\partial x} + \frac{\partial v'}{\partial y} + \frac{\partial w'}{\partial z} - \frac{w'}{H} = 0, \tag{2.5}$$

$$\frac{\theta'}{\theta_0} = \frac{1}{c_s^2}\left(\frac{p'}{\rho_0}\right) - \frac{\rho'}{\rho_0}, \tag{2.6}$$

(Fritts and Alexander 2003). $\frac{D}{Dt}$ is the linearized form of the total time derivative,

$$\frac{D}{Dt} = \frac{\partial}{\partial t} + U\frac{\partial}{\partial x} + V\frac{\partial}{\partial y}, \tag{2.7}$$

t is time, f is Coriolis parameter, H is density scale height, c_s is speed of sound, and N is the Brunt-Väisälä frequency (Fritts and Alexander 2003).

The wave solution for the perturbations in a non-Boussinesq fluid (i.e. taking into

account the decrese of ρ with altitude) reads

$$u' = A_u \cdot \exp[i(kx + ly + mz - \omega t) + \frac{z}{2H}], \tag{2.8}$$

$$v' = A_v \cdot \exp[i(kx + ly + mz - \omega t) + \frac{z}{2H}], \tag{2.9}$$

$$w' = A_w \cdot \exp[i(kx + ly + mz - \omega t) + \frac{z}{2H}], \tag{2.10}$$

$$\frac{T'}{T_0} \approx \frac{\theta'}{\theta_0} = A_\theta \cdot \exp[i(kx + ly + mz - \omega t) + \frac{z}{2H}], \tag{2.11}$$

$$\frac{p'}{\rho_0} = A_p \cdot \exp[i(kx + ly + mz - \omega t) + \frac{z}{2H}], \tag{2.12}$$

where A_u and A_v are amplitudes of the horizontal wind components, A_w is the amplitude of the vertical wind component, A_θ is the potential temperature amplitude, A_p is the pressure amplitude, k and l are horizontal wavenumbers, and m is the vertical wavenumber. $\omega = \Omega + kU + lV$ is the ground-based frequency which is the intrinsic wave frequency (Ω) Doppler shifted by the background wind (U, V) (Fritts and Alexander 2003). Vertical velocity perturbations are denoted as w in the following for consistency with Lane et al. (2000). w' is used for vertical velocity perturbations after removing the effect of the background density on its value (Lane et al. 2000).

The dispersion relation of atmospheric GWs relates their intrinsic frequency to their spatial scales and to the background atmosphere and is given by

$$m^2 = \frac{(k^2 + l^2)(N^2 - \Omega^2)}{\Omega^2 - f^2} - \frac{1}{4H^2} \tag{2.13}$$

in a rotating frame (Fritts and Alexander 2003). Based on the intrinsic frequency, the spectrum of atmospheric GWs can be separated into low frequency (inertia-GWs, $\Omega \to f$) and medium ($N >> \Omega >> f$) to high frequency ($\Omega \to N$) GWs (Fritts and Alexander 2003). For low frequency GWs and using Boussinesq approximation (i.e. assuming ρ to be constant except in the buoyancy term $g\frac{\rho'}{\rho_0}$), the dispersion relation simplifies to

$$m^2 = \frac{N^2 k_h^2}{\Omega^2 - f^2}, \tag{2.14}$$

where $k_h^2 = k^2 + l^2$ is the horizontal wave number (Vincent and Alexander 2000). It is defined that Ω is always positive. The hodograph (u' plotted against v') describes an ellipse for a monochromatic inertia-GW. Figure 2.1a shows a 2-dimensional, upward propagating hydrostatic inertia-GW packet and Figure 2.1b a corresponding hodograph.

The phase of atmospheric GWs propagates with the phase speed and into the direction of the wave number vector (Fig. 2.1a). The intrinsic horizontal phase speed is given

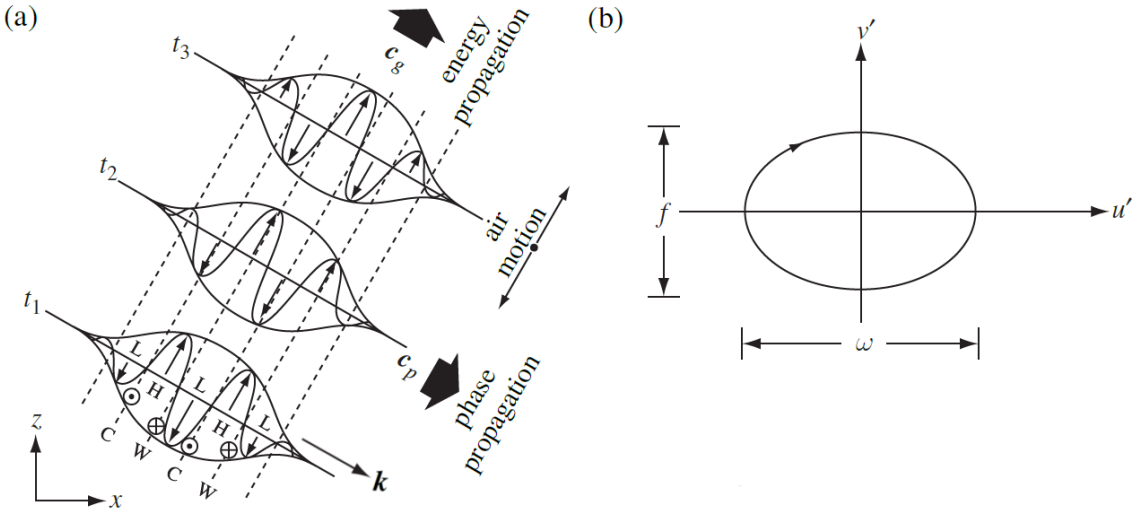

Figure 2.1: (a) Propagating hydrostatic inertia-GW packet ($m < 0$, $k > 0$, $l = 0$, $U = 0$, $\Omega = \omega > 0$, $f > 0$). The phase of the wave propagates with the phase speed and the wave energy with the group velocity. Symbols H and L denote the perturbation high and low pressures and W and C denote the warmest and coldest regions for the wave at time t_1. **k** shows the direction of the wave number vector. Meridional perturbations (v') are shown by arrows into or out of the page. (b) Hodograph of a hydrostatic inertia-GW showing an ellipse with the ratio of the major to the minor axes being ω/f and which rotates anticyclonically with height for upward energy propagation. Figure taken from Lin (2007). Copyright © Cambridge University Press 2007.

by

$$c_{ih} = \frac{\Omega}{k_h} \tag{2.15}$$

(e.g., Vincent et al. 1997). The horizontal wind must be taken into account for the ground-based horizontal phase speed. The ground-based horizontal phase speed is then given by

$$c_h = \frac{\omega}{k_h} = \frac{\Omega + kU + lV}{k_h}. \tag{2.16}$$

In contrast to the intrinsic phase speed, the ground-based phase speed can also have negative values, which means the ground-based phase speed is against the direction of the intrinsic phase speed. This is the case if the wind along the horizontal wave number vector is of opposite sign and larger than the horizontal intrinsic phase speed. The magnitude of the ground-based horizontal phase speed can also be expressed with respect to the wave's horizontal propagation direction ϕ and the background wind direction α (Murphy et al. 2014). A value of 180 degrees must be added if α is the

"wind-from direction". It follows

$$c_h = \frac{\Omega}{k_h} + \sqrt{U^2 + V^2}\cos(\alpha + 180 - \phi), \tag{2.17}$$

where $U_{kh} = \sqrt{U^2 + V^2}\cos(\alpha + 180 - \phi)$ gives the wind speed along direction of phase propagation (Fig. 2.2). α and ϕ are in degrees clockwise from North. It can be shown that Eq (2.17) is equal to Eq (2.16) when the relationship $\cos(a - b) = \cos(a)\cos(b) + \sin(a)\sin(b)$, the expressions $k = k_h \sin(\phi)$ and $l = k_h \cos(\phi)$, and $U = \sqrt{U^2 + V^2}\sin(\alpha + 180)$ and $V = \sqrt{U^2 + V^2}\cos(\alpha + 180)$ are considered.

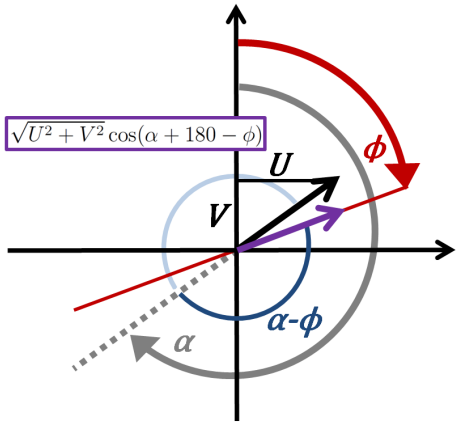

Figure 2.2: Angles of direction of phase propagation (ϕ) and "wind-from direction" (α) with the corresponding wind vector $[(U, V)]$. Purple arrow shows the wind speed in direction of phase propagation.

The intrinsic vertical phase speed is given by

$$c_{iz} = \frac{\Omega}{m} \tag{2.18}$$

(Murphy et al. 2014). The vertical phase speed is negative for downward phase propagation. This is realized by the definition that m is negative for downward phase propagation (Fig. 2.1a). The ground-based vertical phase speed is also influenced by the horizontal wind and is given by

$$c_z = \frac{\Omega + kU + lV}{m}. \tag{2.19}$$

As for the horizontal phase speed, the ground-based vertical phase speed can be of opposite sign compared to the intrinsic phase speed. This happens for the same conditions as for the horizontal phase speed, i.e. if the wind along the horizontal wave number vector is of opposite sign and larger than the horizontal intrinsic phase speed.

There is no influence of the vertical wind since its mean value is assumed to be zero. The ground-based vertical phase speed can be expressed by means of ϕ and α

$$c_z = \frac{\Omega}{m} + \frac{k_h\sqrt{U^2+V^2}\cos(\alpha+180-\phi)}{m}. \tag{2.20}$$

Eqs (2.17) and (2.20) reveal that the ground-based phase speeds are equal to the intrinsic phase speeds when the background wind direction is normal to the direction of horizontal wave propagation, i.e. the background wind in the direction of wave propagation (and hence the Doppler shift) is zero. The ground-based phase speeds become zero (stationary waves) when the background wind component along the direction of horizontal wave propagation is of the same magnitude and of opposite direction as the intrinsic horizontal phase speed.

The energy propagation of GWs follows the group velocity (Nappo 2012). The zonal, meridional, horizontal, and vertical ground-based group velocities $[(\frac{\partial\omega}{\partial k}, \frac{\partial\omega}{\partial l}, \frac{\partial\omega}{\partial m})]$ for inertia-GWs are given by

$$c_{gx} = \frac{kN^2}{\Omega m^2} + U, \tag{2.21}$$

$$c_{gy} = \frac{lN^2}{\Omega m^2} + V, \tag{2.22}$$

$$c_{gh} = \sqrt{c_{gx}^2 + c_{gy}^2}, \tag{2.23}$$

$$c_{gz} = -\frac{\Omega^2 - f^2}{\Omega m} \tag{2.24}$$

(Murphy et al. 2014). The sign of c_{gz} is positive for negative m and opposite to c_{iz}, i.e. an upward (downward) energy propagation corresponds to downward (upward) phase propagation (Eq. (2.18), Fig. 2.1a).

The horizontal ground-based group velocity and the vertical group velocity of medium to high frequency waves ($\Omega \to N$) read

$$c_{gh}(z) = U_{kh}(z) + \frac{k_h}{|k_h|}\frac{N(z)m(z)^2}{(k_h^2+m(z)^2)^{3/2}} \tag{2.25}$$

$$c_{gz}(z) = \frac{-|k_h|N(z)m(z)}{(k_h^2+m(z)^2)^{3/2}} \tag{2.26}$$

(Fritts and Alexander 2012). As already mentioned for the intrinsic frequency (Eq. (2.27)), the sign for k_h is opposite to $U_{kh}(z)$ for stationary waves and c_{gh} is always smaller than $U_{kh}(z)$.

The intrinsic frequency Ω of stationary MWs ($\omega = 0$) is related to the horizontal wavenumber via the background wind speed

$$\Omega(z) = -k_h U_{kh}(z). \tag{2.27}$$

The sign of the wind speed along the direction of phase propagation (U_{kh}) is always opposite to k_h to comply stationarity of the waves and to always lead to positive values of Ω. The vertical wavenumber m depends on the background conditions

$$m(z)^2 = \ell(z)^2 - k_h^2, \tag{2.28}$$

where ℓ is the Scorer parameter which is defined as

$$\ell(z)^2 = \frac{N(z)^2}{U_{kh}(z)^2} - \frac{\partial^2 U_{kh}(z)/\partial z^2 + \partial U_{kh}(z)/\partial z/H}{U_{kh}(z)} - \frac{1}{4H^2} \tag{2.29}$$

in a non-Boussinesq fluid with vertical shear (Lane et al. 2000). The Scorer parameter is part of the linearized version of the Taylor-Goldstein equation

$$\frac{d^2\hat{w}}{dz^2} + \underbrace{\left(\ell^2 - k^2\right)}_{m^2}\hat{w} = 0, \tag{2.30}$$

with $w' = \hat{w}\exp(ikx)$ (e.g., Eq. (2.36) in Nappo (2012) with the condition of stationarity (Eq. (2.27)) included to describe stationary MWs). The mountain must in some way exert a force against the atmospheric flow, i.e. MW/GW drag, in oder to allow the waves remaining stationary (Lin 2007).

The behaviour of MWs in the atmosphere is linked to background wind and stability conditions, which are summarized in the Scorer parameter (Scorer 1949). In a Boussinesq fluid and ignoring vertical changes of the background wind, the Scorer parameter can be approximated by

$$\ell^2 \approx \frac{N^2}{U_{kh}^2}, \tag{2.31}$$

where N is Brunt-Väisälä frequency

$$N = \sqrt{\frac{g}{\theta}\frac{\mathrm{d}\theta}{\mathrm{d}z}}, \tag{2.32}$$

g is the acceleration by gravity and θ is potential temperature

$$\theta = T\left(\frac{p_0}{p}\right)^{0.286}, \tag{2.33}$$

where p_0 is reference pressure, i.e. 1000 hPa. In a two layer problem the linearized, 2-dimensional and steady state equation of motion has a trapped wave solution for

$$\ell_L^2 - k^2 > 0, \tag{2.34}$$

$$\ell_U^2 - k^2 < 0, \text{ and} \tag{2.35}$$

$$\ell_L^2 - \ell_U^2 > \frac{\pi^2}{4h^2}, \tag{2.36}$$

where ℓ_L and ℓ_U are the Scorer parameter of the lower and upper layer (Fig. 2.3), respectively, k is the horizontal wavenumber and h is the depth of the lower layer (Scorer 1949). The solution of the Taylor-Goldstein equation (Eq. 2.30) is a vertically propagating wave ($\ell > k$) in the lower layer and an evanescent flow ($\ell < k$) in the upper layer (Lin 2007). The wavenumber (wavelength) separating these two regimes is $k_c = \ell$ ($\lambda_c = 2\pi/\ell$), i.e. the critical horizontal wavenumber (wavelength). The depth of the layer where a trapped mode is evanescent is essential for leakage of wave energy of a trapped mode into the stratosphere (Georgelin and Lott 2001). The vertical scale height over which waves decay depends on their e-folding scale

$$e_{scale} = (k^2 - \ell^2)^{-1/2}, \tag{2.37}$$

which is smaller for short waves than for longer waves (Durran et al. 2015). For example, for $\ell^2 = 10^{-7}$ m^2 (constant $U_{kh} = 30$ m s^{-1} and $N = 0.01$ s^{-1}) the e-folding scale is 1.8 km for a wave of 10 km horizontal wavelength and 6.7 km for a wave of 18 km horizontal wavelength. If the depth of the evanescent layer is well below this e-folding scale, wave energy more likely leaks into the stratosphere (Georgelin and Lott 2001).

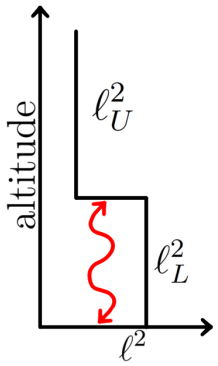

Figure 2.3: Vertical profile of the Scorer parameter showing smaller values in the lower layer (ℓ_L^2) than in the upper layer (ℓ_U^2). For this two layer problem the linearized, 2-dimensional and steady state equation of motion has a trapped wave solution.

The findings mentioned above are based on linear solutions of the equations of motion. However, the linear solution become invalid above some critical value of the non-dimensional mountain height. The non-dimensional mountain describes the ratio between the height of the obstacle h_0 and the horizontal wind speed V_H against the obstacle

$$h^* = \frac{Nh_0}{V_H}. \tag{2.38}$$

Wurtele et al. (1996) call this the paradox of lee-wave theory: "The weaker the flow against the obstacle, the more non-linear the disturbance". Moreover, non-linearity

likely is important because of the high mountains present on Earth. The flow response is controlled by the non-dimensional mountain height and four regimes are identified in case of hydrostatic MWs : (I) flow without wave breaking aloft and upstream blocking ($h^* \leq\sim 0.89$), (II) flow with wave breaking aloft and no upstream blocking ($\sim 0.89 < h^* \leq\sim 1.1$), (III) flow with wave breaking aloft and upstream blocking but where wave breaking occurs first ($\sim 1.1 < h^* \leq\sim 1.7$), and (IV) flow with wave breaking aloft and upstream blocking but where blocking occurs first ($\sim 1.7 < h^* \leq\sim 3.3$) (Lin 2007). However, analyzing mountain waves by means of linear theory can be justified to a certain degree by the fact that in a Boussinesq fluid and for rather vertically constant wind and stability any solution of the linearized equations is also a solution of the non-linear equations (see Wurtele et al. (1996) and references therein).

In addition, stationarity is assumed in MW analysis because the obstacle is fixed in time and space. However, wind speed and therefore the forcing of MWs is rarely constant in time. This causes MWs to evolve over time in response to changing upstream conditions and it appears that this non-stationarity, i.e. changing wavelength and amplitudes, is common (Ralph et al. 1997, Portele et al. 2018). In this context, the term intermittency describes this variability and gives the fraction of time during which significant forcing exists (Nastrom and Fritts 1992). When measurements are analyzed and e.g., MW drag from aircraft measurement is determined, it is necessary to identify time intervals of sufficient stationary conditions to avoid errors introduced by temporal changes of the wave structure (Ralph et al. 1997).

For a comparison between measurement and model results, Georgelin and Lott (2001) highlight five origins of the discrepancy between the MW drag by parameterizations and measurements by airplane. Those five points are

- unsteady nature of waves due to time variations of the incident flow,
- downstream transfer of momentum by trapped waves or simply the fact that measurements are taken over a finite distance,
- the momentum flux leakage that occurs through the lateral direction when the waves are three-dimensional,
- for real and high mountains, the low level flow goes around the mountain rather than over it and a large part of the drag is related to low level flow deceleration rather than to wave emission, and
- dissipation in the boundary layer and breaking at low level

(Georgelin and Lott 2001). They largely are a summary of the different factors which influence the flow characteristics and limit the applicability of estimates based on assumptions such as hydrostatic approximation, stationarity, linearity, and 2-dimensionality.

2.2 Inversion Effects on Mountain Waves

Fine-scale structures in the troposphere such as sharp temperature inversions can have significant influence on the GW and near-surface wind structure (see Vosper (2004) and references therein). Numerical experiments for the middle atmosphere revealed inter alia reflection and trapping of gravity waves in the vicinity of a mesosphere inversion layer, which are characterized by a moderate static stability enhancement and a layer of weaker static stability above (Fritts et al. 2018). For idealized 2-dimensional cases, Vosper (2004) found that the presence of a sharp temperature inversion in the troposphere influences the occurrence of phenomena such as lee-wave rotors, hydraulic jumps, and wave breaking. An inversion in the troposphere (e.g., at the top of the boundary layer) can be a waveguide for trapped waves which propagate downwind of the mountain. Conditions for which those trapped waves form and their horizontal wavelengths are well predicted by linear theory (Sachsperger et al. 2015). However, the wave amplitude is seriously underestimated if the horizontal wavelength is significantly less than the mountain length scale, i.e. for broad mountains (Vosper 2004). In addition, such temperature inversions can isolate the stably stratified, cross barrier flow aloft the inversion from the underlying terrain and build a so called "virtual topography", which is smoother and less steep than the real topography and cause a different flow response (Armi and Mayr 2015).

Four possibilities of MW propagation in dependency of the background conditions can be summarized from former studies of Scorer (1949), Wurtele et al. (1987), Keller (1994) and Vosper (2004). With focus on inversions and vertically constant or increasing wind speed and not accounting for decreasing wind speed and critical levels, those possibilities are:

(1) vertical propagation and no trapping, i.e. jump from neutral to higher static stability without inversion and with vertically constant wind speed (Fig. 2.4a)

(2) full trapping, i.e. constant static stability and infinitely increasing wind speed (Fig. 2.4b)

(3) partial trapping and leakage, i.e. jump to higher static stability without inversion and with increasing wind speed (Fig. 2.4c)

(4) trapping on the inversion, i.e. jump from neutral to higher static stability with an inversion and vertically constant wind speed (Fig. 2.4d)

The concept of changing wave behaviour according to the Scorer parameter (Eq. (2.29)) builds the backbone of those considerations. A critical horizontal wavenumber above which wave characteristics change from propagating to evanescent can be calculated from the Scorer parameter (cf. Eqs.(2.34) and (2.35)). Possibility (4), i.e. trapping on the inversion below a stably stratified layer is also known as forced interface waves at the

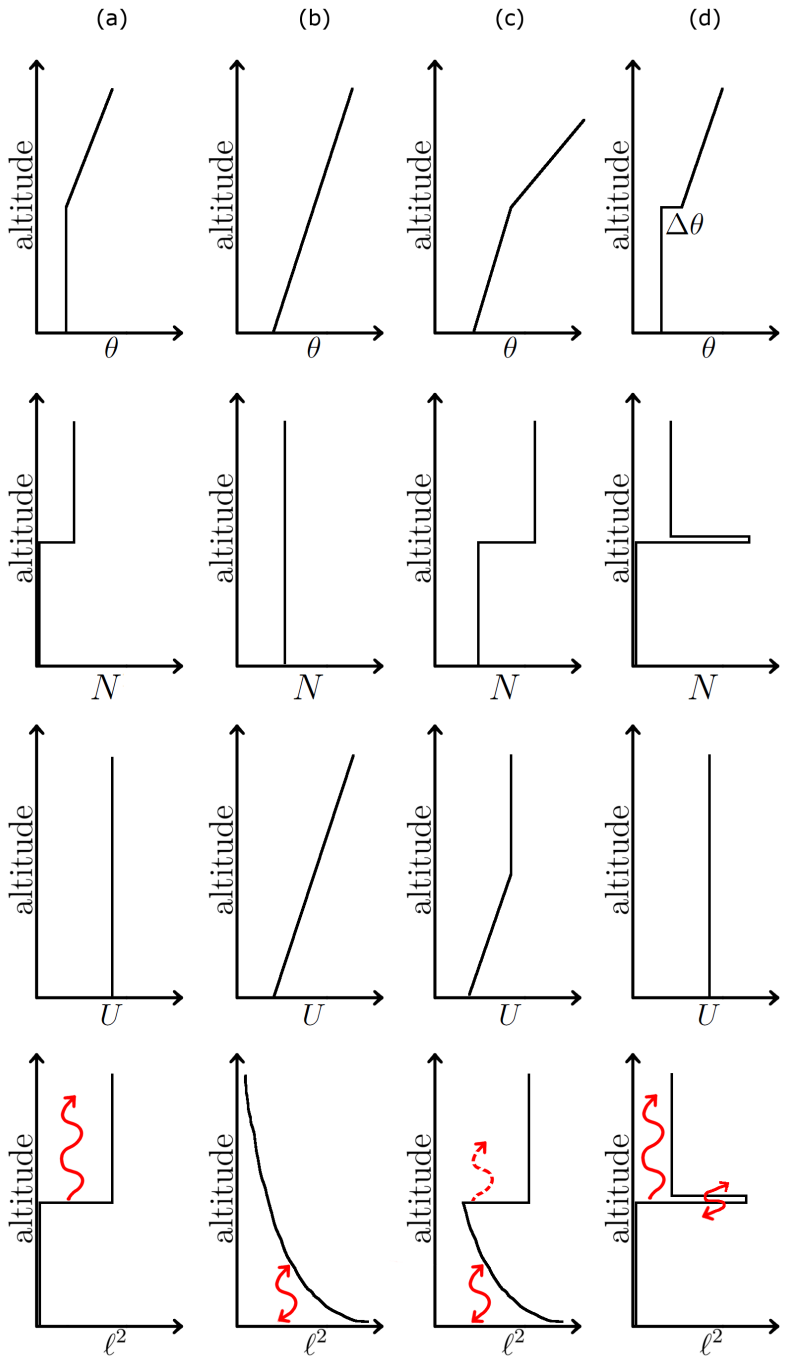

Figure 2.4: Profiles of (first row) potential temperature, (second row) Brunt-Väisälä frequency (Eq. (2.32)), (third row) horizontal wind speed and (fourth row) resulting Scorer parameter approximated by N^2/U^2 for (a) propagating waves above the neutral layer (Vosper 2004), (b) fully trapped waves (Wurtele et al. 1987, Keller 1994), (c) partial trapping and leakage (Wurtele et al. 1987, Keller 1994) and (d) trapped waves on an inversion (Vosper 2004).

discontinuity of potential temperature. In the case of a marine atmospheric boundary layer, it may be more appropriate to interpret the trapped lee waves, which create lee-wave cloud patterns, as interfacial waves rather than as classical trapped lee waves, which are created by decreasing Scorer parameter with altitude (Sachsperger et al. 2015). Since the tropopause itself is a discontinuity of potential temperature it seems reasonable to consider the possible existence of interfacial waves on the tropopause similar to their existence on an inversion in the troposphere.

The impact of an inversion at the top of a neutral layer in the troposphere on the wave behaviour was comprehensively studied with 2-dimensional numerical simulations ($V = 0$) and linear theory by Vosper (2004). In section 4.1 of this thesis, it is investigated if those findings for an inversion in the troposphere can be easily transferred to the TIL. Figure 2.5 (taken from Birner (2006)) shows averaged profiles of temperature and Brunt-Väisälä frequency squared representative for northern hemispheric mid-latitudes. The characteristic shape of the TIL is missing in the U.S. standard atmosphere and only revealed when a tropopause-based averaging method is used (Birner 2006). Based on linear theory and in accordance with the numerical simulations, the Froude number

$$F_i = \frac{U}{\sqrt{g z_i \Delta\theta/\theta}} \tag{2.39}$$

required for trapping to occur is

$$F_i^2 \leq \tanh(Z)/Z, \tag{2.40}$$

where $Z = \frac{N z_i}{U}$, U is the horizontal wind speed ($V = 0$), $\Delta\theta$ is the strength of the inversion, and z_i is the altitude of the inversion (Vosper 2004). The Froude number relates the flow speed to the speed of long-wavelength interfacial waves on the inversion in a stationary fluid when the stratification above is neutral. The parameter Z relates the inversion height to the vertical wavelength of hydrostatic mountain waves in the upper layer (Vosper 2004). The physical explanation for the trapping condition is that waves with horizontal wave numbers smaller than N/U are able to propagate freely in the vertical above the inversion and thus no trapping mechanism exists (Vosper 2004). For fixed values of N and U, an increase of z_i leads to an increase of Z and to a decrease of the ratio of hill height to the altitude of the inversion (h_0/z_i) for fixed h_0. For $U = 20$ m s^{-1} and $N = 0.02$ s^{-1}, which is typical for the stratosphere, and $z_i = 10$ km trapping occurs for $F_i^2 \leq 0.1$. If θ of the neutral lower layer is assumed to be 288 K, $\Delta\theta$ must be at least ≈ 12 K for trapping to occur. This is twice as large as for an inversion in the troposphere where $N = 0.01$ s^{-1}.

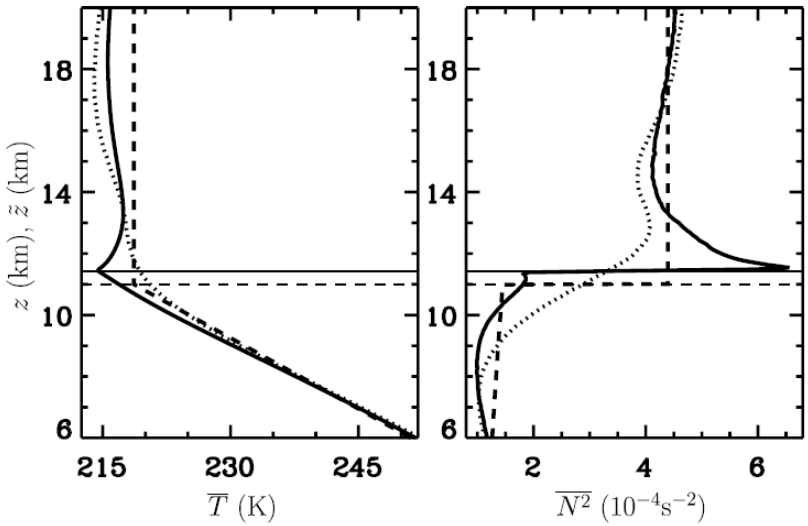

Figure 2.5: Averaged profiles of temperature (left) and buoyancy frequency squared (right) representative for northern hemispheric mid-latitudes. Dotted lines indicate sea level based average, solid lines indicate tropopause-based average, and dashed lines indicate profiles of the U.S. standard atmosphere at 45° N. Horizontal lines denote corresponding tropopause altitude. Figure taken from Birner (2006).

3 Data and Methods

3.1 Numerical Models

3.1.1 EULAG

EULAG[3] is a multi-scale computational model for the simulation of geophysical flows. It provides at least second-order accuracy in time and space (Prusa et al. 2008). EULAG solves the governing equations of motion either in an EUlerian or a LAGrangian form. Here, the non-hydrostatic equations of motions

$$\frac{D\mathbf{v}}{Dt} = -\nabla\frac{p'}{\bar{\rho}} + \mathbf{g}\frac{\theta}{\bar{\theta}} - \mathbf{f}\times\mathbf{v}' + \mathcal{M}', \tag{3.1}$$

$$\frac{D\theta}{Dt} = 0, \tag{3.2}$$

$$\nabla\cdot(\bar{\rho}\mathbf{v}) = 0, \tag{3.3}$$

are used in their anelastic ($\bar{\rho} = \rho_0 \cdot \exp(-z/H)$) and Boussinesq approximated ($\bar{\rho} = \rho_0$) form (Smolarkiewicz et al. 2001, Prusa et al. 2008). $\frac{D}{Dt}$ is the material derivative, $\mathbf{v}$ is the velocity vector, $\mathcal{M}$ represents appropriate metric forces, and $\mathbf{f}$ and $\mathbf{g}$ symbolize the vectors of Coriolis parameter and gravity acceleration. Primes denote deviations from the ambient state and overbars refer to the horizontally homogeneous hydrostatic reference state of the Boussinesq expansion around a constant stability profiles (Smolarkiewicz et al. 2001). EULAG has been applied for a broad range of topics in fluid dynamics like turbulence (e.g., Domaradzki et al. 2003), urban flows (e.g., Wyszogrodzki and Smolarkiewicz 2010, Gisinger et al. 2015), orographic GWs (e.g., Prusa et al. 1996, Grubišić and Smolarkiewicz 1997) but also for stellar convection (Elliott and Smolarkiewicz 2002).

3.1.2 ECMWF Numerical Analyses and Forecasts

Operational analyses of the Integrated Forecast System (IFS) of the European Centre for Medium-Range Weather Forecasts (ECMWF) provide meteorological data to

[3] http://www2.mmm.ucar.edu/eulag/

characterize the atmospheric situation. The 6 hourly operational analyses and hourly forecast fields of the IFS cycle 40r1[4] have a horizontal resolution on the reduced linear Gaussian grid of about 16 km (TL1279) and 137 vertical model levels (L137) from the ground to $\sim$ 80 km (0.01 hPa). The layer thicknesses gradually increases from $\sim$ 300 m at $\sim$ 10 km altitude, to $\sim$ 400 m at $\sim$ 20 km altitude and $\sim$ 2 km at $\sim$ 60 km altitude[5].

3.2 Gravity Wave Analysis of Radiosonde Data

3.2.1 Sensors and Data

DEEPWAVE (Fritts et al. 2016) dealt with atmospheric GWs and its field phase took place in NZ in austral winter 2014. The goal was to study and gain better understanding of excitation, propagation, and dissipation of GWs from the troposphere to the top of the middle atmosphere. Besides the Southern Andes, the Antarctic Peninsula, Tasmania and other small islands in the Southern Ocean, the South Island (SI) of NZ constitutes one of several hotspots of stratospheric GW activity in the Southern Hemisphere during austral winter (Jiang et al. 2006, Hoffmann et al. 2016).The campaign combined a set of airborne and ground-based measurements to reach the above mentioned goal. In addition to e.g., lidars on the ground and on board of the aircraft measuring tropospheric winds and stratospheric and mesospheric temperatures, radiosondes were used to obtain temperature, pressure, humidity and wind profiles in the troposphere and stratosphere up to $\sim$ 35 km. In the altitude range from above the maximum flight altitude of the aircraft (approx. 11 km for the DLR Falcon and 13 km for the NSF/NCAR GV) to where the ground-based lidar measurements started (approx. 25 to 30 km) the only measurements came from the radiosondes. The radiosonde station at Lauder (Fig. 3.1) in the premises of New Zealand's National Institute of Water and Atmospheric Research (NIWA) was operated by the German Aerospace Center (DLR), the Meteorological Institute Munich (MIM) of Ludwig-Maximilians-University Munich (LMU) and the Institute of Atmospheric and Cryospheric Sciences (ACINN) of University of Innsbruck. Two different sounding systems were used. One system used the GRAW DFM-09 in combination with GRAWMET software. The DFM-09 has a ceramic temperature sensor and a capacitive polymer humidity sensor. Pressure as well as wind are determined via global positioning system (GPS) data. The accuracy of the measurements is < 0.2 K for temperature, < 5 % for relative humidity, < 0.3 hPa for pressure and < 0.2 m s^{-1} for wind speed (GRAW 2011). The second system was a

[4] https://www.ecmwf.int/en/forecasts/documentation-and-support/evolution-ifs/cycle-40r1-summary-changes, accessed 6 Feb 2018

[5] https://www.ecmwf.int/en/forecasts/documentation-and-support/137-model-levels, accessed 6 Feb 2018

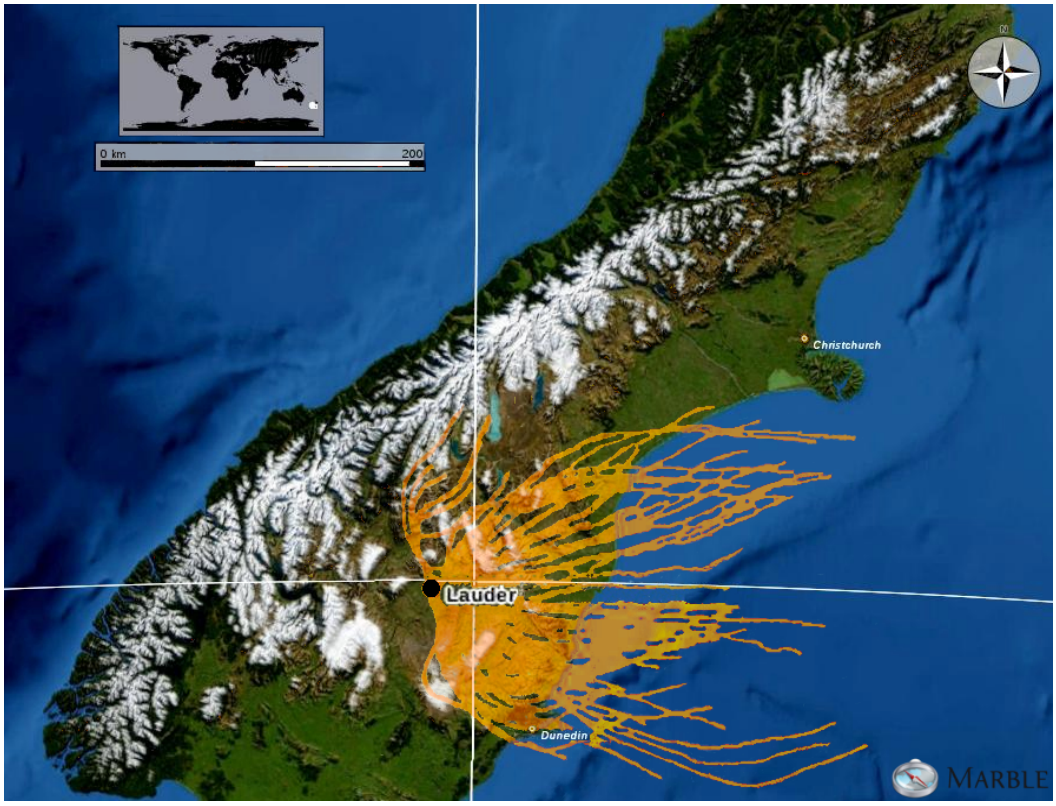

Figure 3.1: SI of NZ showing the Southern Alps and the location of the radiosonde station in Lauder as well as the trajectories of the soundings released during DEEP-WAVE. Map is based on NASA's "Blue Marble Next Generation" (Credits: NASA's Earth Observatory).

Vaisala Digicora sounding system with RS-92 radiosondes. The RS-92 has a capacitive temperature sensor with a total accuracy < 0.2 K for 1080–100 hPa, < 0.3 K for 100–20 hPa and < 0.5 K for 20–3 hPa. The capacitive humidity sensor has an accuracy of 2 % and the Silicon pressure sensor of 0.5 hPa for 1080–100 hPa and 0.3 hPa for 100–3 hPa. The GPS wind finding has an accuracy of 0.15 ms^{-1} in wind speed and 2 degrees in wind direction (VAISALA 2013). Data were stored in 1 s interval for the DFM-09 and in 2 s interval for the RS-92. The mean balloon ascent rate of 5 ms^{-1} leads to a vertical resolution of about 5 and 10 meters, respectively. The ascent rate of the balloon needed for MW analysis was calculated using GPS-altitude. All data were interpolated on a regular 25 m vertical grid for further analyses.

Altogether, 92 radiosondes distributed over different intensive observing periods (IOPs) were released at Lauder in the period from 13 June to 1 August 2014. The main part of the radiosondes drifted towards East (Fig. 3.1) due to the prevailing westerly winds in the lower and middle stratosphere. 72% of the radiosondes collected usable data

Table 3.1: Number of soundings released and included in the analysis for each IOP as well as the start time in UTC of the first and the last sounding used to show the time period covered by the soundings.

	IOP									
	3	4	6	8	9	10	13	15	16	21
released	9	4	5	12	15	13	19	6	4	5
used	9	3	1	6	10	12	15	3	4	3
first	Jun	Jun	Jun	Jun	Jun	Jul	Jul	Jul	Jul	Jul
	13th	16th	19th	24th	28th	3rd	10th	16th	20th	30th
	1830	0906	1431	0935	2336	2335	1754	0000	0537	1129
last	Jun	Jun	Jun	Jun	Jun	Jul	Jul	Jul	Jul	Aug
	14th	16th	19th	25th	30th	4th	13th	17th	20th	1st
	1730	1436	1431	1432	1435	2036	0238	0000	2325	1723

to an altitude of at least 27 km. The balloon burst for the other 28 % either below 27 km or problems with the data transmission and reception led to gaps in the profiles or profiles were not used due to "bad data quality" (e.g., downward motion of the balloon). Table 3.1 shows the number of soundings released and the number used for analysis with respect to the IOPs.

3.2.2 Background and Perturbation Profiles

The basic idea of the radiosonde analysis methods is that the perturbations of horizontal wind (u', v'), perturbations of the ascent rate (taken as w), and perturbations of temperature (T') from a background state can be associated to GWs (Eq. (2.8)-(2.11)) and, hence, can be analyzed for the GW properties. For this purpose either a temporal mean over multiple soundings (e.g., a monthly mean when conducting climatological studies) or a polynomial fit of various orders can be used as background state. In general, perturbations in atmospheric variables caused by GWs can be more easily detected in the stratosphere than in the troposphere due to the decreasing density with altitude which lets the GWs' amplitudes increase because of energy conservation. Moreover, perturbations in the troposphere could also be influenced by migratory weather systems (e.g., Lane et al. 2003).

The sensitivity in the determination of temperature and velocity perturbation profiles has been tested using different methods based on polynomial fitting (not shown). The different methods are a 2^{nd} and 4^{th} order polynomial fit for the whole sounding, a 2^{nd} and 4^{th} order polynomial fit for troposphere (1-8 km) and stratosphere (13-27 km)

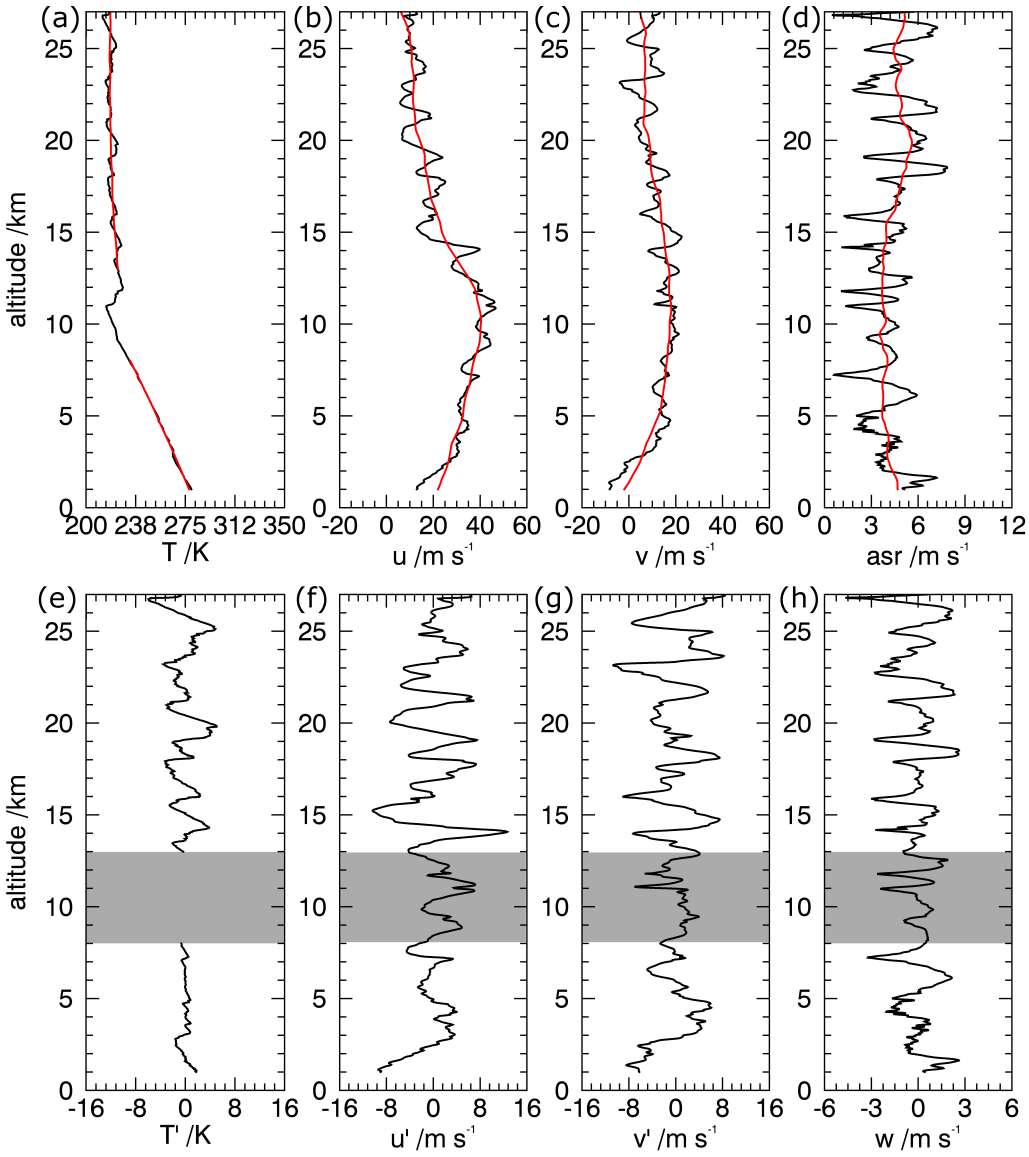

Figure 3.2: Profiles of (a) temperature, (b) zonal wind, (c) meridional wind and (d) ascent rate showing also the combined 2nd order polynomial and 5 km mean background fit (red) and the resulting perturbation profiles (e,f,g,h) for a sounding released on 4 July 2014 at Lauder. Further analysis are conducted separately for troposphere (1-8 km) and stratosphere (13-27 km).

separately and sliding 3rd order polynomial fits with a length of 20 km. The latter is a method which is used for Rayleigh lidar data (Duck et al. 2001). Moreover, the effect of additionally subtracting a 5 km mean from the derived perturbations at every height has been tested (Lane et al. 2000, Reeder et al. 1999, Lane et al. 2003). It was

found that the polynomial fitting depends on the altitude range of the fitting as well as on the shape of the measured profiles (e.g., strong gradients) which can lead to outliers in the perturbation profiles. All methods give nearly identical results for the ascent rate due to the smoother background (mean around 5 m s^{-1}) compared to temperature and horizontal wind. The subtraction of the additional 5 km mean leads to more similar results for all polynomial fits and reduces outliers for the temperature and the horizontal velocity perturbations. Wave-like perturbations with apparent vertical wavelengths less than 5 km are retained (Lane et al. 2000). The tropopause region should be excluded when deriving temperature perturbations. Artificial signatures are introduced by a fit which tries to catch the tropopause inversion (Schmidt et al. 2008). Finally, a 2nd order polynomial fit for troposphere and stratosphere separately with the 5 km mean subtracted is used when determining temperature perturbations (T'). A 2nd order polynomial fit for the whole sounding with the 5 km mean subtracted is used when determining velocity perturbations (u', v', w), i.e. from horizontal velocity and balloon ascent rate (Fig. 3.2). Further analyses of the radiosonde perturbations were conducted for troposphere and stratosphere separately. The tropopause region itself is excluded because the temperature profiles show remarkable gradients in this region. Moreover, static stability changes between troposphere and stratosphere which influences the ascent of the balloon in the transition region.

3.2.3 Properties and Limits

Radiosonde measurements are not conducted along strictly vertical or horizontal trajectories. While the radiosonde mounted on a balloon is ascending with approximately 5 m s^{-1} up to 35 km altitude it also drifts horizontally up to 100–300 km depending on wind conditions. Therefore, the measurements are taken along a tilted trajectory containing not only vertical but also horizontal information. Moreover, the perturbations of the different variables are sensitive to different parts of the GW spectrum. This can be readily seen when considering the dispersion relation of two-dimensional ($l = 0$) linear GWs in a rotating Boussinesq fluid (e.g., Eq. (3.61) in Nappo 2012) and the relationship between GW scales (e.g., wavenumbers) and GW amplitudes (Lane et al. 2003):

$$\frac{m^2}{k^2} = \frac{N^2 - \Omega^2}{\Omega^2 - f^2}, \tag{3.4}$$

$$A_w = \frac{-kA_u}{m}, \tag{3.5}$$

$$A_u = \frac{-mA_w}{k}, \tag{3.6}$$

$$A_\theta = \frac{A_w \theta_0 N^2}{\Omega g} = -\frac{\theta_0 N^2}{\Omega g}\frac{kA_u}{m}, \tag{3.7}$$

where k is the horizontal wave number ($l = 0$). Note that these relationships between the GW scales and amplitudes result from the continuity equation of a Boussinesq fluid and that the phase difference between maximum vertical velocity perturbation (A_w) and the maximum potential temperature perturbations (A_θ) is $\pi/2$ (Lane et al. 2003).

It follows from the equations above that low frequency (inertia-GWs) have larger signatures in the horizontal wind than in the vertical wind because, all things being equal, a decrease of the intrinsic frequency ($\Omega \rightarrow f$) leads to an increase of the vertical wavenumber ($m \uparrow$) and/or a decrease of the horizontal wavenumber ($k \downarrow$) and, therefore, to an increase of the horizontal perturbation amplitude ($|A_u|$). In contrast, medium to high frequency GWs have larger signatures in the vertical wind than in the horizontal wind ($\Omega \rightarrow N$, $m \downarrow$, $k \uparrow$, $|A_w| \uparrow$). (Potential) temperature can be a response to low- to high-frequency GWs (Lane et al. 2003). Therefore, measurements of horizontal velocity perturbations are more likely dominated by low frequency GWs, while measurements of vertical velocity perturbations are more likely dominated by medium to high frequency GWs (Lane et al. 2000, 2003, Geller and Gong 2010).

The following conditions relate the ascent of the balloon in the background wind field to the spatial scales and the frequency of the GWs

$$\left| \frac{kU + lV}{m\overline{W}_B} \right| << 1, \tag{3.8}$$

$$\frac{\omega}{m\overline{W}_B} << 1, \tag{3.9}$$

where $\overline{W}_B$ is the mean ascent rate of the balloon and ω is the ground-based frequency (Gardner and Gardner 1993). When the horizontal wavelength is much larger than the vertical wavelength and the period is large compared with the time taken for the balloon to rise through one wavelength, the above conditions are satisfied and the sounding can be treated as a vertical profile (Lane et al. 2003). If the analyzed GW field comprises a spectrum of GWs, the sounding can be treated as a vertical profile when analyzing the horizontal velocity perturbations, i.e. inertia-GWs. The motion of the balloon relative to the wave field must be taken into account when the ascent rate of the balloon or vertical velocity perturbation, i.e. medium to high frequency GWs, are analyzed (Reeder et al. 1999, Lane et al. 2003).

3.2.4 Methods to determine Gravity Wave Properties from Soundings

Because of the distinct differences between the horizontal and vertical velocity perturbations, the GW kinetic energy is also separated into horizontal and vertical contributions.

Hence, based on the different perturbation variables (Eq. (2.8)-(2.10)) one can distinguish horizontal GW kinetic energy, vertical contribution of GW kinetic energy and GW potential energy per mass

$$\overline{KE} = \frac{1}{2}(\overline{u'^2} + \overline{v'^2}), \tag{3.10}$$

$$\overline{VE} = \frac{1}{2}\overline{w^2}, \tag{3.11}$$

$$\overline{PE} = \frac{1}{2}\frac{g^2}{N^2}\overline{\left(\frac{T'^2}{T_0^2}\right)}, \tag{3.12}$$

where the overbar marks vertically averaged values or averaging over wave phase (Gong and Geller 2010, Geller and Gong 2010).

GWs are characterized with different analysis methods which assume either that (I) the horizontal perturbations are caused by inertia-GWs or (II) the horizontal perturbations are caused by stationary inertia-GWs, i.e. hydrostatic MWs ($\ell >> k$, Lin (2007)) influenced by the Coriolis force or (III) the vertical velocity perturbations are caused by stationary medium to high frequency MWs. It is necessary to ensure that the analyzed time intervals are characterized by sufficiently steady conditions when determining wave properties (cf. Sec. 2.1). It takes the radiosonde, which has a mean ascent rate of 5 m s^{-1} , about 24 minutes and 48 minutes to pass the analyzed altitude range of the troposphere, i.e. 1-8 km, and of the stratosphere, i.e. 13-27 km, respectively. It seems plausible to assume that largely steady conditions prevail for those short time intervals and that the temporal changes of the wave structure are small.

First, methods dealing with inertia-GWs are presented. For this purpose the behaviour of the horizontal velocity perturbations with altitude is exploited. The hodograph ($u'(z)$ plotted against $v'(z)$) gives information about the waves' intrinsic frequency, vertical propagation direction and in combination with temperature information the horizontal propagation direction (cf. Fig. 2.1b). So called rotary spectra and Stokes parameters can be used to calculate those wave properties (Eckermann and Vincent 1989, Eckermann 1996, Vincent et al. 1997, and references therein).

Rotary spectra decompose a sounding into upward and downward propagating parts by applying a fast Fourier transform (FFT) to the complex expression $u'(z) + iv'(z)$. It must be noted that this decomposition is not necessarily the real partitioning of upward and downward propagating waves, especially when the waves are more elliptically or even linearly polarized. That is because linearly polarized waves are decomposed into equal upward and downward propagation direction even if the dominant propagation is upward. Nevertheless, if the ratio of the power of the upward propagating part of the spectrum and the total power

$$R = \frac{\sum_m(\text{power}(m) \times m)_{up}}{\sum_m(\text{power}(m) \times m)_{up} + \sum_m(\text{power}(m) \times m)_{down}} \tag{3.13}$$

is larger than 0.6, one can assume that upward wave propagation is dominant (Guest et al. 2000). However, one cannot say for example, that 60 % of the waves propagate upward and 40 % propagate downward (Vincent 1984, Eckermann and Vincent 1989, Vincent et al. 1997, K. Sato personal communication Apr 2016).

The dominant horizontal phase propagation direction of GWs is given by the orientation of the major ellipse of the hodograph (Fig. 2.1b) and can be calculated from Stokes parameters. The remaining 180° ambiguity can be resolved by investigating the sign of the velocity perturbation in the direction of the major axis times the temperature perturbation shifted by 90° using a Hilbert transformation (Vincent et al. 1997). Corresponding results can be also achieved by directly using the covariances of the horizontal velocity perturbations and the Hilbert transformed temperature perturbations

$$\phi = \arctan\left(\frac{\overline{u'T'_{+90}}}{\overline{v'T'_{+90}}}\right) \tag{3.14}$$

(Evan and Alexander 2008). The result is the angle of the direction of propagation given in degrees clockwise from North (and not in degrees anticlockwise from East as described in Evan and Alexander (2008)). u' and v' must be exchanged to get the direction of propagation in degrees anticlockwise from East. This statement was verified with synthetic signals of u', v' and T' which were constructed based on linear wave theory.

Moreover, Stokes parameters can be used to determine the intrinsic frequency of the dominant wave mode. Before the calculated axial ratio of the ellipse is converted to the intrinsic frequency (Fig. 2.1b), a correction for transverse-shear effect is taken into account (Vincent et al. 1997). The sign of the Stokes parameter Q gives information about cyclonic and anticyclonic rotation of the hodograph with altitude (Fig. 2.1b) and, hence, the dominant vertical propagation direction of the wave energy (Eckermann and Vincent 1989).

The vertical wave number is determined by taking the maximum of the area preserving Fourier power spectrum of the horizontal velocity perturbations (sum of zonal and meridional power spectra times corresponding wave number). The wave number of the maximum corresponding to the smaller wave number (larger wavelength) is used in the case of two maxima of nearly equal power. The horizontal wave number can be calculated when the vertical wave number and the intrinsic frequency are known. Therefore, the simplified form of the dispersion relation for low frequency waves is used (Eq. (2.14)). Based on the horizontal and vertical wave numbers and intrinsic frequency, phase speed and group velocity are calculated using Eqs. (2.15)-(2.24). The direction of the horizontal wave number vector and the horizontal phase speed is the one determined from Stokes analysis or Eq. (3.14). As for the vertical phase speed, the sign of m giving the vertical direction of propagation was set according to the vertical

energy propagation derived from Stokes analysis, i.e. m negative for upward energy propagation and downward phase propagation.

In addition, a new approach, which led to successful results in a case study of MWs over Svalbard (Dörnbrack et al. 2017b), is executed. If it is assumed that the inertia-GWs are linked to the mountains, i.e. long stationary hydrostatic waves in the rotating regime, their horizontal wavenumber k_h can be estimated based on Eq. (2.27) via

$$k_h = -\frac{\Omega}{\langle u_c \rangle_z}, \tag{3.15}$$

where now Ω is the intrinsic frequency derived from Stokes analysis and $\langle u_c \rangle_z$ is the median horizontal cross mountain wind component of the analyzed altitude range. The latter is assumed to point along the horizontal wave vector of the waves which were triggered at the mountain range by the low level wind. The assumption of the traditional inertia-GW analysis, i.e. a sounding can be treated as vertical profile and hence the Fourier power spectrum reveals the true vertical wavelength, is replaced for this approach by the assumption of stationarity (Eq. (2.27)). The idea for trying this approach was motivated by the fact that for mesoscale mountain ranges such as the NZ Alps the effects of Earth's rotation, which appear in the horizontal velocity perturbations, become important (Lin 2007). According to Lin (2007), in this case the advection time of an air parcel to pass over the mountain is too large to be ignored compared to the period of inertial oscillation due to Earth's rotation. The influence of rotation can be estimated with the Rossby number

$$Ro = U_{kh}/(fL), \tag{3.16}$$

where L is the horizontal scale of the mountain (Lin 2007). If Ro is around 1, rotation can no longer be ignored. Ro for NZ is around 0.6 to 1.5 for $U_{kh} = 15$ m s^{-1} and L between 250 km for the width of the SI and 100 km for the main mountain range of the Southern Alps. Inertia-GWs generated by mountains have already been observed over Scandinavia by airborne lidar measurements (Dörnbrack et al. 2002) and over Svalbard by satellite and radiosonde measurements (Dörnbrack et al. 2017b). Inertia-GWs generated by mountains and occurring together with jet generated inertia-GWs have been observed in VHF radar measurements (Serafimovich et al. 2006). Moreover, Smith and Kruse (2017) found MWs of larger horizontal scales in aircraft horizontal velocity measurements compared to vertical velocity measurements during DEEPWAVE.

Second, perturbations of the balloon ascent rate were regarded as vertical velocity perturbations (w, Eq. (2.10)) and analyzed for MWs (Lane et al. 2000). The balloon ascent rate was calculated from GPS-altitude. The horizontal projection method as presented in Lane et al. (2000) takes into account the horizontal drift of the sondes. The dominant horizontal wavelength is derived by projecting the data to the horizontal (a hypothetical horizontally moving radiosonde would measure the true horizontal

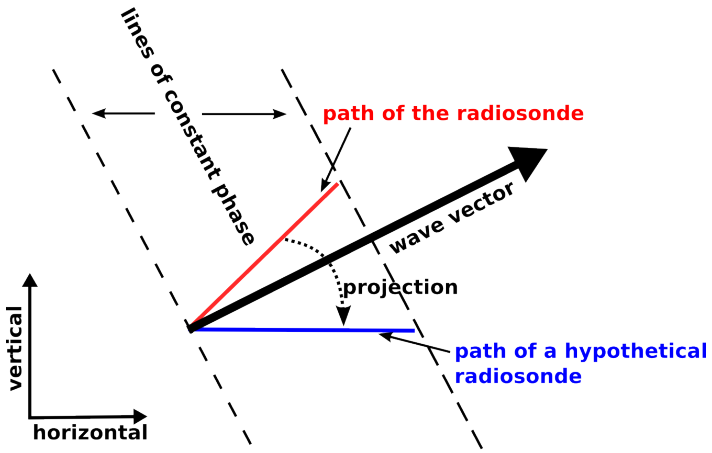

Figure 3.3: Sketch of the concept of the horizontal projection method. Figure after Lane et al. (2000).

wavelength, Fig. 3.3). The method was applied to the tropospheric (1-8 km) and the stratospheric (13-27 km) part of the soundings. For this analysis the wind direction of the lower troposphere (1-3 km) is crucial when it comes to MW triggering and propagation, i.e. it determines the direction of the horizontal wave vector. Profiles of the wind component in this direction (U_{kh}) were computed and used as cross mountain wind (u_c). In contrast to the methods for the inertia-GWs where a set of GW parameter was determined for the whole altitude range, i.e. one intrinsic frequency, one vertical wavelength and one horizontal wavelength, the horizontal projection method allows to account for the vertical changes of the background flow (Lane et al. 2000). Those vertical changes cause variations of the intrinsic frequency and the vertical wavelengths with altitude. Under the assumption of stationarity, the intrinsic frequency $\Omega(z)$ (Eq. (2.27)) and the vertical wavenumber $m(z)$ (Eq. (2.28)) can be calculated from the horizontal wavenumber k_h and $u_c(z)$, which is used as background wind.

Horizontal and vertical group velocities can then be calculated from the determined wave numbers (Eqs. (2.25) and (2.26)). Determining the vertical wavenumber from Eq. (2.28) does not reveal the vertical progapation direction and therefore vertical group velocities will be just shown as positive values later on.

4 Results

The results are presented in the following order. First, idealized numerical simulations with EULAG are presented to assess the influence of a tropopause inversion on mountain wave propagation. The idealized numerical simulations are followed by a comprehensive analysis of the atmospheric conditions of the real atmosphere during DEEPWAVE. Different datasets and diagnostics are combined to characterize the background atmosphere from the troposphere to the lower stratosphere. How weather regimes and the atmospheric state compare to climatological conditions is reported upon and how they relate to the airborne and ground-based gravity wave observations is also explored. The section is concluded by GW activity and characteristics during DEEPWAVE which are determined from radiosonde data. The different methods, which were presented in section 3.2.4, are used to determine the characteristics of GW with low to high intrinsic frequencies.

4.1 Idealized Simulations with EULAG

In this section, it is investigated if wave trapping on an inversion found in the lower troposphere (Vosper 2004) can also occur at tropopause altitudes and which conditions are necessary for it. The computational parameters are chosen similar to Vosper (2004). The 2-dimensional domain consists of 1032 and 2000 grid points in x and z direction, respectively, with grid increments of $\Delta x = 100$ m and $\Delta z = 10$ m. This results in a total domain size of about 103 km $\times$ 20 km. The integration time step Δt is set to 1 s. Open boundaries are applied in x-direction. The model top is a rigid lid. The sponge layers at the horizontal edges of the domain are 8 km wide and the sponge layer at the top of the domain starts at 15 km altitude. As in Vosper (2004) an idealized ridge

$$h(x) = \begin{cases} h_0[1 + \cos(Kx)]/2 & \text{for } |x| \leq \pi/K \\ 0 & \text{for } |x| > \pi/K, \end{cases} \tag{4.1}$$

where $K = 2\pi/L$, and free slip lower boundary condition are used. Mountain height h_0 is set to 400 m and width L to 10 km or 5 km.

The EULAG RUNs #1-7 use the Boussinesq approximated equations (Sec. 3.1.1), vertically constant horizontal velocity $U = 8$ m s^{-1} ($V = 0$), and different profiles

of potential temperature with the corresponding Brunt-Väisälä frequency as initial conditions (Tab. 4.1). The lowest value of θ at $z = 0$ km is always 284.4 K. For RUN #8 the horizontal velocity linearly increases from $U(z = 0 \text{ km}) = 4 \text{ m s}^{-1}$ to $U(z \geq 3 \text{ km}) = 20 \text{ m s}^{-1}$. Additionally, non-Boussinesq (i.e. anelastic) equations are used for RUN #8 which include the increase of wave amplitudes due to decreasing density (Sec. 3.1.1).

At first, two model runs were conducted to check the agreement of the simulation with the results of Vosper (2004). The stratification changes for RUN #1 from neutral to stable ($N_U = 0.01 \text{ s}^{-1}$) at 400 m altitude without an inversion (cf. Fig. 2.4a). As in Vosper (2004), these conditions result in an upward propagating MW above the neutral layer and no wave trapping (Fig. 4.1a). The upward propagating MW has a horizontal wavelength of approximately 10 km and a vertical wavelength of approximately 5.5 km. The latter is close to what is predicted by linear theory where the vertical wavenumber m is equal to $\sqrt{\ell^2 - k^2} = \sqrt{\frac{N^2}{U^2} - k^2}$ (Eq. (2.30)). An inversion with $\Delta\theta = 3.3$ K is introduced for RUN #2 at 1600 m altitude (cf. Fig. 2.4d). Besides the upward propagating MW, there is now also a train of interfacial waves on the inversion at 1600 m altitude. The amplitudes of the upward propagating wave is smaller compared to RUN #1 (approximately 0.8 vs 1.2 m s^{-1} for vertical velocity at 7 km altitude). The amplitudes of the interfacial waves above the inversion at 2000 m altitude are approximately 0.6 m s^{-1} for vertical velocity and approximately 0.2 K for potential temperature. Their horizontal wavelength is approximately 4.8 km which is right below the critical horizontal wavelength (or right above the critical horizontal wavenumber) of the stable layer causing them to become evanescent above the inversion (cf. Sec. 2.1). RUN #1 and #2 confirm that the EULAG model and the chosen model setup is appropriate to simulate MW propagation and trapping on an inversion as in Vosper (2004). Hence, a number of runs were conducted to test the influence of the TIL on MWs. Compared to the inversion in the troposphere, the inversion at the tropopause is capped by a higher static stability ($N_U \approx 0.02 \text{ s}^{-1}$) and is located at higher altitudes further away from the surface, where the wave source is located.

First, the influence of the stability above the inversion is investigated. N_U was set to a value of 0.02 s^{-1} for RUN #3 by using a larger linear gradient in the computation of the θ-profile ($\mathrm{d}\theta/\mathrm{d}z = 12$ K km^{-1}). A propagating MW with a horizontal wavelength of approximately 10 km and a shorter vertical wavelength of about 2.8 km compared to RUN #2 is visible above the mountain (Fig. 4.2a). No local maxima are found at the altitude of the inversion, i.e. for RUN #3 no interfacial waves occur on the inversion. A look at Table 4.1 and Eq. (2.40) reveals that the condition for trapping is no longer fulfilled for $N_U = 0.02 \text{ s}^{-1}$ and $\Delta\theta = 3.3$ K. $\Delta\theta$ was increased to 6.6 K for RUN #4 and trapping is again found on the inversion (Fig. 4.2b). However, the amplitudes are small for this model setup (< 0.1 m s^{-1} for vertical velocity). The horizontal wavelength of the interfacial waves is only about 2.4 km which is in agreement with the larger Scorer parameter corresponding to $N_U = 0.02 \text{ s}^{-1}$ and a critical horizontal wavelength

Table 4.1: Mountain width L, static stabilities of the lower and upper layer (N_L,N_U), strength of the inversion ($\Delta\theta$) and height (z_i), upstream wind conditions, Froude number squared, and trapping condition of the conducted numerical simulations.

RUN	L /km	N_L /s^{-1}	N_U /s^{-1}	$\Delta\theta$ /K	z_i /m	U /m s^{-1}	F_i^2	$\tanh(Z)/Z$
1	10	0.00	0.01	0.0	400	8	–	0.92
2	10	0.00	0.01	3.3	1600	8	0.35	0.48
3	10	0.00	0.02	3.3	1600	8	0.35	0.25
4	10	0.00	0.02	6.6	1600	8	0.18	0.25
5	5	0.00	0.02	6.6	1600	8	0.18	0.25
6	5	0.01	0.02	6.6	8000	8	0.035	0.05
7	5	0.01	0.02	0.0	8000	8	–	0.05
8	5	0.01	0.02	15	8000	$4 \rightarrow 20$	0.1	0.12

of around 2.8 km (e.g., Fig. 4.3a). The mountain width L was reduced to 5 km for RUN #5 to enhance the forcing of waves with shorter horizontal wavelength (Tab. 4.1). Results for RUN #5 are shown in Figure 4.3b. The amplitudes of the interfacial waves increased compared to RUN #4 to around 0.2 m s^{-1} for vertical velocity (Fig. 4.3c).

The results of the RUNs #4 and #5 confirm that trapping on the inversion can occur in the numerical simulations even when $N_U = 0.02$ s^{-1} (Fig. 4.2b and Fig. 4.3) if the linear condition for trapping (Eq. (2.40)) is fulfilled. As already mentioned above, the inversion has to be two times stronger for $N_U = 0.02$ s^{-1} than for $N_U = 0.01$ s^{-1}. The horizontal wavelength of the interfacial waves is smaller for $N_U = 0.02$ s^{-1} which suits the dependence of the wavelength of forced interfacial waves on the stratification above the inversion as estimated by Sachsperger et al. (2015). The amplitude of the interfacial waves depends on the wave forcing (Fig. 4.2b vs. Fig. 4.3).

The same simulations were conducted with a TIL located at 8 km altitude and neutral conditions below and they showed weak signs of waves trapped on the inversion (not shown). This is because the forcing of the mountain hardly reaches the inversion at 8 km altitude through the neutral layer, i.e. no upward propagating waves can exist in the neutral layer. This remark is also found in the theoretical considerations of Sachsperger et al. (2015). Nevertheless, the horizontal wavelength of the weak interfacial waves is the same as for the respective simulations with the inversion at a low altitude.

The previous findings with respect to MW forcing and strength of the inversion are taken into account for RUN #6. The stratification below the tropopause was set to $N_L = 0.01$ s^{-1} to allow for propagating waves which can reach the tropopause. The

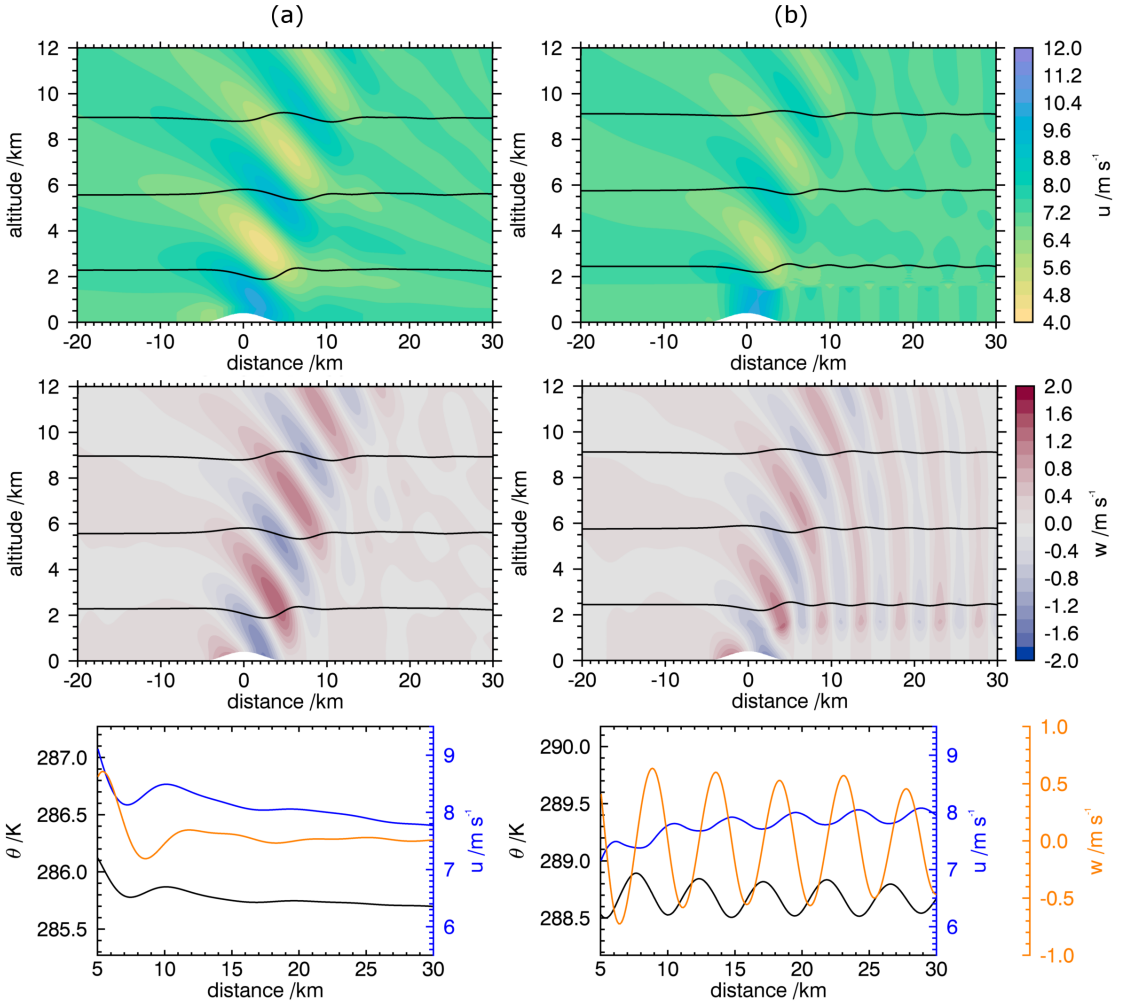

Figure 4.1: Simulation results after an integration time of 96 min when the initial disturbance[a] already lies downstream of the distance of 30 km. (Top) Horizontal and (middle) vertical velocity with potential temperature as black contours with 10 K interval, (bottom) potential temperature (black), horizontal (blue) and vertical velocity (orange) at an altitude 400 m above the change from neutral to stable stratification ($N_U \approx 0.01$ s^{-1}) for (a) RUN #1 ($\Delta\theta = 0$ K) and (b) RUN #2 ($\Delta\theta = 3.3$ K).

[a]The disturbance is produced by the mountain during the initialization of the simulation.

strength of the TIL was set to $\Delta\theta = 6.6$ K and the stratification above to $N_U = 0.02$ s^{-1}. As expected, waves of larger amplitude reach the tropopause and interfacial waves, which have an amplitude of around 0.1 m s^{-1} for vertical velocity, are found (Fig. 4.4a). The horizontal wavelength of the interfacial waves is around 2.4 km as for RUN #4 and

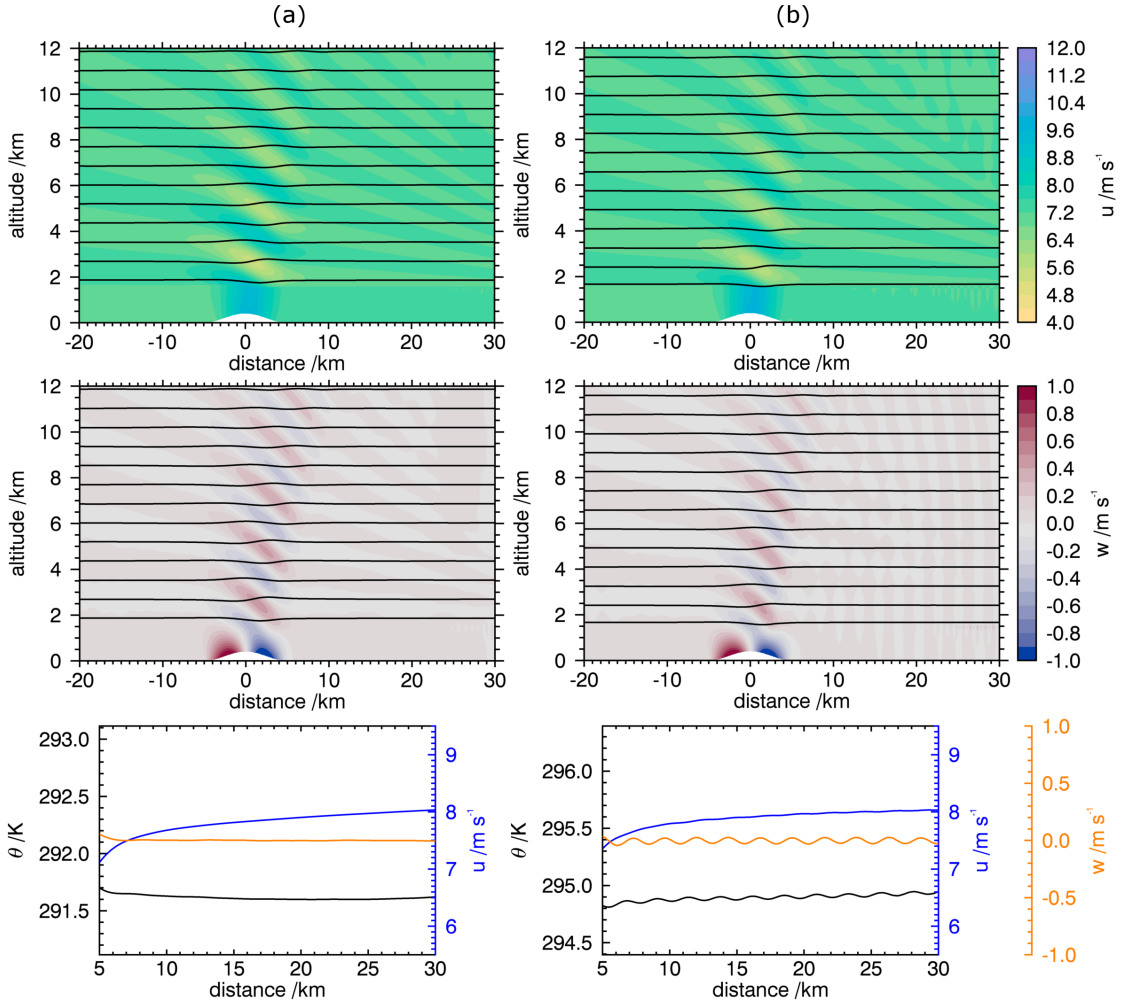

Figure 4.2: Same as Fig. 4.1 but with $N_U \approx 0.02$ s^{-1} for (a) RUN #3 ($\Delta\theta = 3.3$ K) and (b) RUN #4 ($\Delta\theta = 6.6$ K).

RUN #5. An upward propagating MW with a horizontal wavelength of approximately 10 km is found above the TIL. Besides the interfacial waves on the tropopause, two trains of trapped waves are found in the troposphere for RUN #6 (Fig. 4.4a). This highlights that reflection occurs at the tropopause. The reflected waves can persist and propagate downstream in the stably stratified troposphere. This finding is different to the simulations with neutral stratification below the inversions which does not permit any reflected waves to propagate. To answer the question whether the waves are reflected by the change of stability from $N_L = 0.01$ s^{-1} to $N_U = 0.02$ s^{-1} or whether the TIL ($\Delta\theta$) causes the reflection, RUN #7 was computed. RUN #7 uses the same setup as RUN #6 despite $\Delta\theta$ was set to zero, i.e. the stability increases at 8 km but no TIL is present. The results for RUN #7 are shown in Figure 4.4b. The interfacial

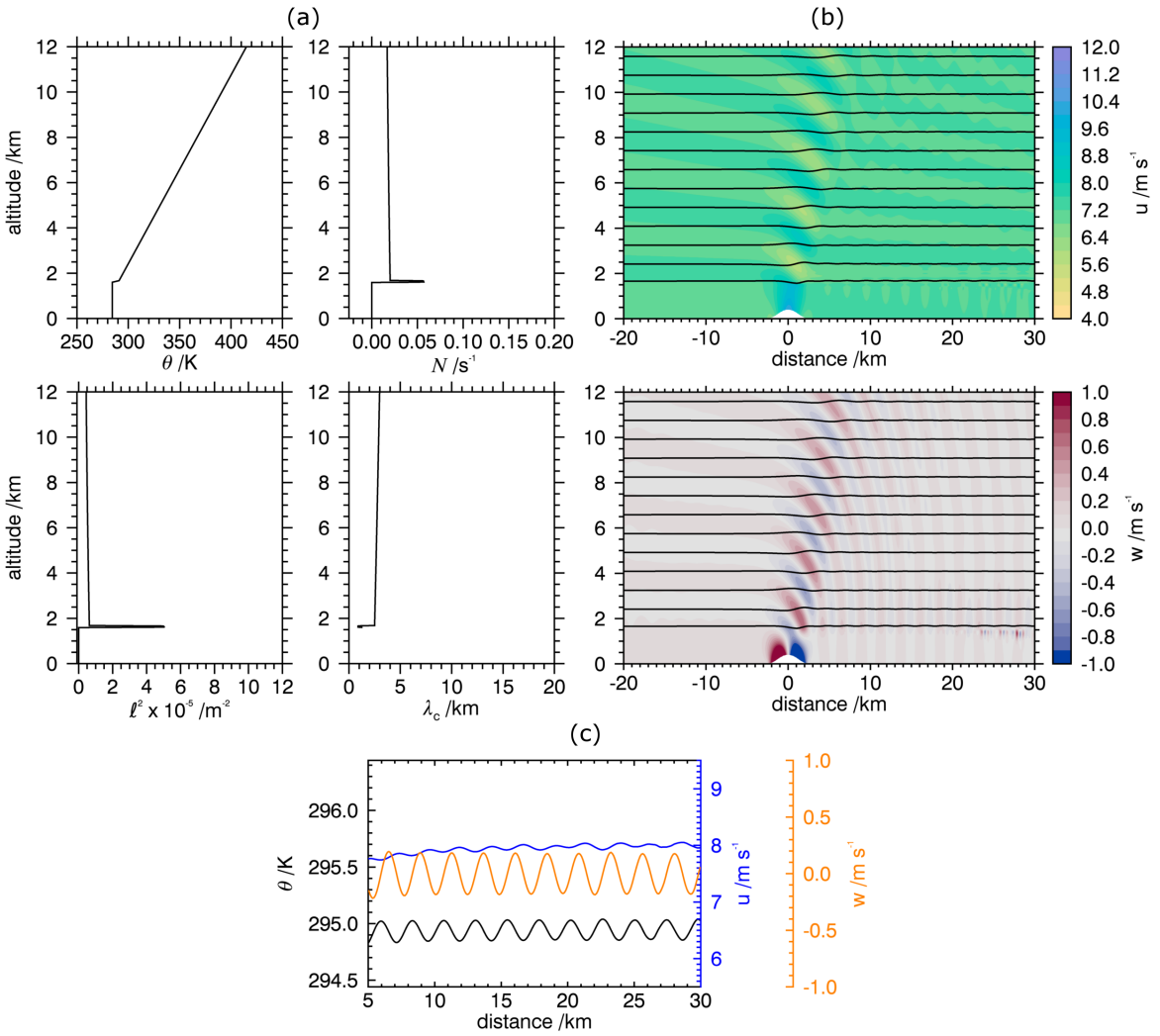

Figure 4.3: Simulation results of RUN #5 ($L = 5$ km) after an integration time of 190 min when the initial disturbance lies almost downstream of the distance of 30 km. (a) Initial profiles of potential temperature, Brunt-Väisälä frequency, Scorer parameter and critical horizontal wavelength, (b) Horizontal and vertical velocity with potential temperature as black contours with 10 K interval and (c) potential temperature (black), horizontal (blue) and vertical velocity (orange) at an altitude 400 m above the inversion ($\Delta\theta = 6.6$ K), i.e. at 2000 m altitude.

waves are missing at 8 km altitude because of the lack of the inversion (bottom panel of Figure 4.4b). The reflected waves in the troposphere are still present, although their amplitudes are smaller than for RUN #6 (middle row of Figure 4.4). This suggests that the TIL causes stronger wave reflection even its depth was set to be quite small [i.e. eight grid points (70 m)] and much smaller than the vertical wavelength of the

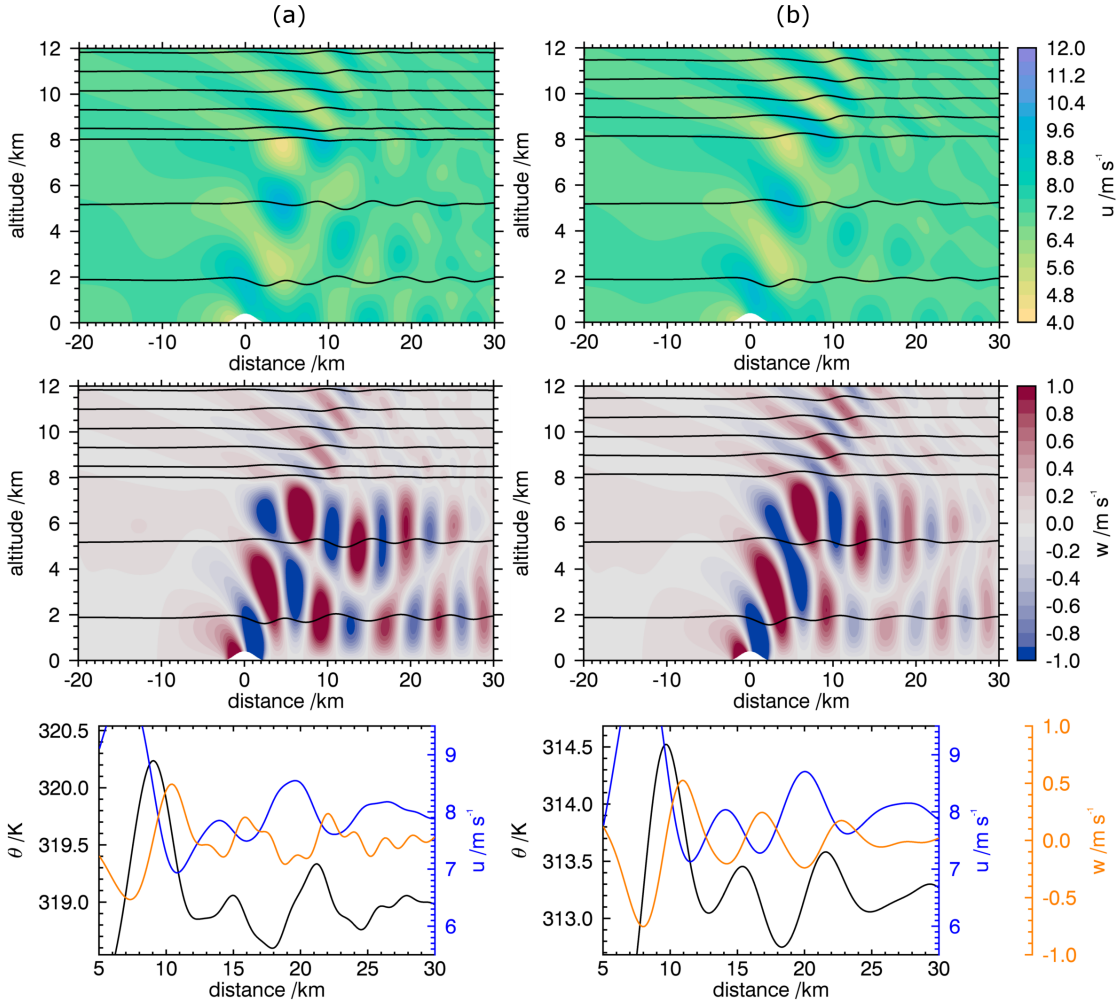

Figure 4.4: Simulation results after an integration time of 96 min when the initial disturbance already lies downstream of the distance of 30 km. (Top) Horizontal and (middle) vertical velocity with potential temperature as black contours with 10 K interval, (bottom) potential temperature (black), horizontal (blue) and vertical velocity (orange) at an altitude 400 m above the change from tropospheric (N_L = 0.01 s^{-1}) to stratospheric stratification (N_U = 0.02 s^{-1}), i.e. at 8.4 km altitude, for (a) RUN #6 ($\Delta\theta$ = 6.6 K) and (b) RUN #7 ($\Delta\theta$ = 0 K).

upward propagating waves in the troposphere, which is about 5.5 km.

The maxima of the absolute values of vertical velocity were determined for RUN #1, RUN #6 and RUN #7 to quantify the effects of the jump in stability and the TIL on the wave amplitudes in the lower stratosphere and downstream of the mountain in the troposphere (Tab. 4.2). RUN #1 is the reference for conditions where no trapping on an inversion and no wave reflection occurs. The largest absolute value of vertical velocity

in the altitude region between 9 and 12 km is found for RUN #1 being 1.05 m s^{-1}. The maximum is only 0.60 m s^{-1} for RUN #6 which has a TIL at 8 km altitude. It is 0.79 m s^{-1} for RUN #7 which has just the jump in stability. If it is assumed that the difference of these amplitudes to the amplitudes of RUN #1 goes into reflected downward propagating waves the reflection coefficient can be calculated:

$$r = \left|\frac{B}{A}\right|, \tag{4.2}$$

where B is the amplitude of the downward propagating wave and A is the amplitude of the upward propagating wave (Eliassen and Palm 1960). Note that this definition of r omits to square the amplitudes to be consistent with Keller (1994). The reflection coefficient is $\frac{1.05-0.60}{1.05} = 0.43$ for RUN #6 and $\frac{1.05-0.79}{1.05} = 0.25$ for RUN #7. The reflection coefficient can be approximated and computed directly from the Brunt-Väisälä frequencies for hydrostatic waves and in the absence of vertical wind shear

$$r \approx \frac{N_U - N_L}{N_U + N_L} \tag{4.3}$$

(Keller 1994). The approximated hydrostatic reflection coefficient is 0.33 for $N_L = 0.01$ s^{-1} and $N_U = 0.02$ s^{-1}. This value is similar to the estimate from amplitudes for RUN #7 which of course also includes non-hydrostatic contributions. One gets a reflection coefficient of 0.71 if the value of N of the TIL of RUN #6, which is approximately 0.06 s^{-1}, for N_U, is used . This is by far larger than the estimate from amplitudes for RUN #6. This suggests that the approximated hydrostatic reflection coefficient which takes into account the effect of the TIL overestimates the reflection for this case of a sharp inversion (i.e. potential temperature increases by 6.6 K over 70 m leading to a large N of 0.06 s^{-1}).

At the horizontal distance between 15 and 30 km and in the altitude region up to 7 km, i.e. the downstream region in the troposphere, the largest absolute value of vertical velocity is found for RUN #6 being 1.01 m s^{-1}, followed by RUN #7 with 0.81 m s^{-1}. For RUN #1 it is only 0.28 m s^{-1}. The analyses of the amplitudes of the RUNs #1, 6 and 7 above and downstream of the mountain clearly confirm that reflection of the upward propagating waves occurs at the tropopause and that a TIL increases the amount of reflection which leads to larger amplitudes of the reflected waves in the troposphere.

Last but not least, the wind speed is increased from 4 m s^{-1} at the low levels to 20 m s^{-1} above for RUN #8 because one can expect higher wind speeds in the upper troposphere and around the tropopause. The strength of the TIL was increased ($\Delta\theta = 15$ K) to fulfill the condition for trapping on the tropopause. Fig. 4.5 shows that the three types of waves which were found in RUN #6 are still present, i.e. the upward propagating waves in the troposphere and stratosphere above and in the lee of the mountain, the interfacial waves on the inversion, and the reflected waves in the troposphere

Table 4.2: Maxima of absolute values of vertical velocity above and downstream of the mountain for RUNs #1, 6 and 7.

distance	-20-30 km	15-30 km
altitude	9-12 km	< 7 km
RUN #1	1.05 m s^{-1}	0.28 m s^{-1}
RUN #6	0.60 m s^{-1}	1.01 m s^{-1}
RUN #7	0.79 m s^{-1}	0.81 m s^{-1}

downstream of the mountain. However, their properties are different. The interfacial waves can be only seen in this simulation setup which use an idealized and simplified mountain if the increase of wave amplitudes due to decreasing density are included (i.e. use of the anelastic equations). The reflected waves in the troposphere are still dominated by the reflection at the TIL despite the additional wind shear which may also cause reflection in the lowest 3 km altitude. The horizontal wavelengths increased as expected for higher wind speed according to the dependence on Scorer parameter and critical wavelength (Fig. 4.5a). The horizontal wavelength of the interfacial waves on the inversion is about 5.5 km with an amplitude of about 0.1 m s^{-1} in vertical velocity (Fig. 4.5c). The horizontal wavelength of the reflected waves in the troposphere increased to approximately 12 km. There is only one wave train of reflected waves due to the larger vertical wavelength of the upward propagating waves (Fig. 4.5b) compared to RUN #6.

Summary idealized simulations

To sum up, the presented results of the numerical simulations confirm that interfacial waves can exist at the TIL. The mechanism of their trapping and horizontal propagation matches the published results for boundary-layer inverisons (Vosper 2004, Sachsperger et al. 2015). However, the strength of the inversion $\Delta\theta$ must be twice as large due to the larger stability of the stratosphere, i.e. $N_U = 0.02$ s^{-1}, in case of vertically constant wind speed and even larger for higher wind speed. Moreover, it was found that reflected waves exist downstream of the mountain in the troposphere although the classical conditions of a decreasing Scorer parameter with altitude in the troposphere ("Scorer trapping", Fig. 2.3) are not fulfilled. Therefore, a fifth possibility of MW propagation behaviour (Sec. 2.2, Fig. 2.4) describing the influence of a TIL can be introduced (Fig. 4.6). The horizontal wavelength of the interfacial waves decreases with increasing stability above the inversion. The horizontal wavelengths of propagating, interfacial and reflected waves increase with increasing wind speed. The amplitudes of the reflected waves are found to be larger if an inversion is present at the tropopause than if there is

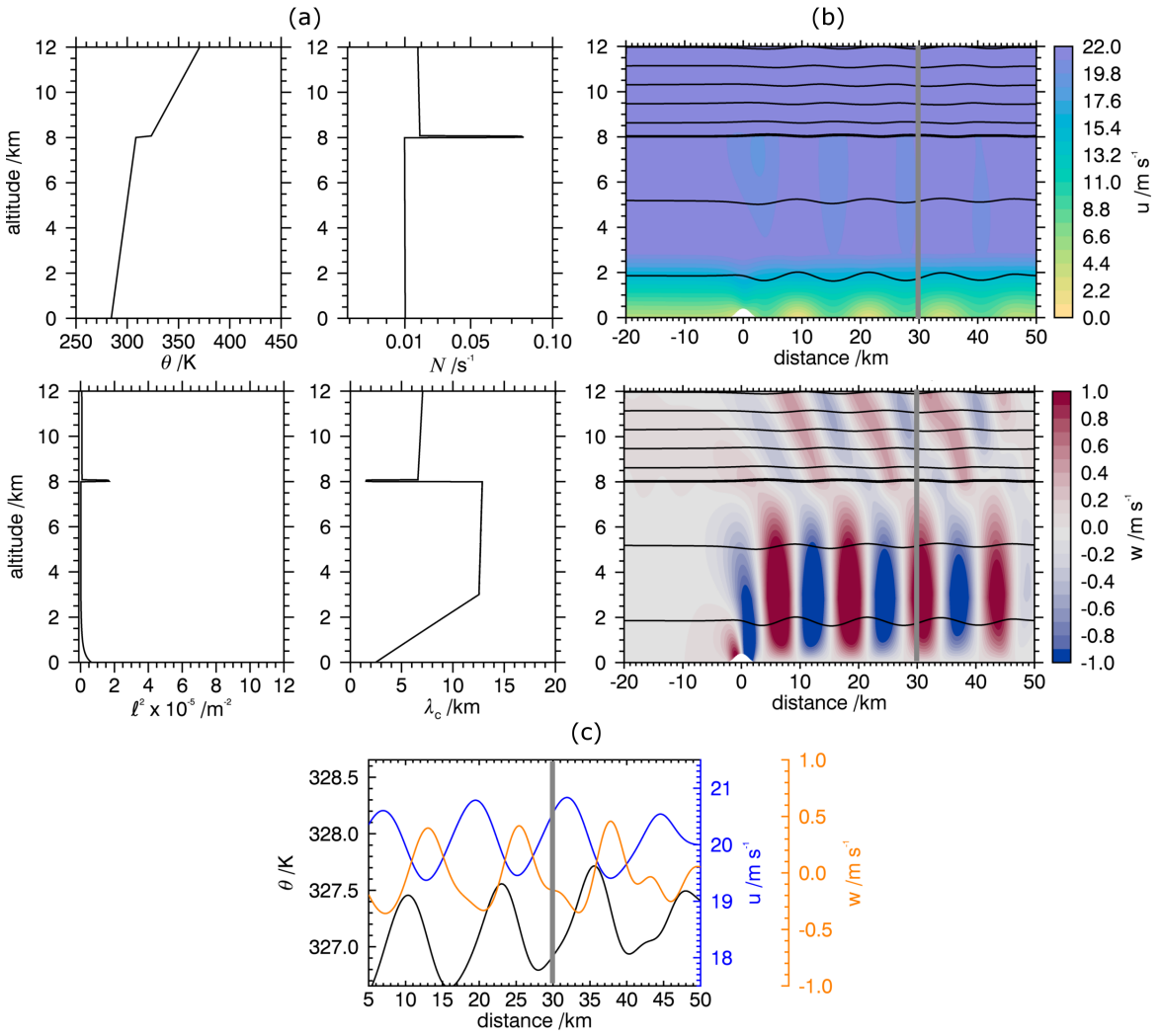

Figure 4.5: Simulation results of RUN #8 after an integration time of 285 min when the initial disturbance lies already downstream of the distance of 50 km. (a) Initial profiles of potential temperature, Brunt-Väisälä frequency, Scorer parameter and critical horizontal wavelength, (b) Horizontal and vertical velocity with potential temperature as black contours with 5 K interval and (c) potential temperature (black), horizontal (blue) and vertical velocity (orange) at an altitude 400 m above the inversion, i.e. at 8400 m altitude. Gray lines in (b) and (c) mark the range of the x-axis used for the plots of RUNs #1-7.

just the jump from tropospheric to stratospheric stability. This should be taken into account when the approximated hydrostatic reflection coefficient is calculated from Brunt-Väisälä frequencies. Though, an overestimation of the hydrostatic reflection coefficient for sharp inversions may occur. Here, the altitude range of the potential

temperature increase of the inversions, i.e. 70 m, followed the simulations of Vosper (2004). Climatological mean values of N at the TIL computed from high-resolution radiosonde data ($\Delta z = 50$ m) of northern hemispheric mid-latitude stations lie around 0.024 s^{-1} (i.e., $N^2 = 6 \times 10^{-4}$, Fig. 2.5) and the depth of the TIL varies between 500 m and 3 km (Birner 2006). Hence, it can be assumed that an overestimation of the hydrostatic reflection coefficient computed with N at the TIL is smaller for real atmospheric profiles due to the larger depth of the inversion. Detailed assessment of the influence of the depth of the TIL was not examined in this thesis. This task requires additional sensitivity studies by means of an extended set of simulations.

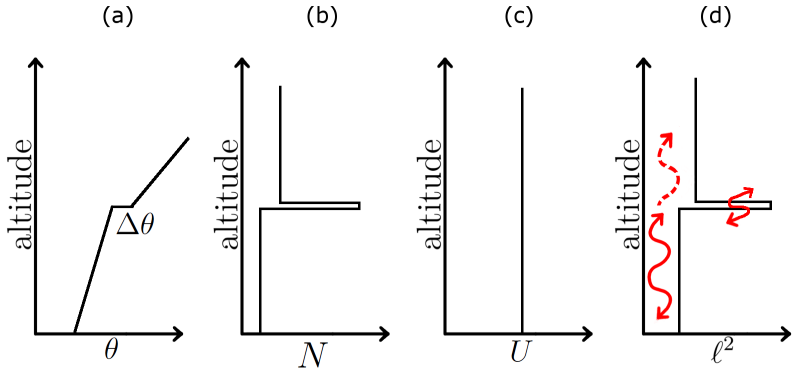

Figure 4.6: Profiles of (a) potential temperature, (b) Brunt-Väisälä frequency (Eq. (2.32)), (c) horizontal wind speed and (d) resulting Scorer parameter approximated by N^2/U^2 for propagating and reflected waves in the troposphere leaking into the stratosphere, and trapped waves on the TIL as found in simulations (Fig. 4.4a, b).

4.2 Atmospheric Conditions during DEEPWAVE

The Results presented in this section are published in Gisinger et al. (2017) © Copyright 2017 AMS.

Processes, which influence the propagation of MWs and which were identified in Section 2 and the previous section (Sec. 4.1) are controlled by the background conditions of wind and temperature. Shear and stability discontinuities cause wave reflection and can lead to wave trapping in the troposphere or interfacial waves on inversions in the troposphere and at the tropopause. Classical trapping by a decreasing Scorer parameter with altitude capped by the enhanced stability of the stratosphere can come with upward leakage of wave energy downstream of a mountain range. In addition, the low level forcing conditions triggering MWs are important. Therefore, this section gives a comprehensive overview of the atmospheric conditions for the region of NZ from the troposphere to the low-stratosphere for austral winter 2014, mainly based on ECMWF IFS data allowing to assess a possible contribution of the different processes. Key circulation features are related to climatological mean conditions and background conditions are set in connection to the probed wave events (IOPs with airborne observations and periods with only ground-based measurements (GB) as listed in Table 4 and Table 5 of Fritts et al. (2016)).

4.2.1 Tropospheric Circulation

First, the southern hemispheric tropospheric circulation situation during austral winter 2014 is analysed and its impact on the tropospheric circulation in the vicinity of NZ is highlighted. Then, the daily tropospheric circulation patterns of NZ are compared to their long-term occurrence properties and are related to wave forcing and to reported wave activity during the DEEPWAVE period.

Circulation Patterns

Typical patterns of the southern hemispheric tropospheric circulation are analysed using three commonly used climatological indices. The Southern Oscillation Index (SOI) is the difference in mean sea level pressure (MSLP) between the western and eastern tropical Pacific. In the austral winter months June/July/August (JJA), negative SOI values are associated with anomalous southwesterly flow over NZ (Gordon 1986) and a higher mean seasonal frequency of blockings (Kidson 2000). In 2014, the monthly mean SOI taken from NCEP/NCAR reanalyses[6] switched from positive values in April, May and June (0.8, 0.5, 0.2) to negative values in July, August and September (-0.2, -0.7, -0.7) indicating an increasing tendency for southwesterly flows and blocking over NZ.

[6] http://www.cpc.ncep.noaa.gov/data/indices/soi

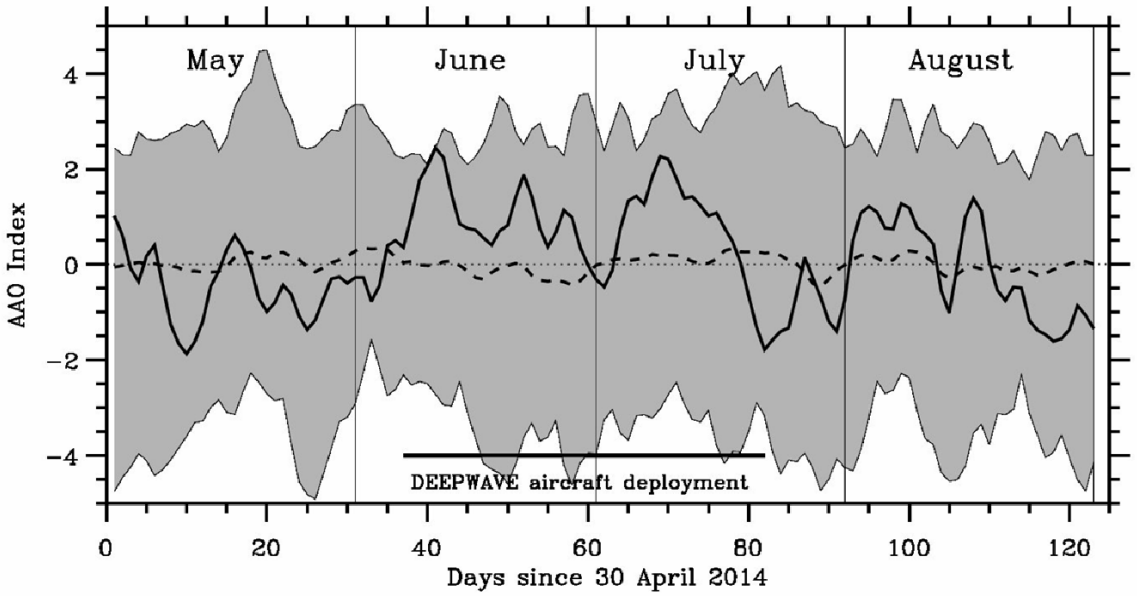

Figure 4.7: Daily SAM/AAO index for May to August 2014 (solid line). The gray-shaded area encloses the minima and maxima from 36 years of NCEP reanalysis and the dashed line shows the climatological mean. (Figure by A. Dörnbrack)

The index of the Southern Annular Mode (SAM) or Antarctic Oscillation (AAO) is calculated as the difference of the normalized zonal MSLP between 40° S and 60° S (Gong and Wang 1999). During JJA, the subtropical jet stream (STJ) and polar front jet stream (PFJ) are two bands of strong westerlies which, climatologically, are located north and south of NZ at around 30° S and 50° S, respectively (Gallego et al. 2005). The STJ is the dominant jet reaching its maximum magnitude between June and mid-September. The position, strength, and occurrence frequency of both jets depend differently on the sign of the SAM index. During positive SAM phases, the STJ is weaker. During austral winter, positive SAM phases are correlated with enhanced PFJ occurrence and peak wind speeds. Analyzing the daily evolution of the SAM index of NCEP/NCAR reanalysis reveals that the aircraft deployment of DEEPWAVE took place during a period with moderately positive SAM anomalies (Fig. 4.7). This implies slightly stronger-than-average PFJ westerlies at mid-high latitudes (50° S-70° S) and slightly weaker-than-average STJ westerlies in the mid-latitudes (30° S-50° S).

The Semi-Annual Oscillation (SAO) of the Antarctic troposphere results from the twice-yearly expansion and contraction of the circumpolar pressure trough. In a year with a pronounced SAO, the circumpolar pressure trough is deepest and located further south in the equinoctial seasons March/April/May and September/October/November. In winter and summer, the trough expands equatorward and becomes less intense

(Burnett and McNicoll 2000). To quantify an SAO index in the region of NZ, the monthly mean daily MSLP difference between 44° S and 70° S at 172° E was determined using ERA-Interim data. The resulting index revealed a generally weak local SAO for the year 2014 (not shown). This indicates a contraction of the tropospheric westerlies in the mid-latitudes and an enhancement of blocking in the vicinity of NZ during DEEPWAVE (Burnett and McNicoll 2000, Trenberth 1986).

Synoptic Flow Regimes

Some years ago Kidson (2000) introduced twelve characteristic synoptic flow regimes over NZ as daily weather types. His classification is based on surface circulation patterns derived from a cluster analysis using the 40-year (1958-1997) NCEP/NCAR reanalysis dataset. Kidson's weather types were often used in climate variability studies (e.g. Renwick 2011, and references therein). Here, we investigate the occurrence frequency of these patterns during JJA 2014 and relate them to the tropospheric forcing conditions and MW activity during DEEPWAVE. The analysis is based on the archive of NIWA, which provides an objective classification of 00 and 12 UTC NCEP/NCAR reanalyses as described in Renwick (2011) including also recent years. In the next paragraph, we first present the occurrence frequency of weather types together with selected charts of the according ECMWF IFS 1000 hPa geopotential height and horizontal wind at 850 hPa. The occurrence frequencies are then compared to the results of the long-term studies of Kidson (2000) and Renwick (2011). Second, we present the patterns which occurred during IOPs with MWs as primary target, and relate them to the reported wave activity.

The most common circulation pattern in JJA 2014 was a high pressure system centered at the south east coast (HSE, Fig. 4.8a) of the SI (21.7 % of 184 reanalyses at 00 and 12 UTC). The HSE regime causes weak pressure gradients and, therefore, weak surface winds in the vicinity of the SI. The second most common pattern was the southwest (SW) regime with an occurrence frequency of 17.9 %. This regime is characterized by a high pressure system northwest and a trough east of NZ resulting in a southwesterly flow incident on the SI (Fig. 4.8b). Other common patterns were, a high pressure system located over NZ with the strongest gradient and wind towards the south (H regime, not shown) with an occurrence frequency of 15.2 % and a high pressure system north of the North Island with a strong pressure gradient towards the south leading to a strong westerly flow (W regime, Fig. 4.8c). The latter flow regime is prone to excite MWs and was found for 9.8 % of the reanalyses. It prevailed for some consecutive days only at the end of July and beginning of August after the aircraft deployment concluded (ground-based lidar and radiosonde observations continued through this period at Lauder: see Kaifler et al. (2015) and Ehard et al. (2017)). Similar to the SW regime, a high pressure system close to the North Island on the west side caused a moderate south westerly flow on the SI (HNW, not shown, 7.6 %). A high pressure

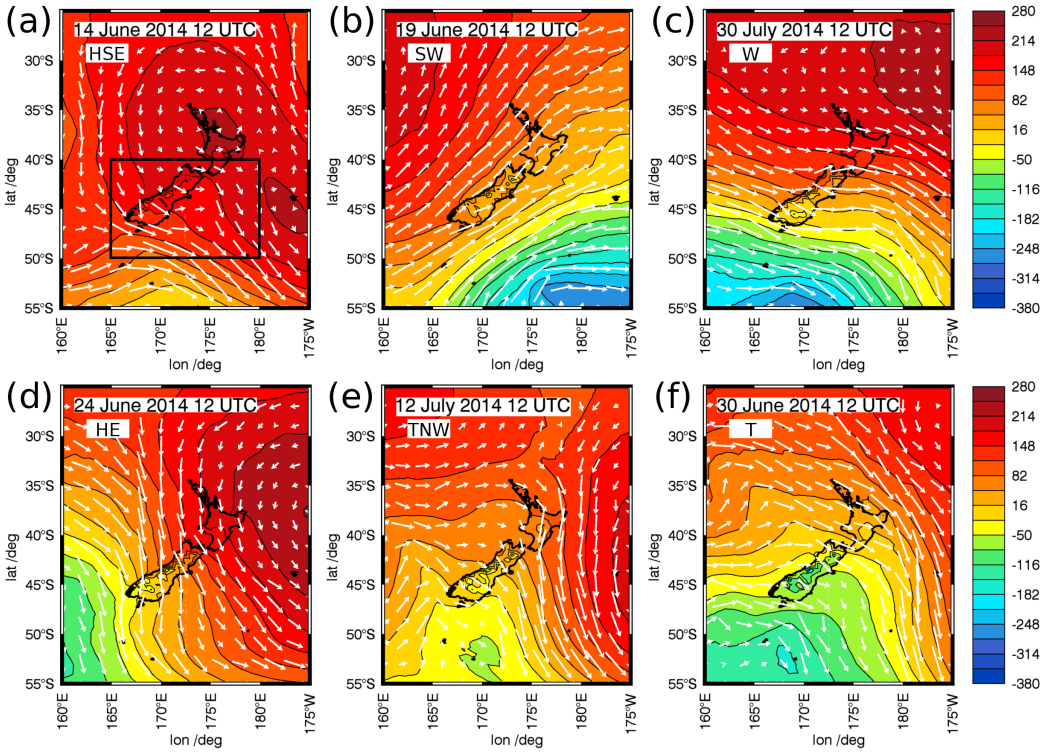

Figure 4.8: Selected examples of the ECMWF IFS 1000 hPa geopotential height (m) and horizontal wind at 850 hPa (white arrows) for weather regimes occurring during JJA 2014: (a) HSE (IOP 3, RF04), (b) SW (IOP 6, RF07), (c) W (GB21), (d) HE (IOP 8, RF09), (e) TNW (IOP 13, FF09), (f) T (IOP 9, RF13, FF01, FF02) . Box in (a) marks the area used for spatial mean profiles used in Fig. 3, 4 and 5.

system east (HE) of the North Island (5.4 % or 5 days) is associated with relatively strong northwesterly winds nearly perpendicular to the main ridge of the Southern Alps (Fig. 4.8d). Situations with a trough located west of NZ (TNW regime, Fig. 4.8e) causing northwesterly winds or the trough axis (T) directly above NZ resulting in a moderate westerly flow (Fig. 4.8f) occurred for 4.9 % and 4.3 % of the reanalyses, respectively. The other regimes occurred for less than 4 % of the reanalyses: They comprise a trough reaching on the east coast towards the northern part of NZ resulting in a weak S to SE flow over the SI (TSW regime), a low located northwest and a high located southeast of NZ causing a weak northeasterly flow (NE regime), a high pressure system west of the SI (HW) and a ridge bridge over the SI (R regime) characterized by weak pressure gradients and, therefore, weak surface winds in the vicinity of the SI (not shown). Comparing those findings to the values of Renwick (2011) for JJA of 1958-2010, the occurrence frequency was twice as high for the HSE regime in 2014 (21.7 % vs. 10.6 %), enhanced for the SW regime (17.9 % vs. 11.3 %) and strongly reduced for the T regime (4.3 % vs. 15.8 %). The mean duration of the different regimes was found

to be 1 to 2 days in the 40-year NCEP/NCAR reanalysis dataset (Kidson 2000). For JJA 2014, we found them to last mainly 1-4 days. The HSE blocking pattern persisted even longer in the first half of June. As already mentioned the W regime prevailed for some consecutive days only at the end of July and beginning of August.

Kidson (2000) grouped the twelve flow regimes into three classes representing the zonal group (H, HNW, W), the trough group (T, SW, TNW, TSW), and a blocking group (HSE, HE, NE, HW, R). During the winter months of his 40-year data set he calculated relative portions of 28 %, 40 %, and 32 %, respectively. Numbers of Renwick (2011) extending the analysis till 2010 only differ slightly (29 %, 39 %, 31 %). For JJA 2014, the relative group fractions are 33 %, 31 %, and 36 %, respectively. These numbers show that the trough group was underrepresented in JJA 2014 whereby the SW regime was the most common one of all trough group members. Altogether, the blocking regimes dominated during DEEPWAVE. The latter finding is especially true when the time period of the aircraft deployment (6 June to 20 July) is considered. In this period, the blocking group dominated even more (49 %) and the zonal group was underrepresented (11 %). Those findings agree with the indications of the climatological indices presented earlier (SOI, SAO): a tendency for southwesterly flow and blocking over NZ.

Table 4.3 lists the prevailing weather regimes of the IOPs when aircraft measurements sampling MWs were conducted in the region of the SI. Although the TNW regime was not one of the most common regimes, it occurred in four out of eleven IOPs (Tab. 4.3), namely in the IOPs 4, 8, 9 and 13 (Fig. 4.8e). More precisely, the TNW regime occurred on seven days (at 00 and/or 12 UTC) in total and a research flight sampling MWs was conducted on five of them. In the majority of those cases significant and strong MW activity was experienced at flight levels ($\approx$ 13 km for the NSF/NCAR GV and $\approx$ 10 km for the DLR Falcon, Fritts et al. (2016)). Although the SW regime was the second most frequent, only three IOPs with MWs as primary targets were conducted during this regime. It was the relatively weak cross-mountain wind component at 700 hPa which excluded further SW events as potential cases for aircraft deployments. Therefore, it is worth pointing out that moderate and even strong MWs were observed at flight level and also in the mesosphere and lower thermosphere (MLT) for IOP 6 (19 June, Fig. 4.8b) and IOP 10 (4 July, Smith et al. (2016)) in the SW regime. For the HE regime strong MWs and wave breaking were observed at flight level and by remote-sensing instruments during RF09 in IOP 8 (Fig. 4.8d, Fritts et al. (2016), Smith et al. (2016)). A prominent trough approached NZ from the west in IOP 13 resulting in the TNW regime (Fig. 4.8e) and a northerly to northwesterly flow, with moderate amplitude MWs being observed at flight level and a large scale MW was observed in the MLT at the last day of IOP 13 (Bossert et al. 2015). At this time the regime had already changed from TNW to TSW. For IOP 1, 3 and 15, which were classified as HSE regimes, i.e. weak pressure gradients and surface winds, mainly weak MW activity was reported at flight level and in the MLT. A complete summary of the reported GW activity during various IOPs can be found in Fritts et al. (2016).

Table 4.3: Weather regimes of DEEPWAVE IOPs focusing on MWs and trailing wavess (TWs) around the SI of NZ based on the available objective classification of NIWA using NCEP/NCAR reanalysis at 00 and 12 UTC. See table 4 of Fritts et al. (2016) for summaries of the research flights of the NSF/NCAR GV (RF) and of the research flights of the DLR Falcon (FF).

IOP	RF	FF	Date	Target	Weather regime	
					00 UTC	12 UTC
1	01		June 6	MW/TW/PF SI	HSE	HSE
3	04		June 14	MWs/TWs SI	HSE	HSE
4	05		June 16	MWs/TWs SI	HE	TNW
6	07		June 19	MWs/CWs/FWs E. Ocean	SW	SW
7	08		June 20	MWs/TWs SI	SW	W
8	09		June 24	MWs SI	HE	HE
	10		June 25	MWs/TWs SI	TNW	W
9	12	01/02	June 29	MWs/TWs SI	TNW	TNW
	13		June 30	MWs SI	TNW	T
	14		July 1	MWs/TWs SI	T	T
10	16	04/05	July 4	MWs/TWsSI	SW	SW
13	20	06	July 10	PF/MW SO SI	HE	HE
	21	07/08	July 11	MWs SI	HE	HE
		09	July 12	MWs SI	TNW	TNW
	22	10	July 13	MWs SI	TNW	TSW
15		12	July 16	MWs SI	HSE	HSE
			July 17	MWs SI	R	R
16	26		July 20	MWs SI along mountain ridge	TSW	TSW

4.2.2 Tropopause Layer and Jets

In this section the tropopause region and the impact of static stability and wind conditions on the wave propagation during DEEPWAVE is analysed. First the sharpness of the tropopause is investigated and a first estimate about its role in terms of wave reflection is made. Then, the properties of the tropopause jets (STJ, PFJ) and how they relate to the observed wave activity by altering forcing and propagation conditions are presented.

Tropopause Inversion Layer

The vertical change of wind and static stability at the tropopause modifies the properties of vertically propagating GWs following the dispersion relationship (e.g. Eckermann and Vincent 1993, Keller 1994, Grise et al. 2010, Shibuya et al. 2015). The height of the tropopause, its sharpness and the associated shear varied markedly during DEEPWAVE due to the presence or absence of tropopause jets originating either from the subtropics or the polar region under winter time conditions (e.g. Manney et al. 2014). The height of the thermal tropopause (WMO 1957) varied with migratory weather systems. During JJA 2014, the altitude of the thermal tropopause fluctuated between 8 and 13 km altitude as revealed by Lauder radiosonde and ECMWF IFS temperature profiles (not shown). Moreover, the static stability as given by the squared Brunt-Väisälä frequency (Eq. (2.32)) usually maximizes right above the thermal tropopause (Birner et al. 2002). The associated TIL is a global feature of the upper troposphere and lower stratosphere (UTLS) (Birner 2006, Grise et al. 2010, Gettelman et al. 2011). Here, we characterize the evolution of the tropopause layer in JJA 2014 by calculating its sharpness in terms of the TIL strength.

Following Gettelman and Wang (2015), the characteristics of the TIL were examined using vertical N^2 profiles derived from ECMWF IFS 6-hourly operational analyses averaged over an area covering the SI of NZ (shown by the box in Fig. 4.8a), which in large part eliminates the signatures of GWs. The TIL strengths on the bottom and upper sides relative to the mean values over JJA 2014 are given by

$$TIL'_{strength,UT} = \frac{1}{2}(N^2_{MAX} - N^2_{MIN,UT}) - \underbrace{\left\langle \frac{1}{2}(N^2_{MAX} - N^2_{MIN,UT}) \right\rangle_{JJA}}_{\text{mean } TIL_{strength,UT}} \tag{4.4}$$

and

$$TIL'_{strength,LS} = \frac{1}{2}(N^2_{MAX} - N^2_{MIN,LS}) - \underbrace{\left\langle \frac{1}{2}(N^2_{MAX} - N^2_{MIN,LS}) \right\rangle_{JJA}}_{\text{mean } TIL_{strength,LS}} \tag{4.5}$$

respectively (Fig. 4.9a).

N^2_{MAX} is the maximum of N^2 in the UTLS below 20 km altitude, $N^2_{MIN,UT}$ is the minimum of N^2 in the upper troposphere below the altitude of N^2_{MAX} but above 5 km altitude and $N^2_{MIN,LS}$ is the first local minimum of N^2 in the lower stratosphere above the altitude of N^2_{MAX}, where the vertical gradient of N^2 changes from negative to positive. Positive values of the two quantities calculated by Eqs. (4.4) and (4.5) characterize a peak in N^2 in the UTLS which is exceeding the static stability of the stratosphere. Figure 4.9b illustrates the different quantities by means of three individual N^2 profiles. The mean $TIL_{strength,UT}$ averaged over the three winter months JJA 2014 is 2.6×10^{-4} s^{-2} and the mean $TIL_{strength,LS}$ equals to 0.96×10^{-4} s^{-2}. The

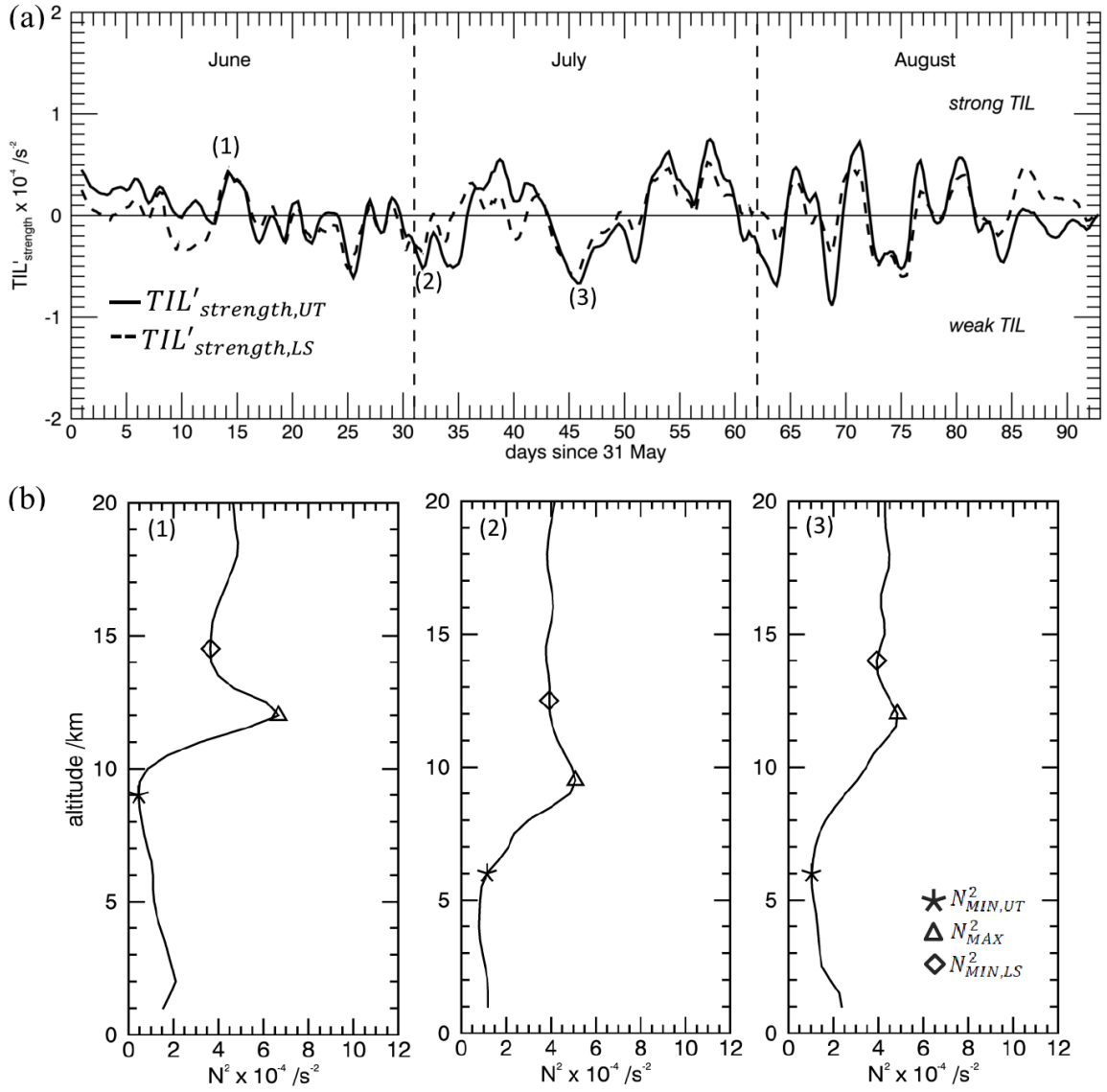

Figure 4.9: (a) TIL characteristics $TIL'_{strength,UT}$ (black solid) and $TIL'_{strength,LS}$ (black dashed) as 24-h running mean based on 6-hourly ECMWF analysis. (b) Examples of mean profiles of N^2 from which TIL characteristics were calculated are taken on (1) 14 June 2014 (IOP3, RF04), (2) 2 July 2014 (after IOP9, RF14), and (3) 16 July 2014 (IOP 15, FF12). Symbols mark $N^2_{MIN,UT}$ (star), N^2_{MAX} (triangle) and $N^2_{MIN,LS}$ (diamond).

mean $TIL_{strength,UT}$ for JJA 2014 is comparable to the values of the annual climatology from 32 years of ERA-Interim data as shown in Fig. 7 of Gettelman and Wang (2015), while the mean $TIL_{strength,LS}$ was larger ($\approx 0.6 \times 10^{-4}$ s^{-2} vs. 0.96×10^{-4} s^{-2}). This enhancement can probably be explained by the presence of weak GWs signals still

contained in the spatial mean profiles in the lower stratosphere altering the N^2 values in the lower stratosphere (see for example wavy structures between 13 and 20 km altitude in Fig. 4.9b).

Generally, the TIL is well pronounced when the two quantities $TIL'_{strength,UT}$ and $TIL'_{strength,LS}$ are positive, which means there is a pronounced peak (i.e. large strength) in stability (Fig. 4.9a, an example profile is shown in Fig. 4.9b(1)). The TIL is weak when $TIL'_{strength,UT}$ and $TIL'_{strength,LS}$ are negative, which means there is no pronounced peak (i.e. small strength) in stability (Fig. 4.9a, two example profiles are shown in Fig. 4.9b(2,3)). Besides the variability of the TIL characteristics, periods of some consecutive days with a strong and well pronounced TIL are found in Fig. 4.9a in the middle of June and in the first and second half of July. During those days the SI was influenced by high pressure systems (namely HSE, HE, H regimes), i.e. anticyclones, which are known to have pronounced TIL characteristics (Wirth 2003, 2004).

Hydrostatic Reflection Coefficient

While the reflection of non-hydrostatic GWs at the tropopause is a function of wavenumber and depth of the tropopause, the hydrostatic reflection coefficient (Eliassen and Palm 1960) can be easily calculated for large Richardson number ($Ri >> 1/4$), i.e., no or negligible vertical shear, according to

$$r \approx \frac{N_S - N_T}{N_T + N_S}, \tag{4.6}$$

where N_T and N_S are the representative mean Brunt-Väisälä frequencies of the troposphere and the stratosphere (compare to Eqs. (4.2) and (4.3)). A reflection coefficient of 1 reveals total reflection of hydrostatic GWs. For typical mid-latitude conditions $N_S = 2 - 4 \times N_T$, such that the reflection coefficient varies between 0.33 and 0.6 indicating a partial reflection of vertically propagating hydrostatic GWs (Gill 1982). We use this as a first simple approach to investigate the influence of the TIL on wave propagation being aware that we neglect the influence of the vertical shear, the depth of the TIL and the influence of the wave's vertical wavelengths. The reflection coefficient was evaluated using two different methods for the period JJA 2014: First, mean values of N_T and N_S were calculated for selected layers in the troposphere ($z = 3 - 6$ km) and the stratosphere ($z = 16 - 19$ km). Secondly, instead of using the mean stratospheric value N_S in Eq. (4.6), N_{MAX} in the UTLS was taken in order to evaluate the influence of the TIL on the magnitude of the reflection coefficient. Figure 4.10a shows both results computed for JJA 2014. The reflection coefficient varies between 0.25 and 0.41 when the mean tropospheric and stratospheric stabilities are considered. The reflection coefficient becomes significantly larger if the enhancement of static stability by the TIL is taken into account. Maximum values often exceed $r = 0.5$ and values of up to 0.63 were calculated for a short period near the end of July 2014.

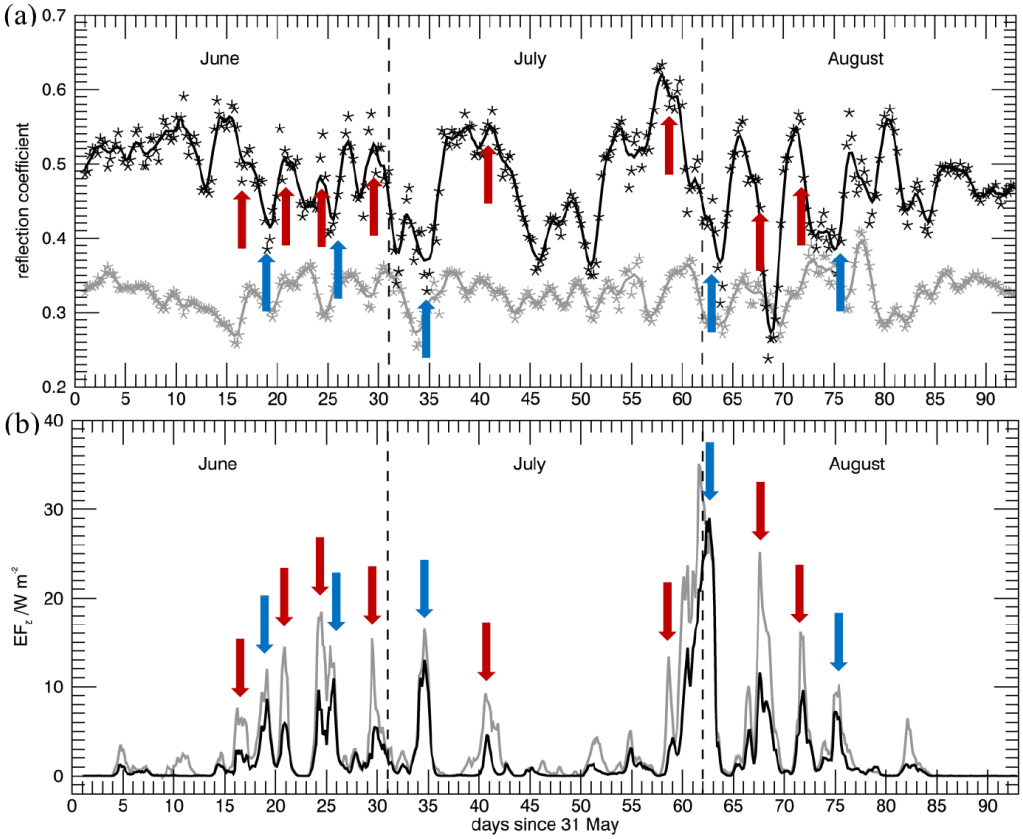

Figure 4.10: (a) Hydrostatic reflection coefficients r ($Ri >> 1/4$) from ECMWF 6-hourly operational analyses (stars) and 24-h running means (solid lines) using an averaged stratospheric value of N (gray) and N_{MAX} taken in the UTLS (black). (b) 3-hourly regional vertical energy fluxes over SI computed from WRF constrained by MERRA2 initial conditions at 4 km (gray) and 12 km (black) altitude, respectively. Arrows mark the GW events, when the reflection coefficient is close to or larger than 0.5 and the EFz at 12 km is reduced by 47-77 % (red) from the 4 km value and when the reflection coefficient is close to or smaller than 0.4 and the EFz is reduced by < 35 % (blue). (WRF data provided by C. Kruse)

We compared the temporal evolution of the reflection coefficient calculated with the N_{MAX} values (black stars in Fig. 4.10a) with the regional vertical energy fluxes (EFz) over the SI derived from the long-term Weather Research and Forecasting Model (WRF) simulations (Fig. 4.10b, WRF data provided by C. Kruse). Only MW episodes, i.e. 6-hourly values with EFz ≥ 6 W m^{-2} at 4 km altitude, were considered. When the reflection coefficient is close to or larger than 0.5, EFz-values at 12 km altitude were reduced by 47-77 % (20th and 80th percentile, i.e. for 16 out of 20 points in time the reduction was larger than 47 %) compared to the EFz-values at 4 km altitude (red arrows mark those events in Fig. 4.10). The reduction is below 35 % (80th percentile,

i.e. for 12 out of 15 points in time the reduction is below 35 %) when the reflection coefficient is close to or below 0.4 (blue arrows mark those events in Fig. 4.10). The simulated reduction of the EFz for a given value of the reflection coefficient is larger than predicted by linear theory, where net upward flux is $(1 - r^2)$ times the flux of the incident wave (Eliassen and Palm 1960). This means for $r = 0.5$ one would expect a reduction of EFz by 25 % rather than 50 %. This discrepancy might be explained by the fact that reflection due to vertical shear is not considered in the approximated r given by Eq. (4.6) and vertical shear certainly played a role during the GW events (e.g. Fig. 4.11d). Nevertheless, the Pearson correlation coefficient between the reflection coefficient based on N_{MAX} and the EFz reduction (between 4 and 12 km) is 0.70 when the 6-hourly values of the events marked by arrows in Fig. 4.10 are considered. Therefore, the relationship between the reflection coefficient and the EFz reduction in the lower stratosphere highlights the impact of the TIL on the vertical propagation of MWs. A stronger TIL enhances the reflection of MWs and, thus reduces the vertical energy flux. This is in agreement with the findings from idealized simulations in Sec. 4.1.

Subtropical and Polar Front Jets

In addition, the tropopause jets (STJ and PFJ) were analysed based on the method by Gallego et al. (2005) where the jets are determined by searching for closed circumpolar 200 hPa geostrophic streamlines showing the largest mean horizontal wind speed along the streamline. Here, operational ECMWF IFS analyses of geopotential heights and horizontal winds at 200 hPa were used. From the results, the zonally averaged positions and strengths of the STJ and the PFJ were determined for the 06 UTC analyses (Fig. 4.11a, c). The STJ dominated the circulation with a mean wind speed of 51 m s^{-1} and its mean location being at 31° S. The PFJ was present on only half of the days in June but was more frequent in July and August (more than 80 % of the days). Its mean wind speed was 39 m s^{-1}, which is more than 10 m s^{-1} slower than the STJ, and the mean location was at 56° S. This matches the climatological findings presented by Gallego et al. (2005). Although the connection mentioned above between the SAM index and the strength of STJ and PFJ (Sec. 4.2.1) does not hold for daily values, it matches for temporally averaged values. While the daily SAM index was mainly positive in June and the first half of July (Fig. 4.7) the mean strengths of the STJ and the PFJ were 51 m s^{-1} and 38 m s^{-1}, respectively. For the second half of July, when the daily SAM index was mainly negative, the mean strengths of the STJ and the PFJ were 55 m s^{-1} and 36 m s^{-1}, respectively. The difference in wind speed is small but the SAM index was not as positive or negative as for other years represented by the gray area in Fig. 4.7.

Since the focus of this study is on the SI of NZ, the location of the jets was also analysed at a longitude of 169° E (Fig. 4.11b). At that longitude, the STJ was located south

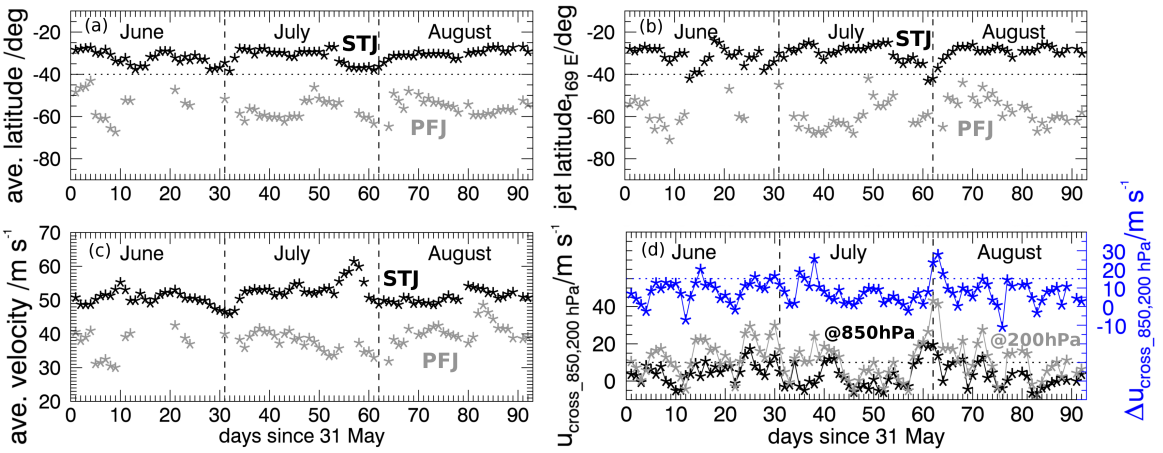

Figure 4.11: Zonally averaged latitudes (a) and strengths (c) of the STJ (black stars) and the PFJ (gray stars) in JJA 2014. Panel (b) shows the latitudes of the STJ and the PFJ at 169° E. Operational IFS analyses at 200 hPa at 06 UTC were analysed using the method presented by Gallego et al. (2005). Panel (d) shows the cross mountain (NW direction) velocity of operational IFS analyses averaged over NZ area at 850 hPa (black) and 200 hPa (gray) and their difference, e.g. vertical shear between 850 and 200 hPa (blue).

of 35° S on 13-15 June (IOP 3), 24 June (IOP 8), 28-29 June (IOP 9) and 31 July-2 August (GB 21). On 13 June and 31 July-1 August the location was even south of 40° S. The PFJ was located north of 52° S at a longitude of 169° E at the beginning of June, on 21 June (GB 10), 1 July (IOP 9), 19-20 July (IOP 16), 24 July and on some days in August (4, 7, 9, 11-13). On 1 and 19 July and 7 and 11 August the PFJ was located even north of 47° S. The locations of the PFJ and STJ were compared with the GW activity reported in the flights summaries of the DEEPWAVE IOPs (Table 4 in Fritts et al. (2016)). Whenever the STJ was located close to the SI, MWs and sometimes even jet-stream-induced GWs were observed at flight level, in the stratosphere and the MLT. Additionally, wave breaking and turbulence at flight level were reported for these events. For the cases when the PFJ was located close to the SI, weak MW activity at flight level was reported. Yet, surprisingly strong MW activity in the stratosphere and the MLT were also reported. This suggests that the presence of the STJ was associated with stronger forcing conditions and larger positive (negative) vertical shear below (above) the jet maximum. These conditions not only triggered strong MWs but also affected the wave propagation and led to wave breaking in the UTLS. The presence of the PFJ was linked with weaker forcing but the triggered MWs could propagate further up leading to strong MW signals in the MLT. The difference in the forcing conditions and in the vertical shear between the STJ and the PFJ is largely confirmed by the cross mountain wind (northwesterly direction) at 850 hPa and 200 hPa from IFS analyses averaged over the NZ area as shown in Fig. 4.11d. When the STJ was close

to the SI (e.g. 14 June, 24 June, 29 June, 31 July-1 August) cross mountain winds at 850 hPa were often larger than 10 m s^{-1} and at 200 hPa larger than 20 m s^{-1} leading to a larger vertical shear, i.e. differences of around 15 m s^{-1} and more between 850 and 200 hPa, (blue curve in Fig. 4.11d). This was different when the PFJ was close to the SI (e.g. 1-4 June, 19-24 July) where the cross mountain winds at 850 hPa and 200 hPa hardly reach 10 m s^{-1} because the PFJ is generally weaker than the STJ and approaches NZ from its mean location from the south (see previous paragraph). The Pearson correlation coefficients between the latitude of the STJ and the cross mountain wind at 850 hPa and 200 hPa are -0.46 and -0.47, respectively. The negative sign comes from the negative latitudes used for the Southern Hemisphere. Those analyses support the findings of Kaifler et al. (2015) and the hypothesis that the PFJ is the main driver when weak and moderate MW activity were observed in the UTLS and large amplitudes in the MLT.

4.3 Gravity Wave Activity and Properties from Radiosonde Data

The non-dimensional mountain height (Eq. 2.38) was computed based on altitude data from the Navy 10-minute global elevation dataset[7]. The dataset provides inter alia the maximum and modal elevation for areas of 10 minutes × 10 minutes each. Figure 4.12 shows the largest values of the maximum elevation among all latitudes between 35 and 50° S for longitudes between 165 and 180° E. The largest value of the maximum elevation between 167 and 173.5° E is about 3750 m, i.e. Mount Cook, and the smallest value of the maximum elevation is about 1700 m. This smallest value of the maximum elevation is close to the modal elevation of the main mountain range of the SI which describes the mountain range apart from the highest peaks (Fig. 4.12).

Mean wind speed of ECMWF upstream profiles (u_c computed for profiles in the according upstream region westerly, northerly, easterly or southerly of the SI), which were interpolated on a 500 m grid in the vertical between 0 and 3500 m and 1500 m, respectively, is used as representative horizontal velocity. The non-dimensional mountain height is always larger than 1 based on the highest peak of 3750 m (black curve in Fig. 4.13) which suggest that upstream blocking of the flow occurred. The non-dimensional mountain height is often around 1 when the modal elevation of 1700 m is used (39 % of the time, gray curve in Fig. 4.13). This is found for all IOPs except

[7]Fleet Numerical Meteorology and Oceanography Center/U.S. Navy/U. S. Department of Defense, 1980: U.S. Navy 10-Minute Global Elevation and Geographic Characteristics. Research Data Archive at the National Center for Atmospheric Research, Computational and Information Systems Laboratory, Boulder, CO. [Available online at http://rda.ucar.edu/datasets/ds754.0/], accessed 13 Apr 2017.

IOP 3 (13/14 June) and IOP 15 (16/17 July). It must be ensured that linear wave solutions are largely valid due to the fact that wave properties can only be derived based on linear wave solutions (here 2D). This seems to be the case for most of the IOPs if the modal elevation of 1700 m is considered. Moreover, the linear solution can also be a solution of the non-linear equations due to relatively constant wind and static stability in the stratosphere up to 27 km altitude (cf. Sec. 2.1).

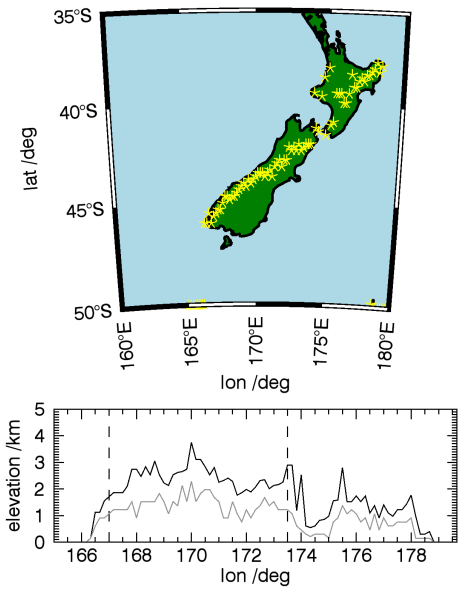

Figure 4.12: Location of the maximum elevation (areas of 10 minutes × 10 minutes) among all latitudes between 35 and 50 S given for longitudes between 165 and 180 E (top) and the maximum elevation (black) and the modal elevation (gray) for these areas of 10 minutes × 10 minutes.

In the following subsections, the analysis methods introduced in Sec. 3.2.4 are used and GW activity and characteristics of low- to high-frequency GWs in the troposphere and stratosphere are determined. GW characteristics such as horizontal wave scales and wave energy propagation directions are important for evaluating the sources of the GWs in the radiosonde measurements and investigating MW activity in relation to the tropopause. First, the horizontal velocity measurements are analysed for interia-GWs, i.e. the low-frequency part of the GW spectrum. Second, the balloon ascent rates are analysed for medium- to high-frequency MWs. A non-MW case is compared to three MW cases to investigate if the vertical velocity perturbations, which are determined from the balloon ascent rate, are indeed caused by MWs. This comprehensive characterization of a large part of the GW spectrum allows the discussion (Sec. 5) of the mountains being the GW source and of the influence of the tropopause on stratospheric MW activity in the mountainous region of NZ during DEEPWAVE.

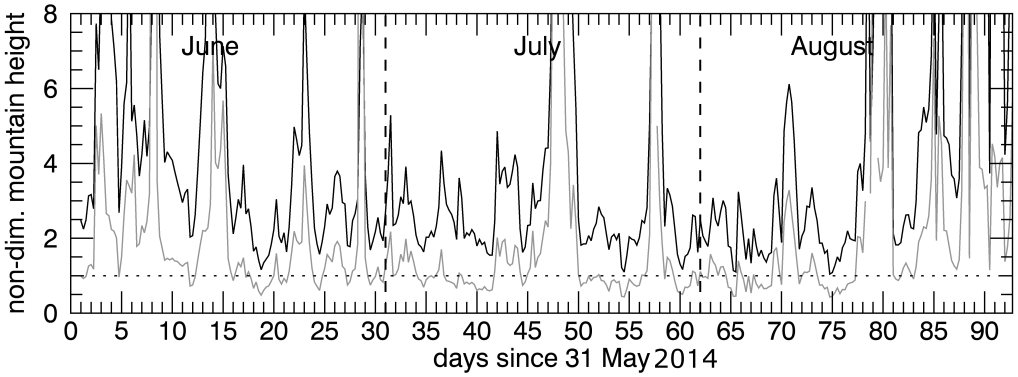

Figure 4.13: The Non-dimensional mountain height computed from mean ECMWF upstream wind speed between 0 and 3500 m altitude and a mountain height of about 3750 (black) and between 0 and 1500 m altitude and a mountain height of about 1700 m (gray). The dotted horizontal line marks a value of 1 above which non-linearity and blocking effects become important.

4.3.1 Intertia-Gravity Waves

Gravity wave energy

Horizontal kinetic and potential GW energy per mass (Eq. (3.10) and (3.12)) were averaged for each IOP for troposphere (1-8 km) and stratosphere (13-27 km) (Fig. 4.14). For simplicity, the overbar ($\overline{KE}$ and $\overline{PE}$) indicating vertical mean values is omitted from now on and simply *KE* and *PE* are used. *KE* is highly variable for the IOPs. *KE* is between 6.0 J kg^{-1} and 15.6 J kg^{-1} and has a mean value of 9.6 J kg^{-1} in the troposphere. The maximum is 22.5 J kg^{-1} and the mean value is 13.0 J kg^{-1} in the stratosphere . *PE* is smaller than *KE* with mean values being 4.3 J kg^{-1} in the troposphere and 6.9 J kg^{-1} in the stratosphere. The largest mean values for *KE* and *PE* in the stratosphere are determined for GB 21. In addition, the minimum and maximum energies during an IOP are marked by bars in Fig. 4.14. This highlights the variability of the GW energies during the IOPs which is caused by changing background conditions (cf. Sec. 4.2.1). For example, IOPs 8, 9 and 13 which are characterized by changing tropospheric regimes (HE, TNW, T, TSW) show the largest variability of *KE* and *PE* in the troposphere.

The ratio between *KE* and *PE* is 3.1 in the troposphere and 2.3 in the stratosphere on average. This can be explained by an enhanced energy near f. Near-inertial frequency waves oscillate almost horizontally and wave energy is essentially kinetic (Vincent et al. 1997). An enhanced energy near f is reasonable as it was already mentioned in Sec. 3.2.3 that horizontal *KE* is most sensitive to low-frequency GWs.

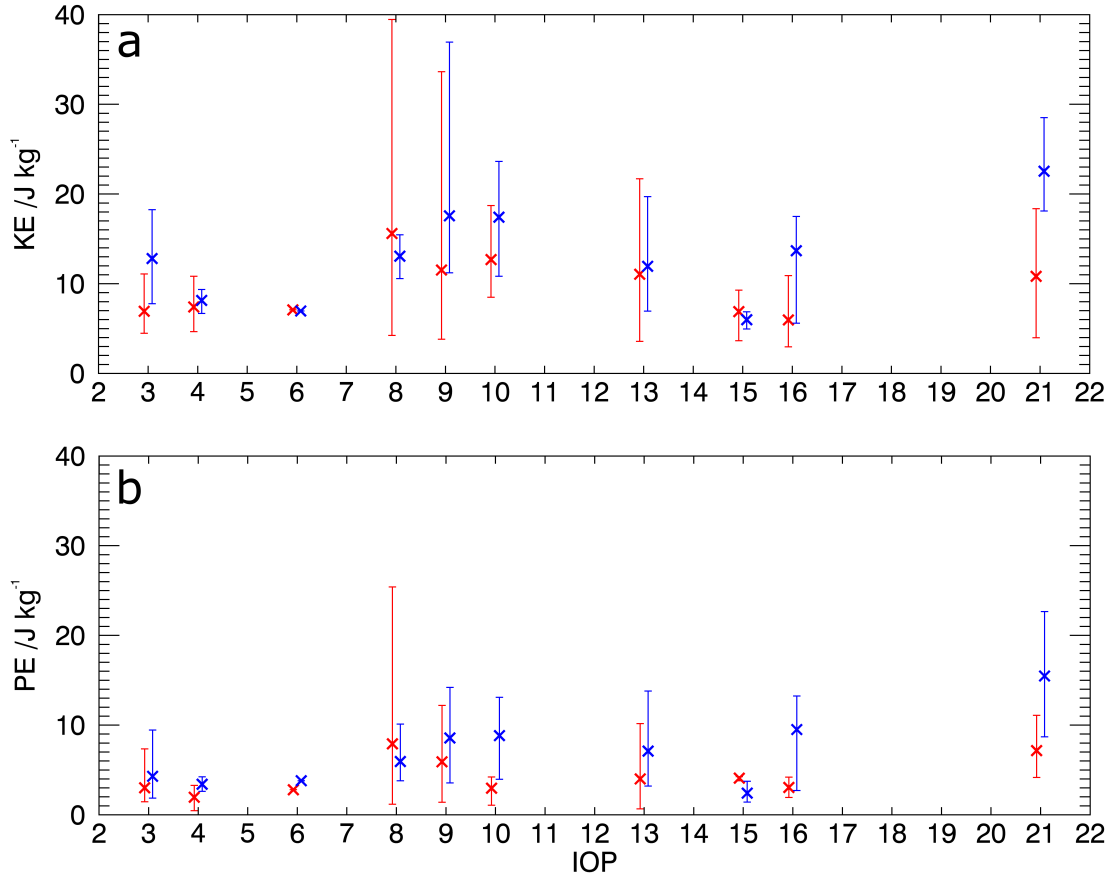

Figure 4.14: Mean (a) horizontal kinetic and (b) potential GW energies for all IOPs for troposphere (red x) and stratosphere (blue x). Bars mark the minimum and maximum values occurring during an IOP. Number of soundings analysed for each IOP can be found in Table 3.1

Rotary Spectra

Rotary spectra (Sec. 3.2.4) have been calculated for the Lauder soundings and averaged over the IOPs. The number of soundings contributing to the averaged spectra are different for the different IOPs (Tab. 3.1). That is because the time periods of the IOPs vary, the time interval between the release of soundings varies, and as already mentioned above some soundings are not included because their maximum altitude reached is below 27 km or they have gaps or bad data (e.g., downward motion of the balloon). The ratio (R) between the upward propagating power and the sum of upward and downward propagating power (Eq. 3.13) for all IOPs is shown in Fig. 4.15. Dominant upward wave energy propagation ($R > 0.6$) is found for nearly all IOPs for

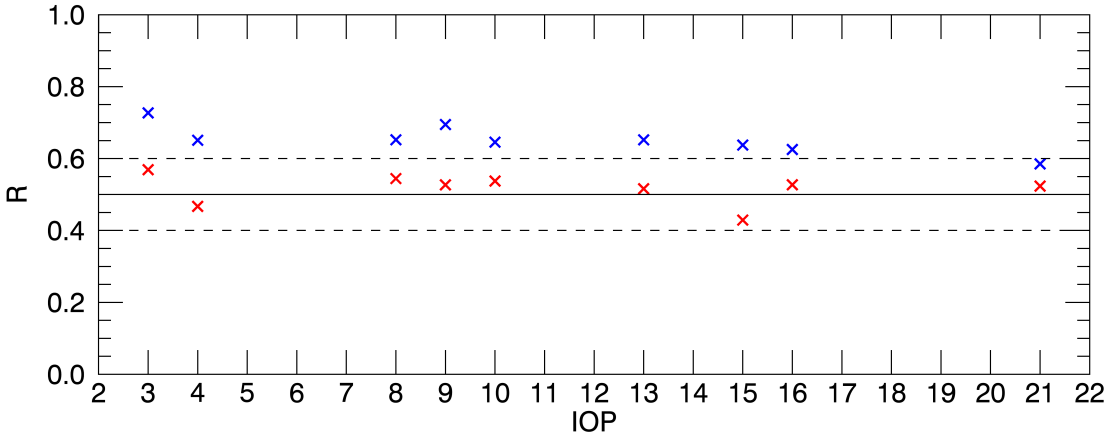

Figure 4.15: Ratio of the upward propagating part of the rotary spectra with the total power of upward and downward propagation integrated over all wave numbers for the Lauder radiosoundings for troposphere (red x) and stratosphere (blue x). A ratio below 0.4 or above 0.6 stands for dominant downward and upward energy propagation, respectively.

the stratosphere. No dominant propagation direction is revealed for the troposphere as all values are close to 0.5.

Stokes Analysis

In the following, GW properties of inertia-GWs derived from Stokes analysis (Sec. 3.2.4) are presented. The given characteristics are valid for the dominant wave modes in the troposphere and stratosphere, respectively. Meaningful results are only obtained if coherent wave motions dominate the velocity perturbations. The degree of polarization (d) is a quantity which shows whether coherent waves are present (Eckermann and Vincent 1989, Vincent and Alexander 2000). Over all, d is larger than or equal to 0.5 for 67 % of the soundings in the troposphere and for 47 % of the soundings in the stratosphere. Values smaller than 0.4 occur for 18 % of the soundings in the troposphere and for 26 % of the soundings in the stratosphere. The influence of the soundings with a low degree of polarization on the determined mean wave characteristics is evaluated in Appendix A.1.

The dominant vertical propagation direction from Stokes analysis is determined for every sounding for troposphere and stratosphere. The partitioning in upward and downward propagating soundings reveals dominant upward propagation for nearly all soundings (97 %) in the stratosphere but only for 56 % of the soundings in the troposphere. This is in agreement with the results from rotary spectra (Fig. 4.15)

where no dominant vertical propagation direction was found for the troposphere. The dominant intrinsic horizontal phase propagation direction was found to be mainly towards NW in the troposphere and towards W to S in the stratosphere (for details see Appendix A.1). IOP 6 (SW regime) and IOP 16 (TSW regime) are the only events with a nearly southward intrinsic horizontal phase propagation in the troposphere. It was found that the intrinsic horizontal phase propagation is in many cases against the mean wind when the mean intrinsic horizontal phase propagation directions of the IOPs are compared to the mean wind directions from soundings for troposphere and stratosphere. The difference between the propagation direction and the mean wind direction is smaller than 30° for all IOPs except IOP 15 and IOP 16 in the troposphere. The tropospheric propagation direction even is along the mean wind for IOP 15 . The difference between the propagation direction and the mean wind direction is larger with 40 to 70° for IOP 4, 6 and 21 in the stratosphere.

The mean difference for a single sounding between the horizontal propagation directions revealed by the two methods which were described in Section 3.2.4, i.e. from Stokes parameters or directly from covariances, is 27°. The maximum difference for a single sounding is 87°. The mean difference is found to be smaller being 12° when the mean propagation directions of the IOPs revealed by the two methods are compared (for details see Appendix A.1). The good agreement between the two methods for the mean propagation directions increases the confidence in the results. Of course both methods are based on the same idea of determining the horizontal propagation direction but the technical implementation is different.

Histograms of the intrinsic frequencies from Stokes parameters for all analysed Lauder sounding are shown in Figure 4.16. Intrinsic frequencies larger than $20f$ are determined for 7.5 % and 3.0 % of the soundings for troposphere and stratosphere, respectively (not shown). This low percentage suggest that the data going into Stokes analysis mainly contain inertia-GWs, especially in the stratosphere. The determined frequencies tend to be more variable in the troposphere. Stratospheric mean intrinsic frequencies for the IOPs are mainly one to three times the inertial frequency.

Vertical and horizontal wave numbers/wavelengths

The distributions of the vertical wavelength for troposphere and stratosphere are given in Figure 4.17a, b . Tropospheric vertical wavelengths tend towards a bit larger values than stratospheric vertical wavelengths. Overall the dominant vertical wavelengths lie between 2 and 4 km. The distributions of the calculated horizontal wavelength for troposphere and stratosphere are shown in Figure 4.17b, c. The horizontal wavelengths derived for the troposphere are significantly smaller than for the stratosphere. In the troposphere most of the soundings are dominated by horizontal wavelengths smaller

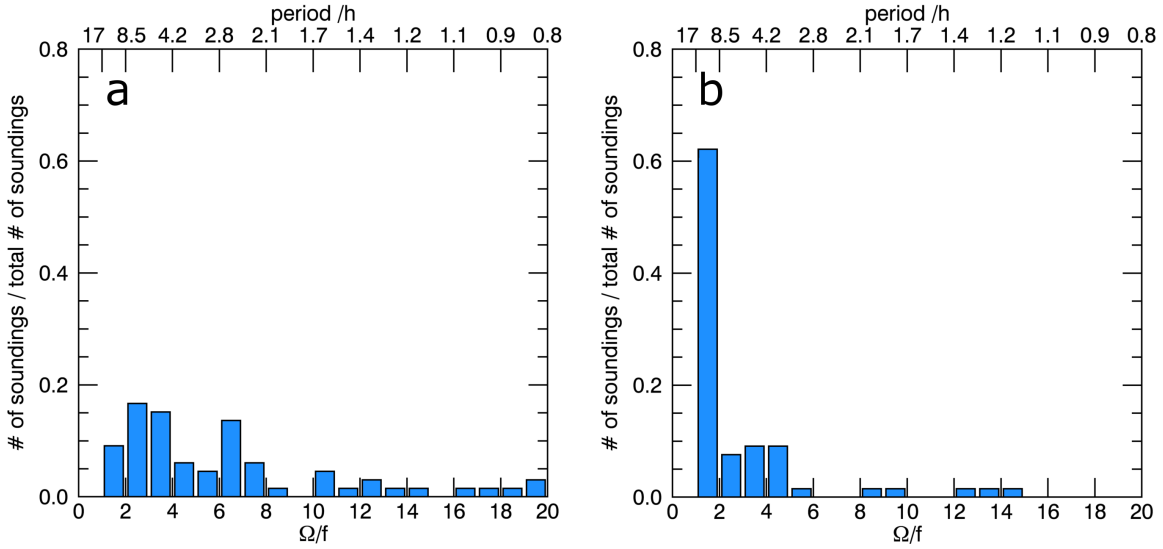

Figure 4.16: Distribution of the intrinsic frequencies with respect to f derived from Stokes analysis for troposphere (a) and stratosphere (b) for all Lauder soundings. Top axis gives the corresponding period ($2\pi/\Omega$) in hours.

than 200 km. For the stratosphere the distribution is much broader containing also larger horizontal wavelengths (further details in Appendix A.1).

Phase speed and group velocity

The distributions of the horizontal intrinsic and ground-based phase speeds in the stratosphere are shown in Fig. 4.18a, b. Stratospheric intrinsic horizontal phase speeds have a mean value of 13.9 m s^{-1}. Tropospheric intrinsic horizontal phase speeds are often smaller than 10 m s^{-1} with a mean value of 7.6 m s^{-1} (for more details see Appendix A.1). The sign of the ground-based horizontal phase speeds is negative for 68 % of the soundings in the stratosphere. The Doppler shift due to the horizontal wind causes a change of the direction of the phase speed relative to the ground compared to the direction of the intrinsic phase speed. The mean value of the absolute ground-based phase speeds (sign neglected) is larger for the troposphere (12.4 m s^{-1}, Appendix A.1) than for the stratosphere (8.4 m s^{-1}, Fig. 4.18b). The direction of the ground-based phase speed is mainly towards eastward directions (between 0 and 180 deg) going with the mean wind (not shown).

Vertical phase speeds (Fig. 4.18b, c) are an order of magnitude smaller than the horizontal phase speeds. The negative and positive values of the intrinsic vertical phase speed are based on the vertical energy propagation found by Stokes analysis. It revealed dominant downward phase propagation in the stratosphere (Fig. 4.18c), i.e. dominant

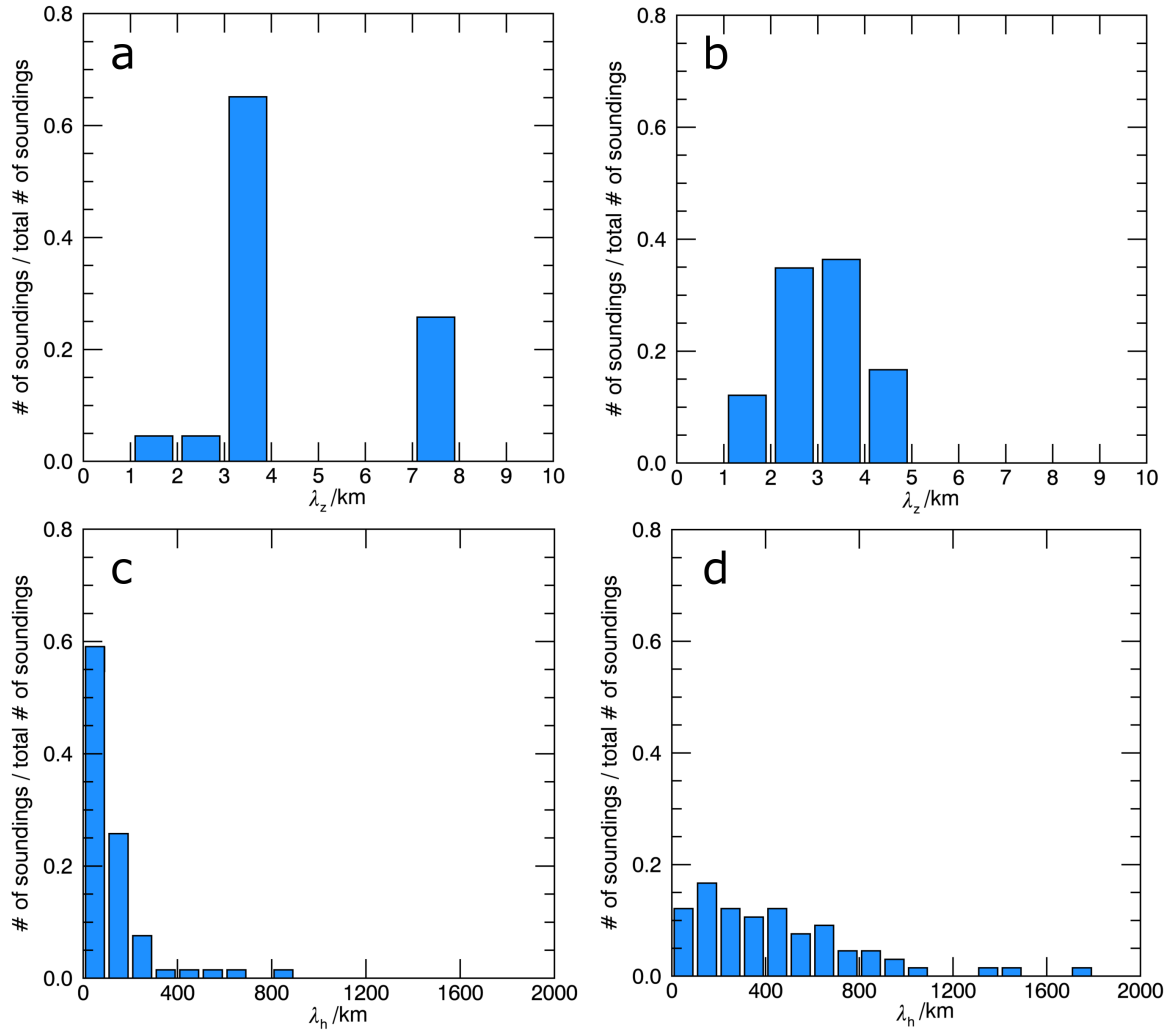

Figure 4.17: Distribution of the vertical wavelength for troposphere (a) and stratosphere (b) and of the horizontal wavelength for troposphere (c) and stratosphere (d) for all Lauder soundings.

upward energy propagation. The mean values of the absolute values of the intrinsic vertical phase speeds are 0.70 m s^{-1} and 0.26 m s^{-1} for troposphere (for details see Appendix A.1) and stratosphere, respectively. As for the horizontal ground-based phase speed, one finds a change of the sign in the ground-based vertical phase speed compared to the intrinsic vertical phase speed for 68 % of the soundings in the stratosphere. This is because the condition for the change of the sign of the ground-based phase speed compared to the intrinsic phase speed is equal for the horizontal and vertical phase speeds. If the horizontal wind causes the sign of the phase speed to change in the horizontal, it must also change in the vertical. The ground-based group velocities

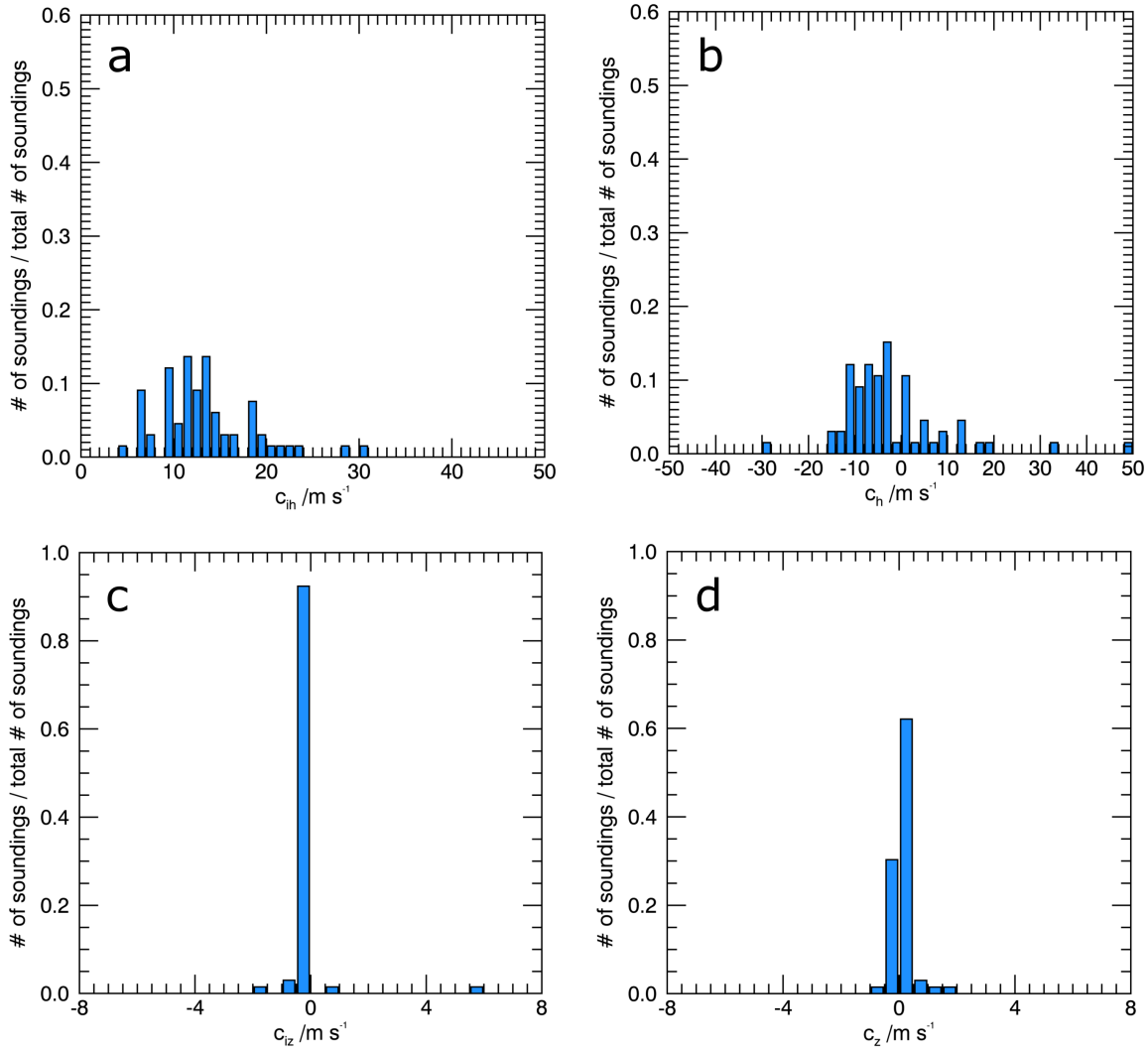

Figure 4.18: Distribution of the intrinsic (left) and ground-based (right) horizontal phase speed (top) and vertical phase speed (bottom) in the stratosphere for all Lauder soundings.

were calculated with Eqs. (2.21)-(2.24). Figure 4.19a-d shows the distribution of the horizontal group velocity and its direction. The dominant direction of the group velocity and therefore of the GW energy propagation is eastward. More variability is found for the troposphere (Fig. 4.19c). The horizontal group velocity is dominated by the zonal wind and its mean absolute value (ignoring direction) over all soundings is 17.1 m s^{-1} for the troposphere and 16.9 m s^{-1} for the stratosphere. These non-zero values of the horizontal group velocity point to horizontally propagating GWs. The distribution of the vertical group velocity is shown in Figure 4.19e, f. The mean absolute value (ignoring direction) of the vertical group velocity is 0.69 m s^{-1} for the troposphere

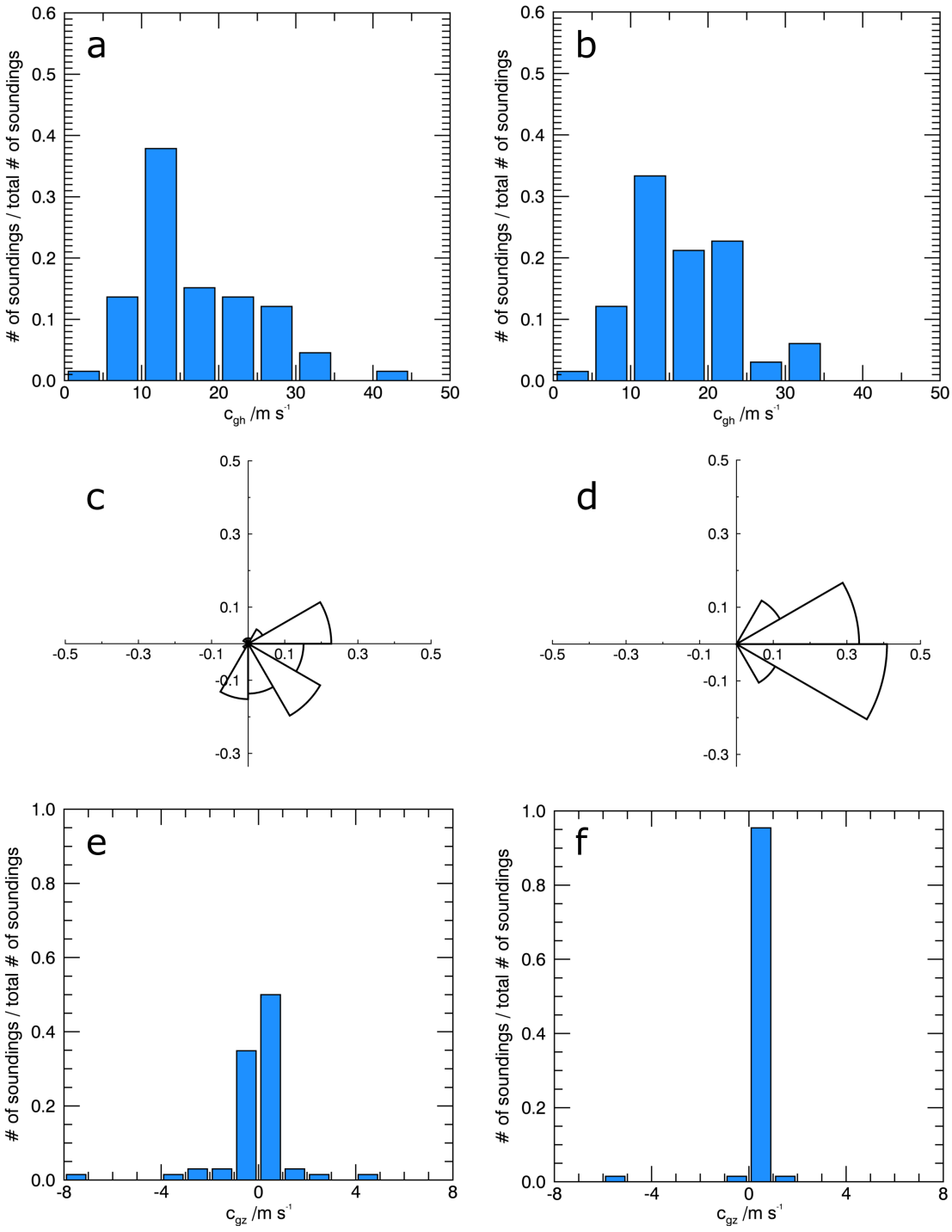

Figure 4.19: Ground-based horizontal group velocity for troposphere (a, c) and stratosphere (b, d). Top panels (a, b) show the distribution of the amplitude of the horizontal group velocity and middle panels (c, d) the distribution of the direction of the horizontal group velocity. Bottom panels show the ground-based vertical group velocity for troposphere (e) and stratosphere (f).

and 0.24 m s^{-1} for the stratosphere. This means the GW energy propagates faster horizontally than vertically.

Hydrostatic mountain waves in the rotating regime

If it is assumed that the inertia-GWs are linked to the mountains, i.e. long stationary hydrostatic waves in the rotating regime, their horizontal wavenumber k_h can be computed from the intrinsic frequency. Horizontal wavenumber and intrinsic frequency are directly related for stationary waves (Eq. (2.27)). The assumption that the sounding reveals the true dominant vertical wavelength (Fig. 4.17), which was used above, is replaced by the assumption of stationarity (Sec. 3.2.4). The vertical wavelength of hydrostatic MWs is known to be more likely around 6-10 km than 2-4 km.

Distributions of the horizontal wavelengths determined from intrinsic frequencies from Stokes analysis (Fig. 4.16) for stationary waves (Eq. (3.15)) are shown in Figure 4.20. The determined horizontal wavelengths lie mainly below 500 km for the troposphere (Fig. 4.20a). A broader range of horizontal wavelengths is found for the stratosphere (Fig. 4.20b). The horizontal wavelengths needed to enable stationarity (Eq. (3.15)) are larger than 500 km for large part of the soundings in the stratosphere because the intrinsic frequencies from Stokes analysis are smaller and closer to f than in the troposphere. On the one hand, the results may reveal that the inertia-GWs in the stratosphere are not hydrostatic MWs. On the other hand, the waves found in the horizontal velocity perturbations of the soundings in the stratosphere may be hydrostatic MWs with horizontal wavelengths below 500 km as in the troposphere but are no longer stationary in the stratosphere for a large part of the soundings. The latter might be explained by the transience of the MW events at NZ due to the migrating weather systems (Sec. 4.2). The inertia-GW in Northern Europe presented in Dörnbrack et al. (2002) and Dörnbrack et al. (2017b) occurred during periods of long-lasting flows past the Scandinavian mountains and Svalbard. Therefore, this approach is not pursued in this thesis any further. It needs to be executed and evaluated in particular case studies.

Summary horizontal velocity analyses

The analyses of the horizontal velocity perturbations revealed variable GW activity in the troposphere and in the stratosphere among the IOPs and in the course of the IOPs. The overall mean values are 9.6 and 13.0 J kg^{-1} for *KE* and 4.3 and 6.9 J kg^{-1} for *PE* for troposphere and stratosphere, respectively. The intrinsic frequencies of the GWs are close to the inertial frequency f. Moreover, rotary spectra and Stokes analysis show dominant upward propagation of wave energy in the stratosphere. Vertical wavelengths of mainly 2 to 4 km and horizontal wavelengths of some hundreds kilometers are

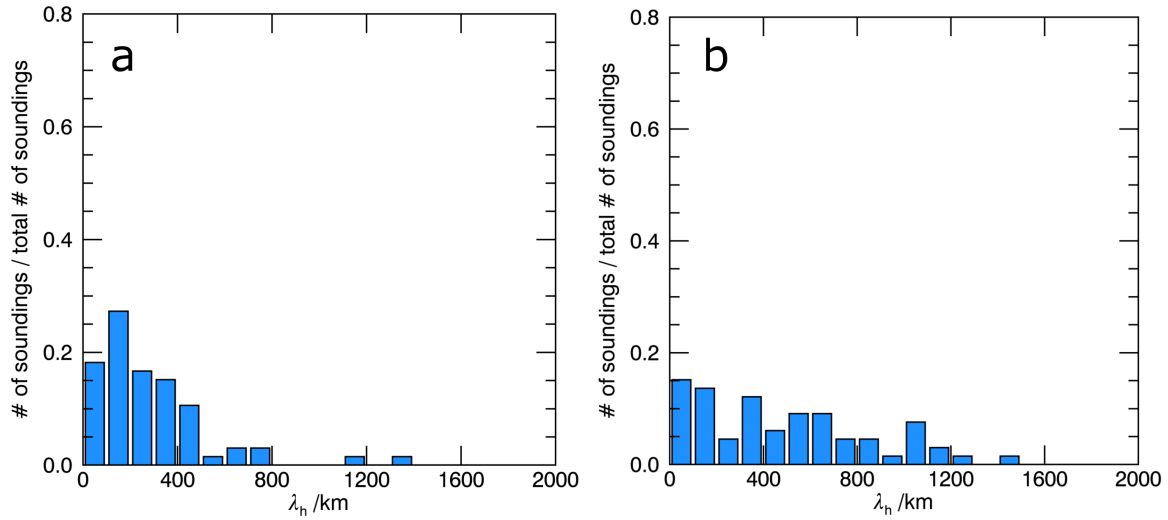

Figure 4.20: Distribution of the horizontal wavelength for troposphere (a) and stratosphere (b) for all Lauder soundings determined from intrinsic frequency from Stokes analysis when stationarity is assumend, i.e. hydrostatic MWs in a rotating regime (Eq. (3.15)).

the scales of the GWs in the stratosphere. The horizontal propagation direction of wave energy is dominated by the background winds and mainly to eastward directions, especially in the stratosphere. Mean ground-based group velocities are around 17 m s^{-1} horizontally and below 1 m s^{-1} vertically. The approach which assumes that the inertia-GWs are linked to the mountains being long stationary hydrostatic waves in a rotating regime leads to ambiguous results for the stratosphere. On the one hand, the results may reveal that the inertia-GWs in the stratosphere are not hydrostatic MWs. On the other hand, the results may reveal that the hydrostatic MWs are no longer stationary in the stratosphere for a large part of the soundings. In any case, the equation for stationarity (Eq. (3.15)) cannot be used to determine GW properties for a large part of the soundings. Therefore, this approach needs to be executed and evaluated in particular case studies.

4.3.2 Non-hydrostatic Mountain Waves

Gravity wave energy

Vertical kinetic GW energy per mass (Eq. (3.11)) determined from the vertical velocity perturbations is shown in Fig. 4.21. As for *KE* and *PE*, the overbar ($\overline{VE}$) indicating mean vertical values is omitted for simplicity and only *VE* is used. The mean *VE*

over all IOPs is 0.5 J kg^{-1} for the troposphere and 0.6 J kg^{-1} for the stratosphere. Those values are significantly smaller than those of horizontal kinetic GW energy (see Sec. 4.3.1). Largest values of *VE* were found for GB 21 in the troposphere and for IOP 16 followed by GB 21 in the stratosphere. IOP 16 was classified as TSW regime (Tab. 4.3) which is characterised by more southerly winds. The PFJ was located close to the SI. Weak to moderate GW activity was reported at flight level and strong activity in the stratosphere (AIRS from space) and in the MLT for IOP 16 (Fritts et al. 2016). GB 21 was classified as a period with some consecutive days of the W regime (Tab. 4.3) and strong MWs were observed by the ground-based lidar in lower and mid stratosphere (Fritts et al. 2016, Ehard et al. 2017). It's worth mentioning here again that some soundings were not used because the sondes were descending from time to time in the course of the flight (vertical velocity perturbations > 5 m s^{-1}). This happened especially during IOP 6. Nevertheless, the enhanced stratospheric vertical energy of the remaining sounding still indicates the enhanced MW activity for this IOP. IOP 6 was classified as SW regime (Tab. 4.3) and significant wave activity was reported at flight level and in the MLT (Fritts et al. 2016).

While *KE* and *PE* of IOP 15 are similar to those of IOP 3, 4 and 6 (Fig. 4.14), *VE* is almost zero for IOP 15. IOP 15 is characterised by weak SE winds at the surface and W winds above which created a critical level. Therefore, IOP 15 will be called a "non-mountain wave" case. This difference in the GW energies highlights again the sensitivity of the different variables to different parts of the GW spectrum. The difference between IOP 3, 4, 6 and 15 will be discussed later on in more detail to show that the vertical velocity perturbations determined from the balloon ascent rate are

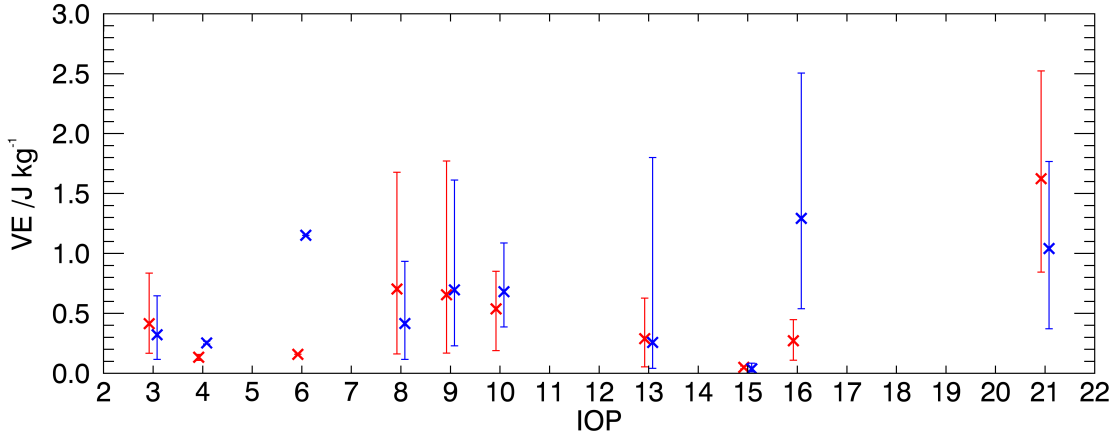

Figure 4.21: Vertical energy for Lauder soundings as mean values for IOPs (x) for troposphere (red) and stratosphere (blue). Bars show the minimum and maximum values during an IOP. Number of soundings analysed for each IOP can be found in Table 3.1.

indeed caused by MWs. This should further justify the interpretation of VE as proxy for MW activity and the assumption of stationarity in the horizontal projection method. The non-mountain wave case (IOP 15) and the three mountain wave cases of IOP 3, 4 and 6 are analysed by means of ECMWF model analysis, aircraft insitu measurements and the corresponding vertical velocity perturbations from soundings in Sec. 4.3.3.

Horizontal projection method

In the following, the horizontal wavelength is computed from the vertical velocity perturbation using the horizontal projection method (examples showing the vertical velocity perturbations projected to the new horizontal coordinate are given in Sec. 4.3.3, Fig. 4.26 and Fig. 4.27). Wave properties are then determined based on the horizontal wavelengths.

First of all, it should be mentioned here that the horizontal projection method does not reveal a result for all analysed soundings. The reasons for this are the cross mountain wind profile ($u_c(z)$, cf. Fig. 4.26) showing a zero crossing (i.e. critical level for MWs), unstable conditions in the upper troposphere (i.e. negative N^2) or the iterative determination of the horizontal wavelength adapting the projected horizontal coordinate does not converge to one value. In addition, results showing a wave which is evanescent over the whole altitude range (troposphere or stratosphere) were not included. Intrinsic frequency, vertical wavelength, and group velocity cannot be determined for those waves. This was mainly the case for soundings without a clear wave signal resulting in horizontal wavelengths smaller than 5 km.

Table 4.4 shows the number of soundings analysed for each IOP (same as in Tab. 3.1) and the number of soundings for which the horizontal projection method reveals waves that can propagate at least in a certain part of the analysed altitude range. Unstable conditions in the upper troposphere and a critical level in the stratosphere above 20 km altitude restricted the determination of wave properties for soundings of IOP 8 (HE and TNW regime). Wave properties only could be determined for one sounding out of six. The low level wind for IOP 13 was more northerly in the first part of the IOP which lead to a critical level in the stratosphere where westerly winds prevailed. In the course of the IOP the low level wind changed to a more westerly direction and the critical level was no longer present in the stratosphere. The revealed waves in the troposphere often had horizontal wavelengths smaller than 5 km which makes them evanescent in the whole troposphere. Those are the explanations why results where only obtained for 3 (6) soundings in the troposphere (stratosphere) out of 15 for IOP 13 (HE and TNW regime). No only the vertical velocity perturbations were almost zero for IOP 15 but also the wind direction changed from southeasterly at the low levels to westerly in the stratosphere which created a critical level.

Table 4.4: Number of soundings used in the analysis (top row) and those revealing wave properties with the horizontal projection method (bottom rows) for each IOP.

	IOP									
	3	4	6	8	9	10	13	15	16	21
used	9	3	1	6	10	12	15	3	4	3
hz. projection										
tropo	7	2	1	1	7	7	3	0	2	3
strato	9	3	1	1	8	10	6	0	3	2

Figure 4.22 shows the horizontal wavelength determined with the horizontal projection method for all IOPs as well as their distributions for troposphere and stratosphere. The mean horizontal wavelength is 19 km for the troposphere and 12 km for the stratosphere. The variability among the IOPs is larger for the troposphere than for the stratosphere (Fig. 4.22a). The determined horizontal wavelength are more equally distributed between 5 and 45 km (Fig. 4.22b) for the troposphere while the horizontal wavelengths are mainly between 5 and 20 km for the stratosphere (Fig. 4.22c). The larger variability and larger horizontal wavelengths in the troposphere may be explained by the method itself. The horizontal wind speed varied in the troposphere due to tropospheric weather systems and the influence of the tropospheric jets (Sec. 4.2.1) which causes a variation of the horizontal drift of the soundings. Hence, the largest horizontal wavelength that is captured by the sounding changes.

However, there also is a physical explanation for the change of the horizontal wavelength with the background wind. The Scorer parameter changes with the background wind and with it also the critical horizontal wavelength above which waves can propagate vertically (Sec. 2.1, cf. Fig. 4.5) changes. Therefore, it is also reasonable from a process point of view that the horizontal projection method reveals larger horizontal wavelength for IOP 10 and GB 21 in the troposphere. The wind speeds were significantly larger than 20 m s^{-1}, i.e. around 30 to 50 m s^{-1}, which made waves of horizontal wavelengths smaller than around 20 km to be evanescent in the whole troposphere. Nevertheless, the horizontal wavelengths is 10 to 15 km in the stratosphere even for those IOPs (Fig. 4.22a). Those shorter waves can propagate vertically in that altitude range because the wind speed and the critical horizontal wavelength are smaller in the stratosphere. But since they are evanescent in the troposphere, their occurrence in the stratosphere can be explained probably by leakage from the troposphere, i.e. they are not completely damped in the upper troposphere, totally reflected or fully trapped at the TIL (Sec. 2.1). Propagating MWs above the TIL in the stratosphere were also found along side the reflected and trapped waves in the idealized simulations (Sec. 4.1).

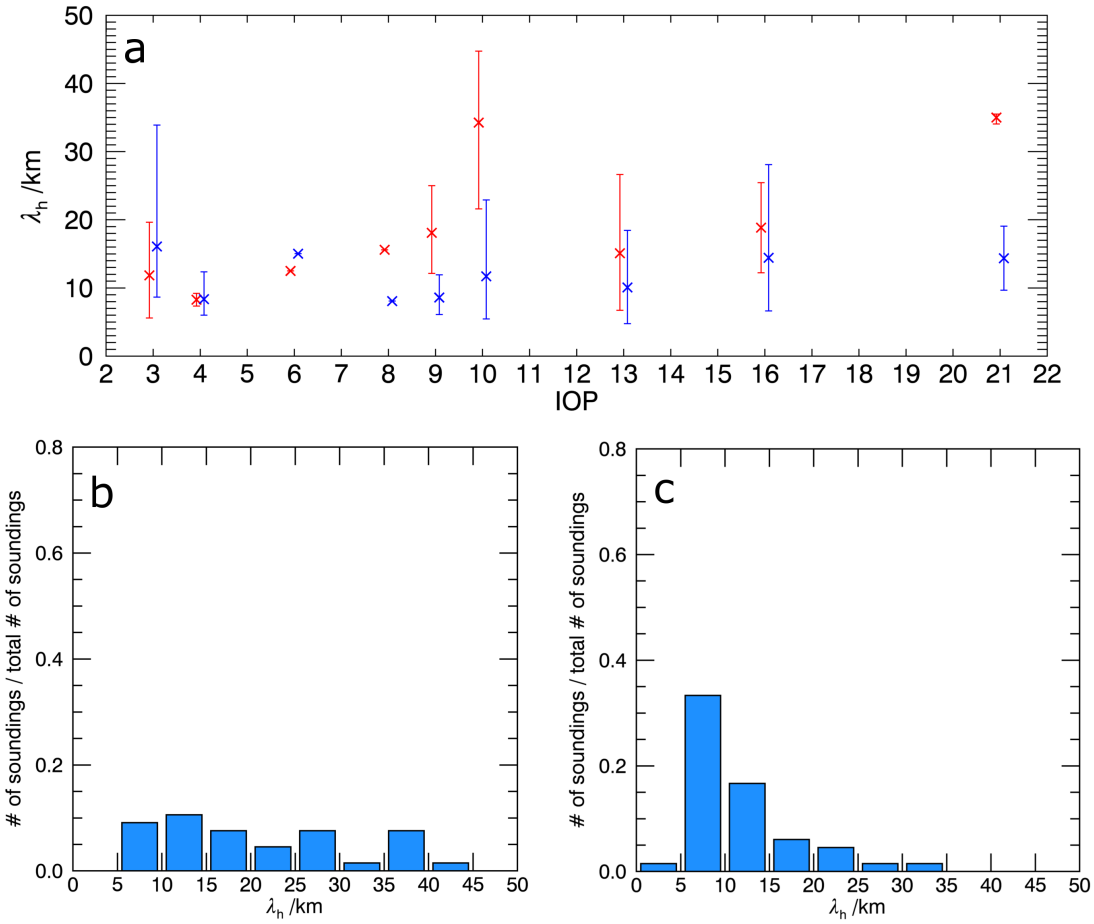

Figure 4.22: (a) Horizontal wavelength from horizontal projection method as mean values for IOPs (x) for troposphere (red) and stratosphere (blue). Bars show the minimum and maximum values during an IOP. Distribution of horizontal wavelength for troposphere (a) and stratosphere (b) for Lauder soundings. Relative numbers are with respect to the total number of soundings analysed and comparable to results of the previous section.

Intrinsic frequency

The altitude dependent intrinsic frequency of the waves can be determined from the horizontal wavelength if stationarity is assumed (Eq. (2.27)). The profiles of the intrinsic frequency of all soundings for which a horizontal wavelength was obtained with horizontal projection method is shown in Fig. 4.23. The mean intrinsic frequency is around $64f$ for troposphere and $120f$ for stratosphere which corresponds to periods of about 16 and 8 minutes, respectively. Hence, those waves are indeed medium to high frequency waves with intrinsic frequencies generally closer to N (typically 0.01 s^{-1} for

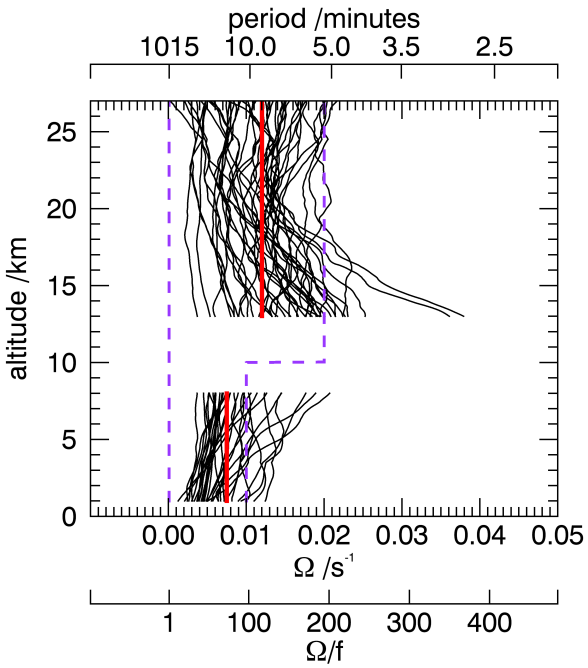

Figure 4.23: Intrinsic frequency as function of altitude determined from horizontal wavelength and background cross mountain wind speed for Lauder soundings. Red lines show the mean value in troposphere and stratosphere, respectively. Purple lines show inertial frequency (f) and typical mean Brunt-Väisälä frequencies for troposphere (0.01 s^{-1}) and stratosphere (0.02 s^{-1}).

troposphere and 0.02 s^{-1} for stratosphere) than to f. Mean values over altitude could be shifted to higher values not representative for the whole altitude range because the wind speed can be locally enhanced compared to the remaining altitude range, e.g., below or above the tropospheric jet. Since this is also true for the vertical wavelength (Eq. (2.28)) and for group velocities (Eqs. (2.25), (2.26)) median values instead of mean values over altitude are presented in the following.

Vertical wavelengths

Vertical wavelengths in the troposphere are found to be larger than those in the stratosphere (Fig. 4.24). This is mainly caused by smaller values of N in the troposphere. In addition, the variability is larger in the troposphere and vertical wavelengths are equally distributed between 3 and 27 km (Fig. 4.24a). Vertical wavelengths are mainly between 3 and 12 km in the stratosphere (Fig. 4.24b). The mean vertical wavelength of the soundings is 15 km for the troposphere and 7 km for the stratosphere. IOP 10 and

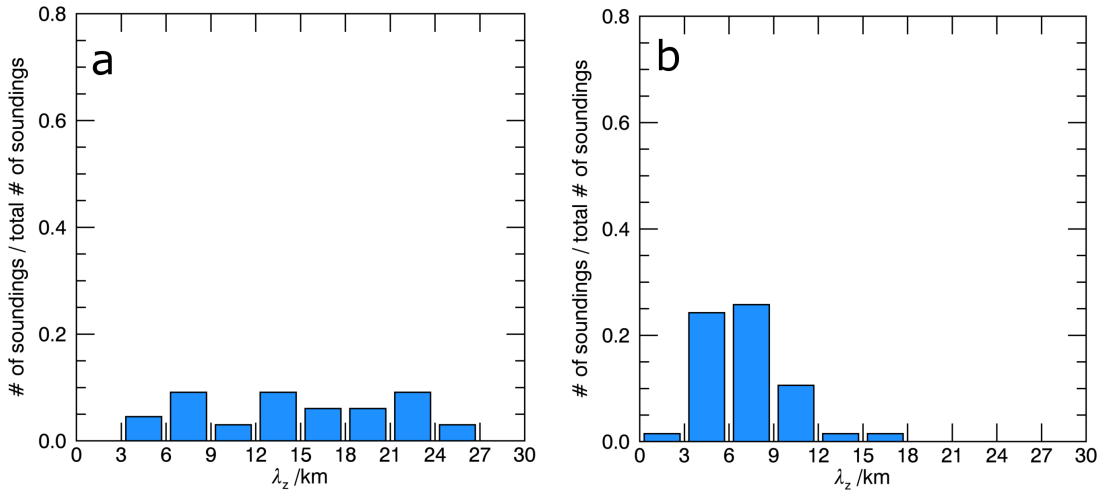

Figure 4.24: Distribution of the vertical wavelength (median of altitude dependent values) determined from horizontal wavelength for troposphere (a) and stratosphere (b) for Lauder soundings.

GB 21 show the largest vertical wavelength in the troposphere due to the prevailing largest wind speed (for more details see Appendix A.2).

Group velocity

Figure 4.25a, b shows the ground-based horizontal group velocity based on horizontal and vertical wavenumbers (Eq. (2.25)). The values are more similar (Fig. 4.25a, b) for troposphere and stratosphere than the values of the vertical wavelength because ground-based horizontal group velocity not only depends directly on background wind and stability (Eq. (2.25)) but also indirectly via wave numbers (Eqs. (2.28) and (2.29)). Mean values of the ground-based horizontal group velocity are about 8 and 6 m s^{-1} for troposphere and stratosphere, respectively. Overall, the ground-based horizontal group velocities are mainly below 15 m s^{-1} (Fig. 4.25a, b). Similar values are found for the vertical group velocity which is shown in Figure 4.25c, d. Mean values over the soundings are 9 m s^{-1} for troposphere and 7 m s^{-1} for stratosphere.

Summary ascent rate analyses

In summary, analyses of the vertical velocity perturbations based on the balloon ascent rate revealed *VE* being around 0.5 J kg^{-1} and significantly smaller then *KE* and *PE*. The horizontal projection method revealed properties of non-hydrostatic MWs for 50 % of the soundings in the troposphere and for 65 % of the soundings in the stratosphere.

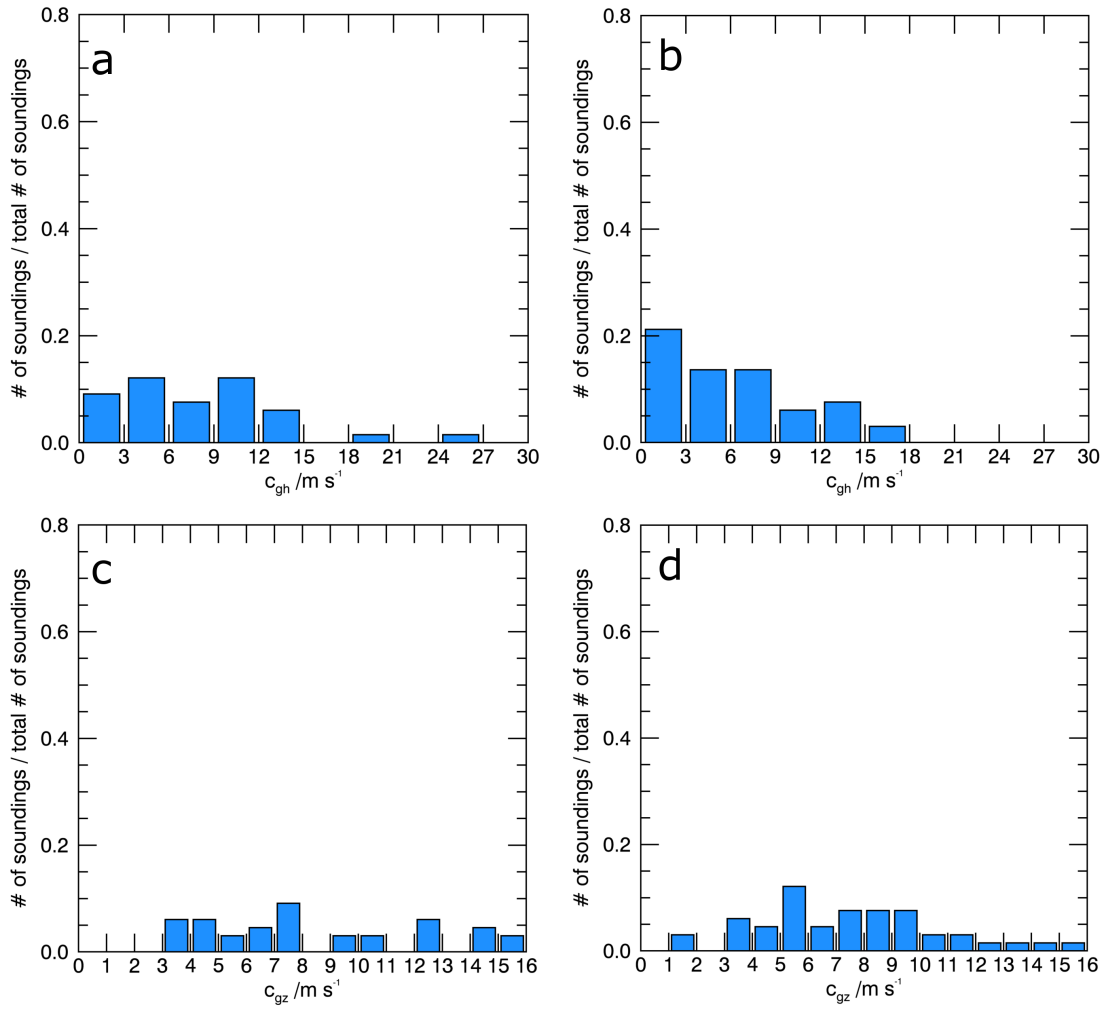

Figure 4.25: Distribution of ground-based horizontal (a, b) and vertical (c,d) group velocity for troposphere (top) and stratosphere (bottom) for Lauder soundings.

They have horizontal and vertical wavelength of tens of kilometers (< 50 km) and intrinsic frequencies closer to N than to f. The MWs were often evanescent in the upper troposphere. Nevertheless, they were also found in the stratosphere. The non-hydrostatic MWs propagate vertically as fast as horizontally with ground-based horizontal and vertical group velocities of similar magnitude (up to 15 m s^{-1}).

4.3.3 Mountain Wave Cases vs. Non-mountain Wave Case

In this section, the IOPs 3, 4, 6 and 15 are analysed and the results of the horizontal projection method are shown in detail. These IOPs show a similar amount of *KE* but not of *VE* (almost zero for IOP 15). It is shown that the vertical velocity perturbations

determined from the balloon ascent rate are indeed caused by MWs by combining findings from sounding data with ECMWF IFS analyses and aircraft insitu data. This should further justify the interpretation of *VE* as proxy for MW activity and the assumption of stationarity in the horizontal projection method.

Figure 4.26 shows the vertical velocity perturbations as a function of time for one soundings of each IOP 3, 4, 6 and 15, respectively. The vanishing small vertical velocity perturbations of the sounding of IOP 15 compared to the soundings of the other IOPs as already revealed by *VE* (Fig. 4.21) are clearly visible at all altitudes. The low level cross mountain wind (1-3 km altitude) was northwesterly for the soundings of IOP 3 and IOP 4, southwesterly for the sounding of IOP 6, and southeasterly for the sounding of IOP 15 (cf. Tab. 4.3). The mean wind speed of u_c between 1-3 km altitude was 11, 13 and 17 m s^{-1} for the soundings of IOP 3, 4 and 6, respectively (Fig. 4.26e, f, g). The wind speed was only 4 m s^{-1} for the sounding of IOP 15 (Fig. 4.26h), i.e. fairly weak for triggering MWs. Moreover, the wind direction changed from SE in the lower troposphere to W in the lower stratosphere. The cross mountain wind u_c going into the horizontal projection method encounters a zero crossing which is a critical level for stationary MWs (i.e. $\Omega = 0$). No wave properties can be derived with the horizontal projection method for the sounding of IOP 15. The method revealed horizontal wavelengths of 9.8 (10.1), 9.2 (6.7) and 12.5 (15.0) km for troposphere (stratosphere) for IOP 3, 4 and 6, respectively (Fig. 4.27). These tropospheric horizontal wavelengths were below the corresponding critical horizontal wavelength (λ_c) in the upper troposphere in all cases (Fig. 4.28). The waves were evanescent in the upper troposphere. The critical wavelengths were smaller than the determined horizontal wavelengths in the stratosphere. The waves can propagate vertically in the stratosphere. The vertical wavelength (Eq. (2.28)) increases towards infinity in the upper troposphere while the vertical wavelengths vary between 5 and 15 km in the stratosphere.

One can not expect to find the non-hydrostatic MWs identified in the radiosonde data in the ECMWF IFS analyses because the ECMWF IFS is a hydrostatic model. Moreover, the horizontal scales of the non-hydrostatic MWs are quite short being tens of kilometers (horizontal grid spacing of the ECMWF IFS Cy40r1 used here is around 16 km). The Southern Alps trigger not only non-hydrostatic but also hydrostatic MWs. The latter are resolved in the ECMWF IFS. First of all, it is checked whether hydrostatic MWs in the ECMWF IFS analyses occur together with the non-hydrostatic MWs in the soundings for IOP 3, 4 and 6. Secondly, the vertical wavelengths predicted by linear theory for the hydrostatic MWs based on sounding data are compared to the vertical wavelengths found in the ECMWF IFS analyses. It follows from Eq (2.28) that $m^2 \approx \ell^2$ ($\lambda_z \approx \lambda_{crit}$) because $m^2 >> k_h^2$, i.e. horizontal wavelength is clearly larger than the vertical wavelength, for hydrostatic waves. These comparisons should show the consistency between MW activity in the radiosonde measurements and in the ECMWF IFS analyses as well as between wave characteristics predicted linear theory, when the atmospheric state directly from soundings, and wave characteristics found in

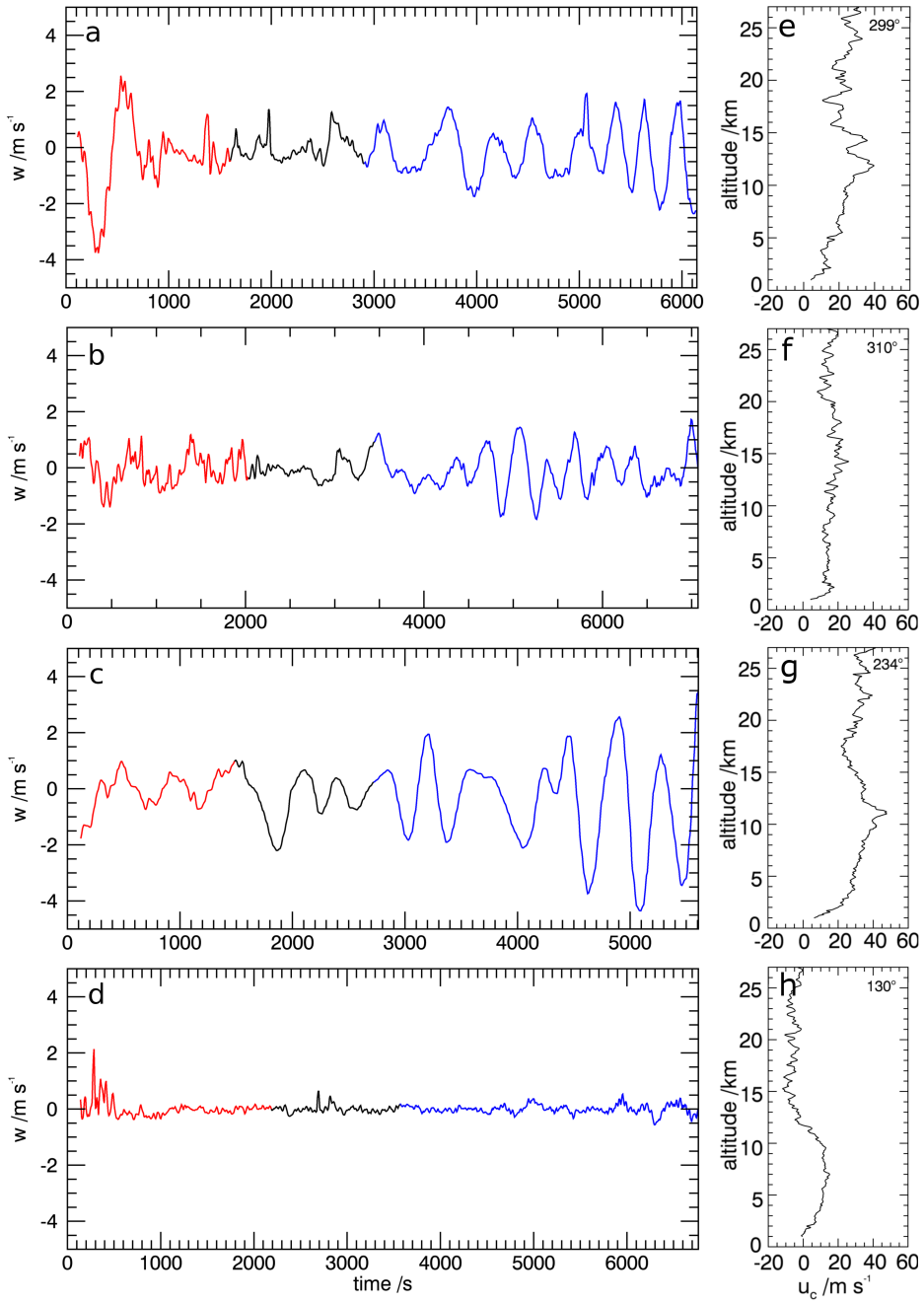

Figure 4.26: Vertical velocity perturbations of the soundings of (a) IOP 3 on 14 June 05:30 UTC, (b) IOP 4 on 16 June 14:36 UTC, (c) IOP 6 on 19 June 14:31 UTC and (d) IOP 15 on 17 June 00:00 UTC as a function of balloon flight time. Red and blue mark troposphere and stratosphere, respectively. Cross mountain wind speed in the given direction (degrees from N) for the soundings of (e) IOP 3, (f) IOP 4, (g) IOP 6 and (h) IOP 15.

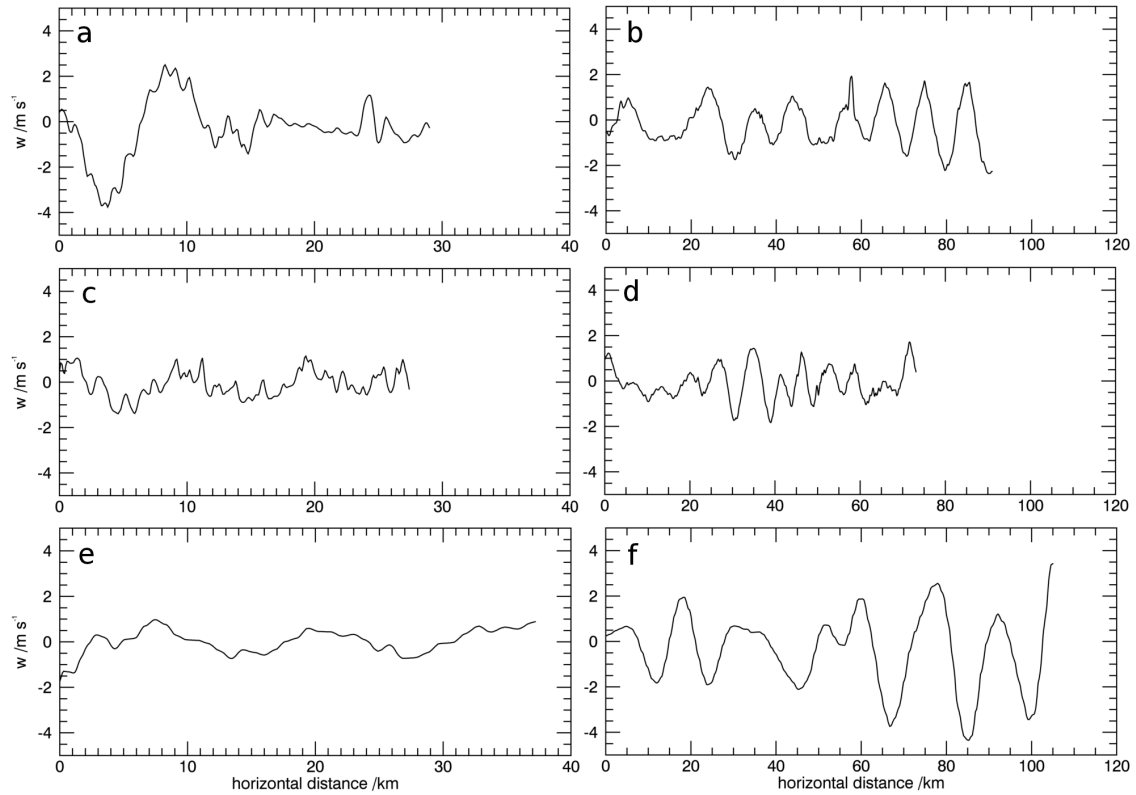

Figure 4.27: Vertical velocity perturbations of the soundings of IOP 3 (a,b), IOP 4 (b,c) and IOP 6 (c,d) as a function of the projected distance for troposphere (left) and stratosphere (right). The projected distance is based on the horizontal wavelengths of 9.8 km (a), 10.1 km (b), 9.2 km (c), 6.7 km (d), 12.5 km (e) and 15.0 km (f).

ECMWF IFS analyses.

A wave pattern is found in the vertical velocity at 15 km altitude over the southern part of the SI for IOP 3 (Fig. 4.29a). The W-E crosssection at 45° S (Fig. 4.29b) reveals that the signal comes from a hydrostatic MW with clearly enhanced vertical velocity perturbations compared to the upstream and downstream region of the SI. The absolute amplitudes are an order of magnitude smaller than in the measurements (Fig. 4.26). Nevertheless, the enhanced vertical velocity perturbations in the sounding come along with an enhanced vertical velocity perturbation in the ECMWF IFS for this case. The horizontal wavelength of the hydrostatic MWs is approximately equal to the width of the southern part of the SI in the troposphere and lower stratosphere (Fig. 4.29a, b) being approximately 230 km. The horizontal wavelength is approximately 150 km above 15 km altitude (Fig. 4.29b). The vertical wavelength is around 6-7 km in the stratosphere (Fig. 4.29b). This is in agreement with the estimate from the Scorer parameter (Eq. (2.29)) of the sounding varying between 6.1 and 8.4 km (Fig. 4.28a).

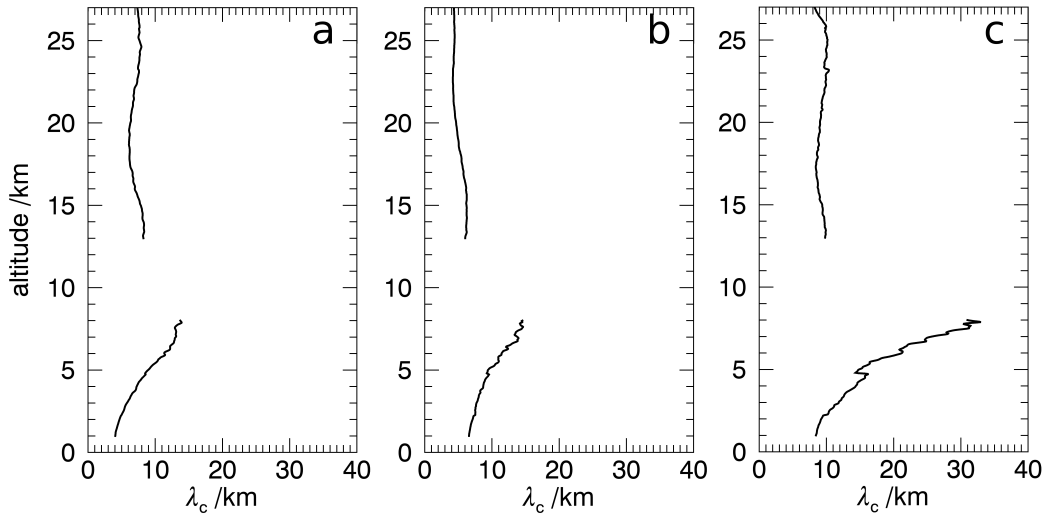

Figure 4.28: Critical horizontal wavelength from Scorer parameter for soundings of IOP 3 (a), IOP 4 (b) and IOP 6 (c).

For IOP 4 the wave pattern in the vertical velocity at 15 km altitude covers the central and northern part of the SI (Fig. 4.29c). The wave fronts are aligned in a SW-NE direction. Figure 4.29d shows a N-S crosssection at 171° E. As for IOP 3, the vertical velocity perturbations are significantly enhanced in the vicinity of the SI. The horizontal wavelength is estimated to be about 220 km. The vertical wavelength is approximately 4-5 km in the stratosphere but the wave pattern is only found up to 20 km altitude (Fig. 4.29d). The predicted vertical wavelength based on the Scorer parameter (Eq. (2.29)) of the sounding varies between 4.2 and 6.3 km (Fig. 4.28b) which matches the results from the ECMWF IFS.

The wave fronts in the vertical velocity over NZ are oriented in a NW-SE direction for IOP 6 and show at least waves of two different scales over the SI (Fig. 4.29e). Smaller scale structures of horizontal wavelengths of around 120 km are visible in the W-E crosssection at 45° S in the troposphere as well as in the stratosphere (Fig. 4.29f, gray dotted). It looks like these 120 km waves superimpose with 230 km (gray solid) waves leading to a less monochromatic pattern in the stratosphere compared to IOP 3 (Fig. 4.29b). The vertical wavelength is around 9 km for the 120 km waves and around 6.5 km for the 230 km wave (Fig. 4.29g). The predicted vertical wavelength based on the Scorer parameter (Eq. (2.29)) of the sounding varies between 8.2 and 10.4 km for this case (Fig. 4.28c) which agrees with the 120 km wave in the ECMWF IFS.

For IOP 15 no enhanced vertical velocity perturbations are found at 15 km altitude in the vicinity of the SI (Fig. 4.30a). In the N-S crosssection at 170° E (Fig. 4.30b) some enhanced perturbations are found, if at all, in the lower most part of the troposphere. They are clearly weaker compared to the MWs of IOP 3, 4 and 6. Something similar

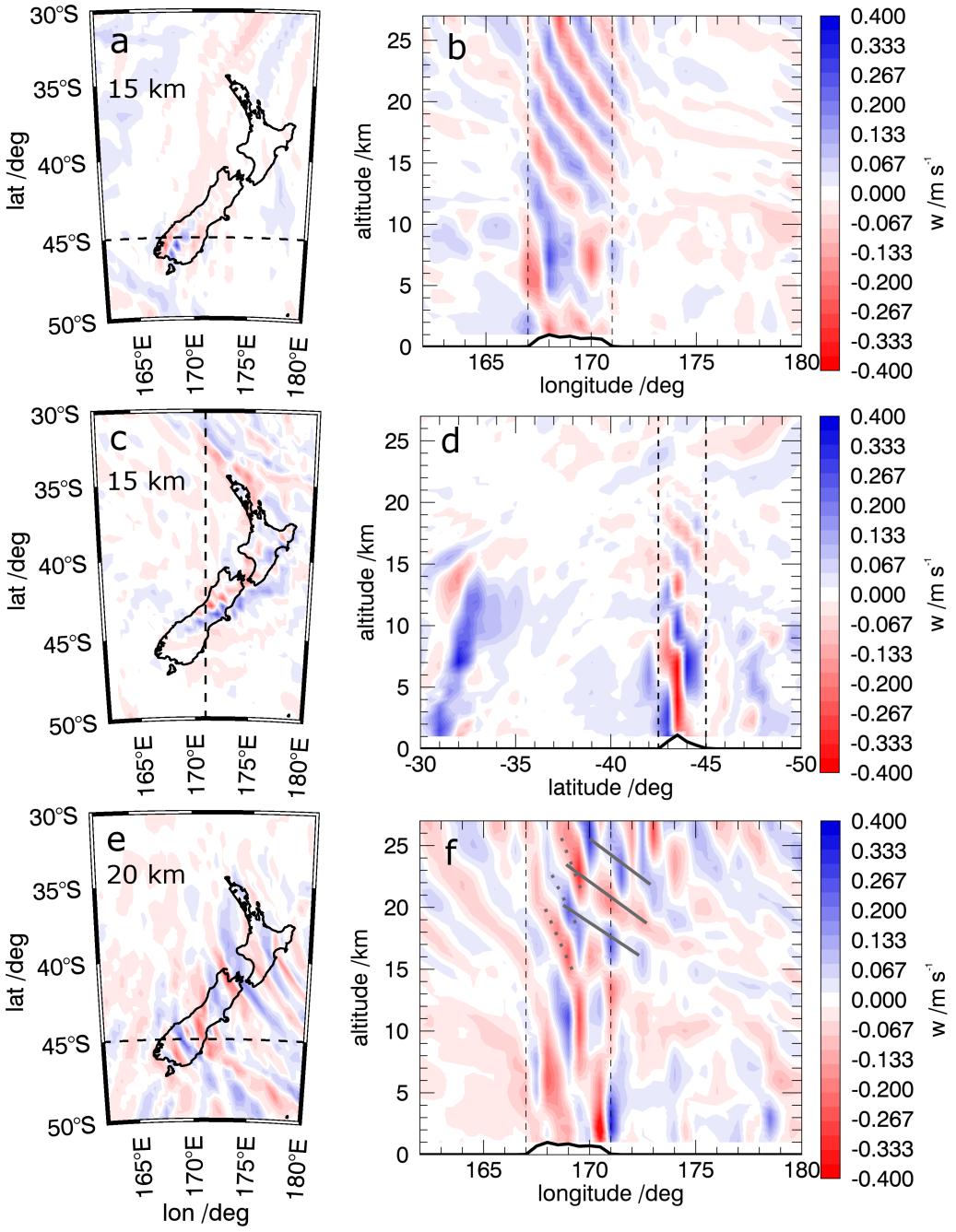

Figure 4.29: Vertical velocity of ECMWF for IOP 3 on 14 June 06 UTC (a,b), IOP 4 on 16 June 12 UTC (c,d) and IOP 6 on 19 June 12 UTC (e,f) at 15 km (a, c) and 20 km (e) altitude. Dashed lines in the left plots (a, c, e) mark the location of the crosssections (b, d, f). Solid and dashed lines in the right plots show ECMWF topography and the extent of the SI, respectively. Gray solid and dotted lines in (f) mark two scales of waves.

is found for two legs of vertical velocity insitu measurements of the NCAR/NSF GV and the DLR Falcon during IOP 4 and IOP 15 (Fig. 4.31). These two legs were chosen because they were both along the same flight track (Fig. 4.31b, d) and in the lower stratosphere which allows a direct comparison. While the vertical velocity amplitudes reach up to 2 m s^{-1} for the leg of IOP 4 (Fig. 4.31a) indicating MW activity at smaller scales (Smith and Kruse 2017), the amplitudes hardly reach 0.5 m s^{-1} for the leg of IOP 15 (Fig. 4.31c). Mean vertical kinetic energies along the legs are 0.20 J kg^{-1} and 0.01 J kg^{-1}, respectively.

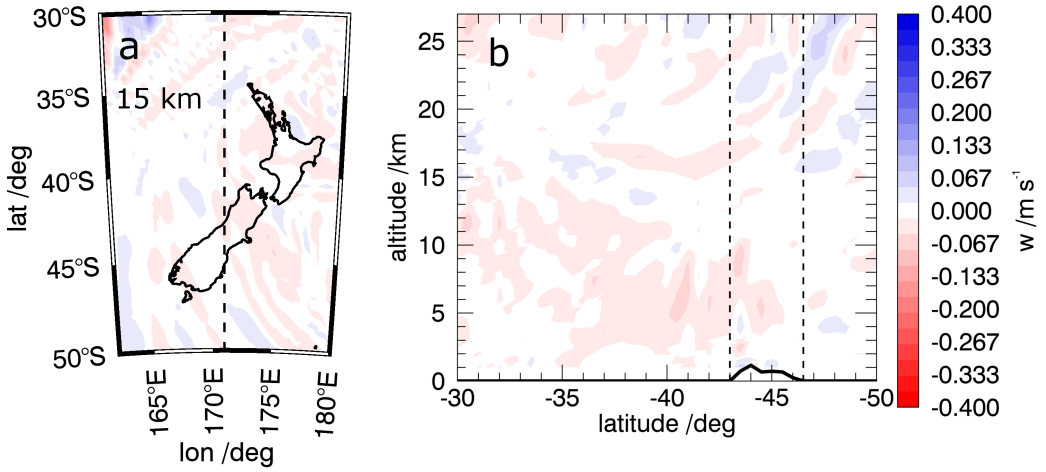

Figure 4.30: Vertical velocity of ECMWF for IOP 15 on 17 June 00 UTC at 15 km altitude (a). Dashed lines in the left plot (a) mark the location of the crosssection (b). Solid and dashed lines in the right plot show ECMWF topography and the extent of the SI, respectively.

Summary mountain wave cases vs. non-mountain wave case

There was not only a weaker forcing during IOP 15 but MWs would also have encountered a critical level due to the changing wind direction with altitude. This is clearly reflected by the MW activity seen in ECMWF IFS data and aircraft data which matches the almost zero *VE*, i.e. MW activity, in the soundings of IOP 15 (Fig. 4.21). In contrast, wave activity in the vertical velocity perturbations for IOP 3, 4 and 6 occurred together with hydrostatic MWs in ECMWF IFS data and enhanced vertical velocity fluctuations indicating MW activity at smaller scales in aircraft data. This finding confirms that the vertical velocity perturbations, which are determined from the balloon ascent rate, are indeed caused by MWs. It further justifies the interpretation of *VE* as proxy for MW activity and the assumption of stationarity in the horizontal projection method. *VE* of the soundings which were analysed for IOP 3, 4 and 6 was

dominated by non-hydrostatic MWs with horizontal wavelengths of 6.5 to 15 km as revealed by the horizontal projection method.

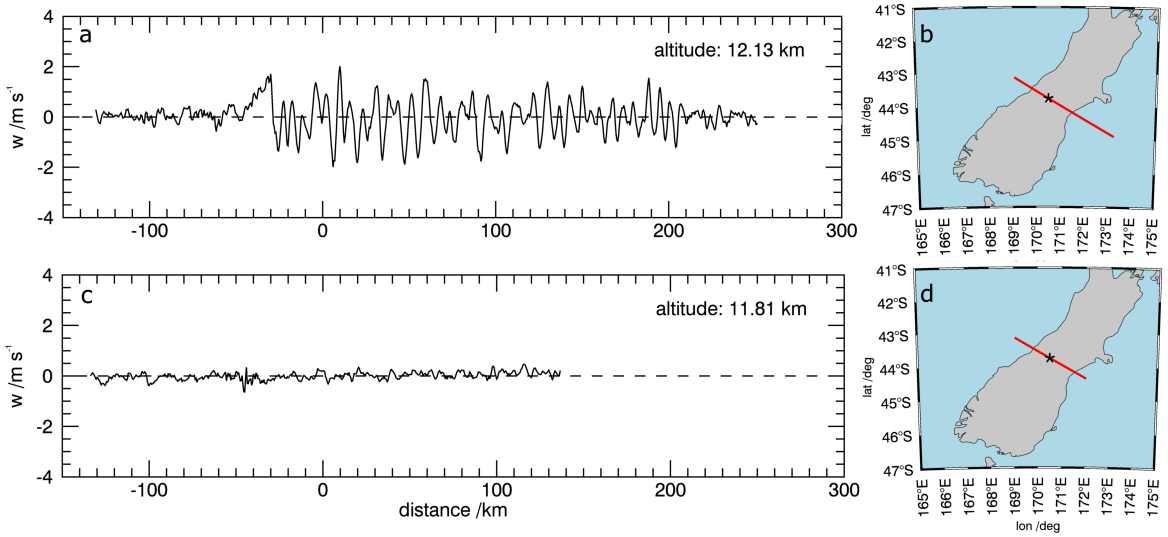

Figure 4.31: Vertical velocity of (a) GV measurements during IOP 4 (leg start time 16 Jun 11:49 UTC) and (c) Falcon measurements during IOP 15 (leg start time 16 Jul 23:19 UTC) in the lower stratosphere. Location of the flight legs are shown on the right (b, d). There the star marks the reference point of the legs centered on the SI, i.e. distance equal 0 km in (a, c).

5 Discussion

5.1 Gravity Wave Sources

GW activity and characteristics of low- to high-frequency GWs in the troposphere and stratosphere determined from Lauder radiosoundings were presented in section 4.3. The sources of these GWs are evaluated based on the determined GW characteristics with the focus being on the assignment to orographic sources (see first hypothesis in Sec. 1.3). As reviewed in the introduction of Spiga et al. (2008), the four known major sources for inertia-GWs in the atmosphere are topography, upper tropospheric jet streams, lower tropospheric frontal systems, and deep convection. Large amplitude MWs are suggested to cause inertia-GWs by adjustment of the large-scale flow due to the high amplitude and eventually breaking of the main MW. Inertia-GW emission by the jet streams is also associated with spontaneous adjustment (Plougonven and Zhang 2014). Measurements as well as numerical studies confirmed the emission of inertia-GWs during the frontogenesis process. Different mechanisms were identified for convection which emit GWs of varying frequency and structure, i.e. a bulk release of the latent heat, the "obstacle effect", and the mechanical oscillatory motions. The last mechanism seems to produce only high-frequency waves (Spiga et al. 2008).

The main focus of almost all published papers of the DEEPWAVE campaign is on MWs. Gravity waves from non-orographic sources as jet, frontal systems, and convection are explicitly listed in the DEEPWAVE overview paper of Fritts et al. (2016) only for IOP 6, 8 and 9, i.e. in connection with research flights of the GV over the Tasman Sea towards Australia and southward over the Southern Ocean. In addition, one initial conclusion given in Fritts et al. (2016) says that "smaller-scale GWs arise preferentially from orography, deep convection and secondary GW generation in the stratosphere". In the course of the presentation of new filtering and GW diagnostics for mesoscale data fields, Kruse and Smith (2015) not only discussed two orographic but also two non-orographic GW events. One took place in the Southern Ocean south west of NZ on 11 July and was classified as a jet-generated GW event with significant vertical energy fluxes (> 1 W m^{-2}) found above 15 km altitude and moving towards NE direction. The other was an event in connection with a frontal system and convection (resolved, no convection parametrization (Kruse et al. 2016)) over the Tasman Sea west of NZ on 10 July. GWs created by the "obstacle effect" at the top of the convection and extending into the

stratosphere were found during this event. Overall, Kruse and Smith (2015) found that the orographic and non-orographic events have four attributes in common, namely positive vertical energy fluxes, upwind-orientated fluid-relative horizontal energy fluxes, wave-/mean-shear interaction, and nonlinear dissipation when dissipation occurred. Smith et al. (2016) concluded that MWs dominated during DEEPWAVE because the analyses of momentum and energy fluxes from GV measurements in the low stratosphere over the ocean were significantly smaller than over NZ and hardly above detection level. Although Smith et al. (2016) did not exclude further identification of non-orographic waves, they point out limited magnitude and frequency of occurrence of those waves in the low stratosphere at around 12 km. Especially, the two non-orographic events analyzed by Kruse and Smith (2015) confirm the occurrence of non-orographic GWs in the stratosphere around NZ. Both non-orographic wave events occurred during IOP 13. The north eastward propagation of the jet generated wave package as well as the eastward movement of the convective systems towards NZ suggest the possible occurrence of non-orographic GWs in the stratosphere over NZ in the course of IOP 13. Therefore, radiosonde data covering altitudes up to 27 km may contain GWs of sources other than orographic. GWs of different sources can of course occur simultaneously (Spiga et al. 2008).

So far, the results presented in section 4, revealed variable forcing and propagation conditions for MWs among the IOPs of DEEPWAVE. The overall mean values from radiosonde observations are 9.6 and 13.0 J kg^{-1} for *KE* and 4.3 and 6.9 J kg^{-1} for *PE* for troposphere and stratosphere, respectively. This is a clear enhancement of stratospheric wave activity compared to previous studies at latitudes $> 50°$ in the Southern Hemisphere where largest mean values were given for the South Pole and for Maquarie Island (55°S, 159°S) (Table 2 in Moffat-Griffin and Colwell (2017)). Three-year mean values of *KE* at the South Pole are largest from May to November and reach values of around 9 J kg^{-1} (Pfenninger et al. 1999). The winter mean value over two years for Maquarie Island is around 4.5 J kg^{-1} (Vincent et al. 1997). Both, mean tropospheric and stratospheric *KE* are also enhanced compared to monthly mean values found for soundings in the United States which are around 6 J kg^{-1} for troposphere and around 9 J kg^{-1} for stratosphere (Geller and Gong 2010).

Analyses of the horizontal velocity perturbations from soundings showed that they are dominated by inertia-GWs characterized by low intrinsic frequencies. Differences were found between the intrinsic frequencies determined from Stokes analysis and the intrinsic frequencies determined from *KE* and *PE* (see Appendix A.1) which may be explained by the differences in the averaging procedure (Geller and Gong 2010). Curiously, the differences between the two methods are more pronounced for the tropospheric values. The determined horizontal wavelengths are hundreds of kilometers. However, a high variability was found depending on the soundings included, the way of calculation, and the intrinsic frequency used. This highlights the uncertainty of the determination of the horizontal wavelength of inertia-GWs from radiosoundings with

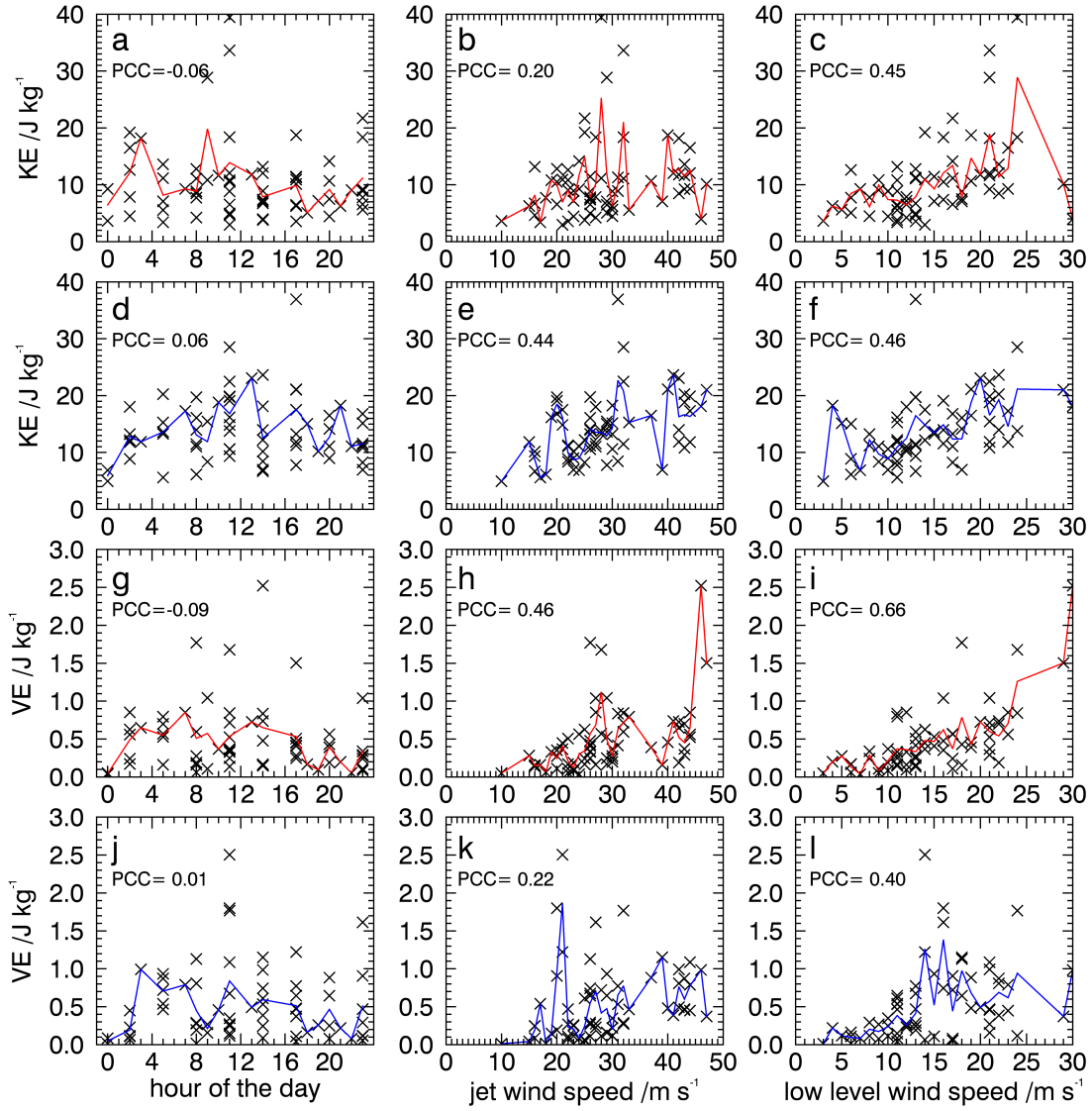

Figure 5.1: Horizontal kinetic energies (a-f) and vertical kinetic energies (g-l) of all Lauder soundings analyzed in dependence of hour of the day (a, d, g, j), of jet wind speed (b, e, h, k) and of low level wind speed (c, f, j, l) for troposphere (a-c, g-i) and stratosphere (d-f, j-l). Solid lines connect mean values for each hour or each m s^{-1}. PCC is the according Pearson correlation coefficient.

these methods. The finding is in agreement with Zhang et al. (2004) who reported important uncertainties when deriving GW properties from radiosonde data. They found that estimates of vertical wavelength and intrinsic phase speed for a mostly monochromatic inertia-GW packet tend to be more accurate than that of intrinsic frequency and horizontal wavelength.

No dominant vertical propagation direction was revealed by rotary spectra for the inertia-GWs in the troposphere but dominant upward energy propagation was found in the stratosphere. Similar results were revealed by the partitioning in upward and downward propagating soundings by Stokes analysis. Upward propagation was found for nearly all soundings (97 %) in the stratosphere but only for 56 % of the soundings in the troposphere. However, this does not necessarily mean that there was no dominant vertical propagation direction in the troposphere. The methods probably just do not allow to identify the dominant vertical energy propagation direction in the troposphere (in case of linearly polarized waves, Sec. 3.2.4) or there are indeed upward and downward propagating waves present either due to reflection (Sec. 4.1) or generation at tropopause level. Dominant upward propagation in the stratosphere suggests the source of the inertia-GWs to be in the troposphere or in the vicinity of the tropopause.

In contrast, studies at higher latitudes in the Southern Hemisphere tend to find a significant amount of downward propagating waves in the stratosphere during wintertime (Murphy et al. 2014, Moffat-Griffin and Colwell 2017, Moffat-Griffin et al. 2011, Yoshiki et al. 2004). The downward propagating waves in these studies are explained by wave generation in the stratosphere due to imbalanced flow associated with the polar vortex (Murphy et al. 2014). The magnitude of stratospheric imbalance at the longitude of NZ (175°E) is maximized south of NZ at 75°S and 55°S (Fig. 8a in Murphy et al. (2014)) which indicates the absence of a dominant source for downward propagating GW in the stratosphere over the SI of NZ.

The ground-based vertical phase speeds of the inertia-GWs have a mean absolute value of 1.25 m s^{-1} in the troposphere and 0.15 m s^{-1} in the stratosphere. A ground-based instrument, e.g., lidar, would measure an altitude change of the maxima and minima in the vertical profiles of 5.4 km in 10 hours, i.e. 1 night, in the stratosphere. Ground-based horizontal and vertical phase speeds show different signs compared to the intrinsic phase speeds for 76 % and 68 % of the soundings for troposphere and stratosphere, respectively. The change of the sign between intrinsic and ground-based phase speed means that an observer fixed in space, e.g., a ground-based lidar, would observe upward phase propagation even if the intrinsic phase propagation is downward and energy propagation is upward (Dörnbrack et al. 2017a). Doppler shifted ground-based upward phase propagation could be misleadingly interpreted as downward energy propagation.

Horizontal wave energy propagation is dominated by the background wind and is towards easterly directions, especially in the stratosphere. This suggests that the source of the waves is located to the west of Lauder. Mean ground-based group velocities are around 17 m s^{-1} horizontally and below 1 m s^{-1} vertically. While the vertical group velocities are similar, the ground-based horizontal group velocities are smaller over NZ compared to the findings at higher latitudes (Fig. 4d in Murphy et al. (2014)). This is likely because of the weaker stratospheric winds over NZ compared to higher latitudes

but could partly also be caused by different intrinsic propagation characteristics, i.e. larger intrinsic phase speeds against the background wind, due to a source different from an imbalanced flow.

Vertical velocity perturbations determined from the ascent rate of the soundings were successfully analyzed for non-hydrostatic MWs. They have horizontal and vertical scales of tens of km and downstream energy propagation. Although often evanescent in the upper troposphere, these non-hydrostatic MWs were also found in the lower and mid stratosphere which suggests their leakage from the troposphere across the tropopause into the stratosphere. Since ground-based horizontal group velocities and vertical group velocities are similar in amplitude, those waves propagate vertically as much as horizontally. This is a characteristic of non-hydrostatic MWs. It is in contrast to hydrostatic MWs not affected by rotation which propagate only vertically above the mountain. It is different to inertia-GWs whose energy propagate faster horizontally than vertically. The classification of those medium to high frequency waves contained in the vertical velocity perturbations as MWs was further strengthened by comparing MW cases with one non-MW case. The comparison showed their occurrence together with hydrostatic MWs in ECMWF and orographic wave activity in aircraft measurements.

However, even this finding could be ambiguous when convection as possible source for high-frequency waves (Spiga et al. 2008) and its occurrence in the vicinity of NZ (Kruse et al. 2016) is taken into account. Before testing a connection between stratospheric inertia-GWs and non-hydrostatic MW activity from soundings, convection must be excluded as dominant source for the vertical velocity perturbations. Figure 5.1a, d, g, j shows the altitude averaged *KE* and *VE* of all analyzed soundings for troposphere and stratosphere as a function of the hour of the day. Neither *KE* nor *VE* shows a clear dependence on the hour of the day as one would expect for convectively induced GWs on a typical day with convection starting at noon and covering the afternoon and evening (e.g. Lane et al. 2003). However, convection around NZ is not restricted to heating by the sun in noon and afternoon hours in wintertime but often takes place when cold air from the south moves northward over the warm Tasman Sea. Figure 5.2 and Figure 5.3 show infrared satellite images in combination with lightning information for all IOPs. The occurrence of convection in the vicinity of the SI of NZ based on the cloud and lightning information in those figures can be certainly excluded only for IOP 6 (Fig. 5.2c) and 15 (Fig. 5.3c) and likely excluded for IOP 3 (Fig. 5.2a) and IOP 16 (Fig. 5.3d). Convective activity with significant amount of lightning directly over the SI occurred during IOP 9 (Fig. 5.2e, f) and GB 21 (Fig. 5.3e, f). Nevertheless, larger amounts of *VE* compared to IOP 15 ("non-mountain wave" case, Sec. 4.3.3) were not only observed for IOP 9 and GB 21 but also for IOPs 6, 3 and 16 (Fig. 4.21). This finding eliminates convection as dominant source of the observed medium to high-frequency GWs. The contribution of convection to the observed inertia-GW activity (bulk release of latent heat, "obstacle effect") remains unclear. The zonal wind perturbations do not depend on the daily cycle of convection even for distinct

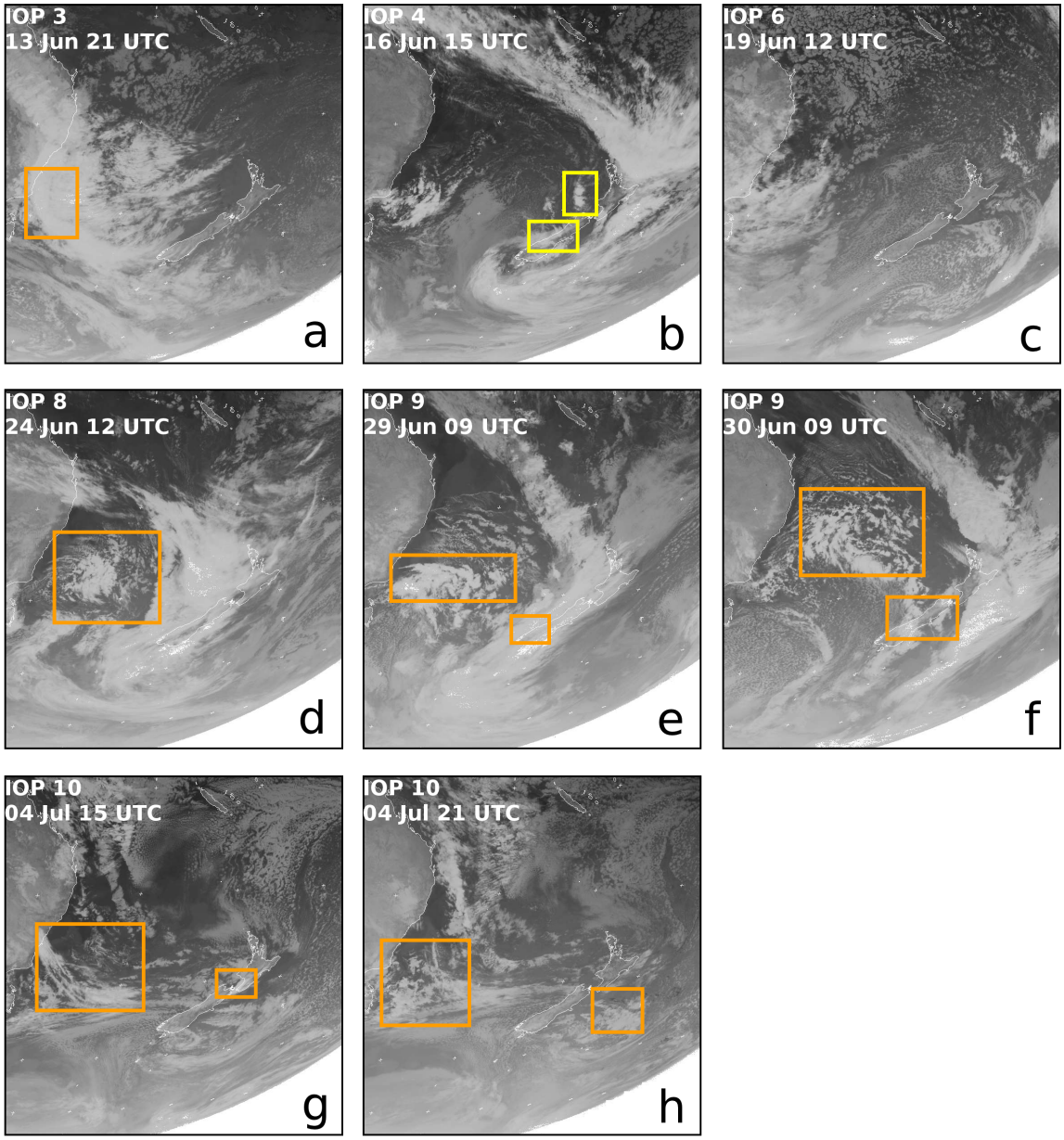

Figure 5.2: Satellite images of MTSAT (channel 2, mid-infrared) provided by NERC Satellite Receiving Station, Dundee University, Scotland (www.sat.dundee.ac.uk) for IOP 3 (a), 4 (b), 6 (c), 8 (d), 9 (e,f) and 10 (g,h). Boxes mark areas of weak ($\approx<$ 10 strokes, yellow) and moderate ($\approx<$ 1000 strokes, orange) lightning activity during the IOPs. Lightning information was looked up at LightningMaps.org which uses Lightning data by Blitzortung.org and contributors. Landmass is surrounded by white contours.

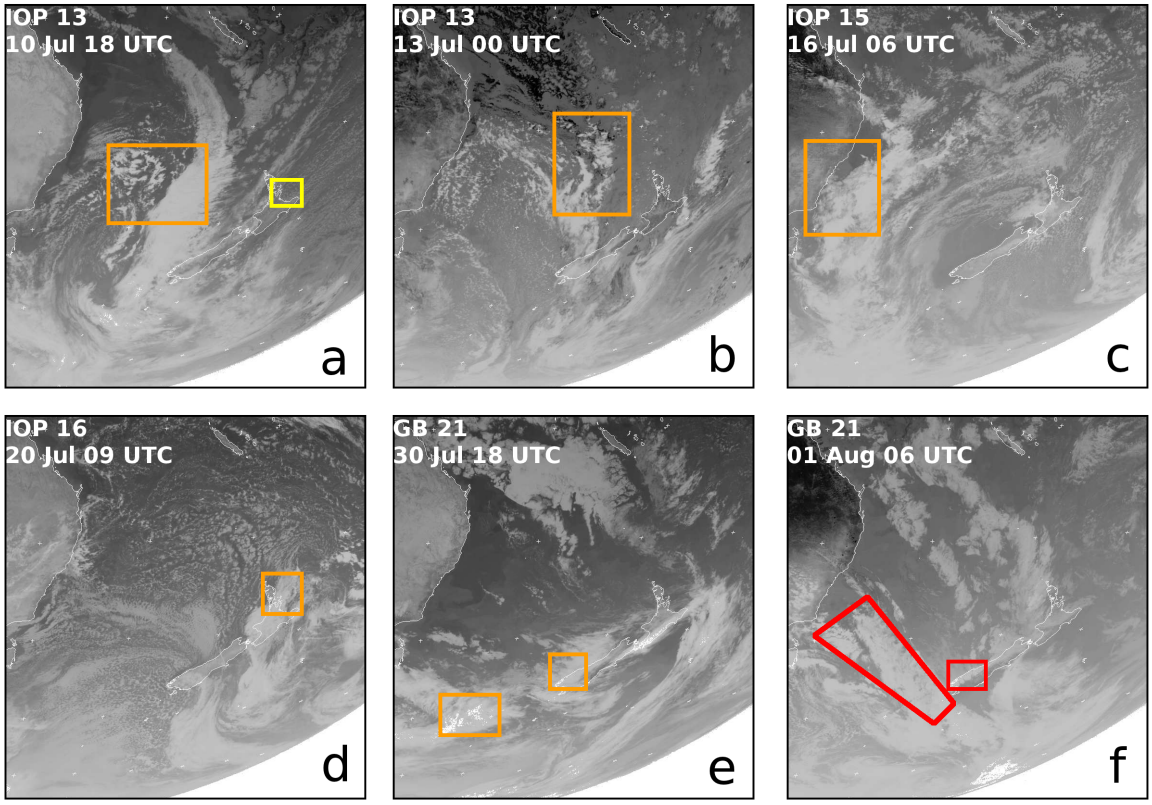

Figure 5.3: Same as Figure 5.2 but for IOP 13 (a,b), 15 (c), 16 (d) and GB 21 (e,f). Red boxes mark high (≈> 1000 Strokes) lightning activity.

convective conditions investigated by Lane et al. (2003). A contribution of convectively generated inertia-GWs in stratospheric observations at NZ is conceivable even when the convection occurred away from NZ over the Tasman Sea due to the ability of inertia-GWs to propagate over large horizontal distance.

There is a higher correlation of *KE* and *VE* with jet wind speed (mean horizontal wind speed from soundings between 8 and 13 km altitude) and low level wind speed (mean horizontal wind speed from soundings between 1 and 3 km altitude) than with the hour of the day (Fig. 5.1). The low level wind speed characterizes the forcing conditions for MWs. Largest correlation is found for *VE* in the troposphere and the low level wind speed (Fig. 5.1i) with a correlation coefficient of 0.66. The correlation of *KE* with the low level wind speed is at least 0.45 (Fig. 5.1c, f). The correlation is smaller for *VE* in the stratosphere and the low level wind speed. *VE* in the stratosphere does not show a further increase for wind speeds larger than 17 m s^{-1} (Fig. 5.1l). This is in agreement with previous findings (Sec. 4.2.2) which showed that too strong forcing likely causes the MWs to break at lower levels. In addition, stronger forcing is often associated with a stronger jet (the correlation coefficient between the low level wind speed and the jet

wind speed from soundings is 0.69) and larger vertical shear (Fig. 4.11). This enhances the probability for wave reflection in the troposphere (Sec. 1.2). Reduced *VE* is found for a jet wind speed between 25 and 50 m s^{-1} for many soundings in the troposphere and stratosphere (Fig. 5.1h, k).

All those findings support the assumption that the vertical velocity perturbations from soundings are indeed caused by MWs. The correlation of the inertia-GW activity (*KE*) and the low level wind speed points towards an overall connection of inertia-GWs and MWs. This is further supported by the correlation (0.88) between the mean IOP values of *KE* in the stratosphere (Fig. 4.14) and *VE* in the troposphere (Fig. 4.21), i.e. between stratospheric inertia-GW activity and tropospheric MW activity. However, when the energies of individual soundings are correlated, the correlation coefficient is smaller (0.36). This suggests a possible temporary larger contribution of other sources of inertia-GWs.

5.2 Impact of the Tropopause

So far, the presented results showed that non-hydrostatic MWs are found in the sounding data in the stratosphere (Figs. 4.21 and 4.22) although they are often evanescent in the upper troposphere and despite possible reflection and trapping at the tropopause. This suggests their leakage from the troposphere across the tropopause into the stratosphere. This finding was further strengthened by their occurrence together with hydrostatic MWs simulated by ECMWF IFS and orographic wave activity in aircraft measurements. Leakage into the stratosphere was previously also found by Lane et al. (2000) who focused on one high-resolution radiosonde released from Christchurch at the east coast of NZ.

As far as the author knows, investigations similar to the following investigation and assessment of the impact of the tropopause on MW activity and propagation by means of radiosonde measurements has not been done and published before. The ratio between *VE* of the stratosphere (13-27 km) to *VE* of the troposphere (1-8 km) is around 10.3 if an exponential growth of the MWs' vertical velocity amplitude due to decreasing density[8], which is valid for vertically constant background conditions without wave breaking, reflection or trapping, is assumed.

The ratios of *VE* computed from soundings for all IOPs is shown in Figure 5.4. They lie well below the value for ideal wave propagation. Besides tropopause related processes as wave trapping, reflection and leakage (Sec. 2.2), reflection by vertical shear (Sec 1.2) and also the time difference between the measurements in the troposphere and in

[8] $\mathrm{Re}(A_w \cdot \exp[i(kx + ly + mz - \omega t) + \frac{z}{2H}])$ [Eq. (2.10)] with $A_w = 1$, $k = m = 2\pi/(10\text{ km})$, $l = 0$, $z = 0 - 28$ km, $x = 0 - 280$ km, $t = 0$, $H = 7$ km

the stratosphere (the sounding takes about 1.5 hours to reach 27 km altitude) can influence the ratio determined from sounding data. Hence, the ratio between *VE* of the stratosphere to *VE* of the troposphere is not a suitable quantity to assess the impact of the tropopause (isolated from other processes causing reflection and dissipation) on MWs propagation and activity in the stratosphere. So another approach is necessary if it is possible at all to assess the effect of the tropopause on the MW activity in the stratosphere from the radiosonde measurements.

It is known from theory and idealized simulations (Sec. 2.2) that the amount of wave energy downstream in the stratosphere with respect of the effects of the tropopause should vary in dependence of trapping on the TIL and the strength of reflection at the tropopause. ECMWF mean profiles for the region of the SI of NZ revealed variable sharpness and strength of the TIL which should result in variable amount of wave reflection. The latter was found by means of variable vertical energy fluxes simulated by WRF (Sec. 4.2.2). Idealized simulations have revealed that trapping can also occur on the TIL if its strength is large enough (2.2). Therefore, the maximum change of potential temperature ($\Delta\theta$) over 1 km between 8 and 13 km altitude determined from sounding data is used as a predictor to account for the effect of the tropopause in a simple multiple linear regression model for *VE* in the stratosphere. The larger $\Delta\theta$ the more likely is trapping on the TIL and the stronger is the reflection (Fig. 4.4). $\Delta\theta$ was computed over 1 km altitude because otherwise small wave perturbations present in the potential temperature profiles (no appropriate background fit can preserve the true strength of the TIL (Sec. 3.2.4)) would have caused large local values not representative for $\Delta\theta$ at the tropopause itself. This is illustrated in Figure 5.5 which also shows $\Delta\theta$

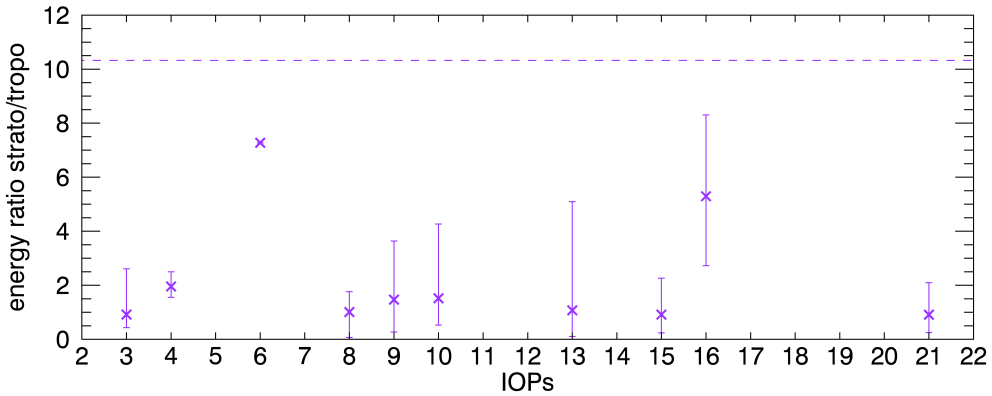

Figure 5.4: Ratio of *VE* in the stratosphere and *VE* in the troposphere as mean values for all IOPs. Bars mark the minimum and maximum values occurring during an IOP. Dashed line gives the ratio assuming an exponential growth of the vertical velocity amplitudes due to decreasing density valid for vertically constant background conditions without wave breaking, reflection or trapping.

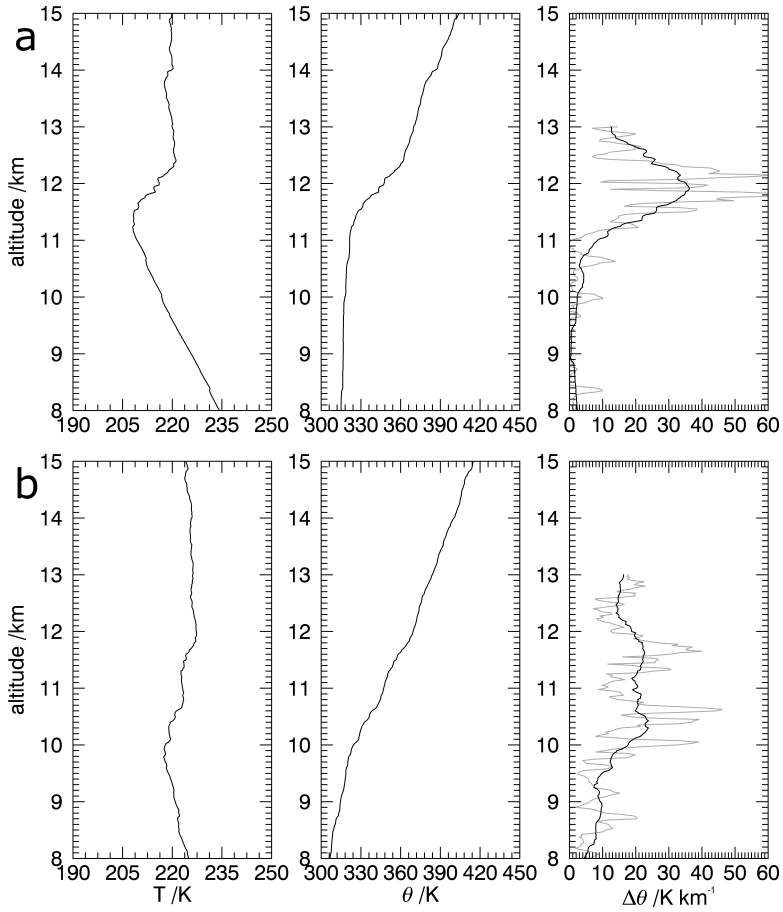

Figure 5.5: Example profiles of temperature, potential temperature and $\Delta\theta$ computed over 1 km altitude (black) and 100 m altitude (gray, values were multiplied by 10 to get K km^{-1}) for (a) 11 July 08:34 UTC (IOP 13) (b) 16 June 11:40 UTC (IOP 4).

computed over 100 m intervals. The values for $\Delta\theta$ for all soundings lie in the range of 16 to 42 K km^{-1} (Fig. 5.6). Values below and around 22 K km^{-1}, which is the mean value of all soundings above 13 km altitude, represent a smooth transition from troposphere to stratosphere without pronounced inversion (e.g. Fig. 5.5b). The values of $\Delta\theta$ around and above 30 K km^{-1} should be large enough to allow for trapping on the TIL. In any case, wave reflection at the tropopause can be expected (Fig. 4.4b).

When MW activity (*VE*) in the stratosphere is related to the strength of the tropopause, one needs also to account for the variable forcing conditions (Sec 4.2.1) which were found to be linearly correlated with *VE* with a correlation coefficient of 0.396 (Fig. 5.1l). The linear correlation coefficient of a multiple linear regression of $\Delta\theta$ and low level wind speed for *VE* in the stratosphere with the original data of *VE* is 0.434, i.e. 0.038 larger than when only low level wind speed is used. This is a quite small increase. Hence, the

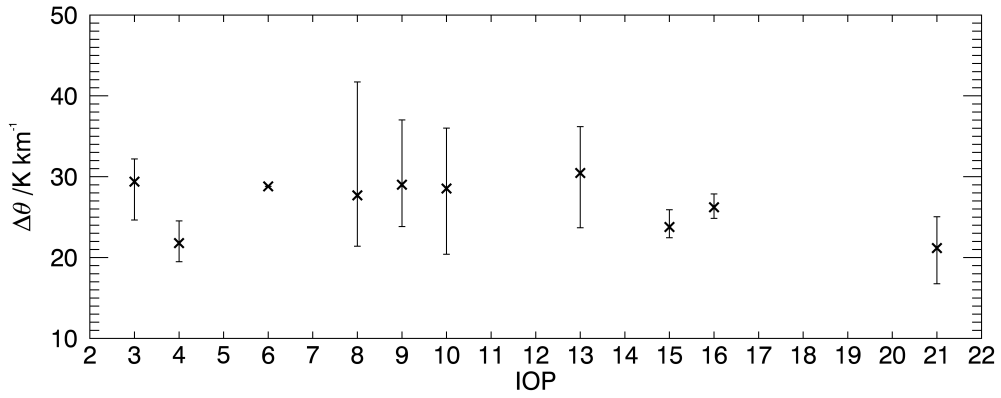

Figure 5.6: Maximum occurring vertical change of potential temperature computed over 1 km altitude from soundings, i.e. showing the strength of the TIL, as mean values for all IOPs. Bars mark the minimum and maximum values occurring during an IOP.

question is if this increase is robust or simply caused by certain single values of $\Delta\theta$.

The multiple linear regression was computed for 10000 subsets each consisting of 44 different soundings, i.e. 3/4 of the total number of soundings analyzed (Tab. 3.1). The distribution of the corresponding correlation coefficient is shown together with the distribution of the correlation coefficient of the subsets based only on the low level wind speed in Figure 5.7. Although the absolute values of the correlation coefficients vary for the subsets and also reach significantly smaller or larger values than the ones determined from all soundings, the majority of the subsets lead to values close to 0.396 for the low level wind speed (red line) and close to 0.434 for the multiple linear regression including $\Delta\theta$ (black line). More important, the difference between the two distributions is found over the whole range of determined correlation coefficients, i.e. the whole distribution for the multiple linear regression is shifted by about 0.04 compared to the distribution for correlation with only the low level wind speed. This confirms that there is an impact of the tropopause on the observed variability of MW activity in the stratosphere albeit the effect of the low level forcing dominates. Not only because low level forcing is necessary to trigger MWs that can reach the stratosphere but also because the changes of the forcing are more pronounced (Sec. 4.2.1) than the changes of the tropopause strength (Figs. 4.9 and 5.6). Therefore, the low level forcing largely controls the variability of the MW activity not only in the troposphere but also in the stratosphere (Figs. 4.21 and 5.1i, l). By the way, the correlation of the multiple linear regression of VE in the stratosphere can be further slightly increased to 0.440 when also the vertical shear (difference between jet wind speed and low level wind speed) is included as predictor.

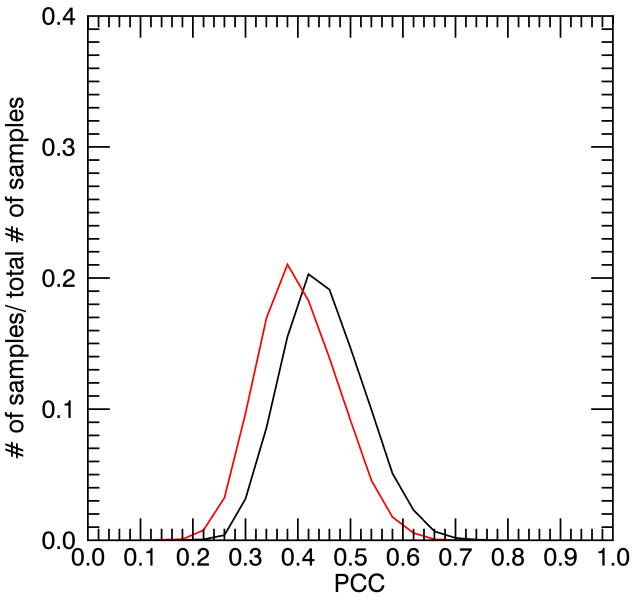

Figure 5.7: Distribution of the linear Pearson correlation coefficient between *VE* in the stratosphere and low level wind speed (red) and multiple linear regression with low level wind speed and $\Delta\theta$ (black) for 10000 subsets (= total # of samples) each consisting of 44 different soundings.

6 Summary and Conclusion

Background conditions in Earth's atmosphere are rarely constant, neither in time nor in space, which affects the propagation of atmospheric gravity waves (GWs) and their way of distributing momentum and energy in the atmosphere. Changes of density and temperature in the lower atmosphere (troposphere and lower stratosphere) are most pronounced in the lower troposphere and at the tropopause. Mountain waves (MWs) do not only propagate vertically above the mountains as described by the 2-dimensional linear hydrostatic solution of the equations of motion. MWs can be trapped at boundary-layer inversions in the lower troposphere, i.e. interfacial waves (Vosper 2004, Sachsperger et al. 2015). This thesis showed by means of idealized numerical simulations that MWs can also be trapped on the tropopause inversion layer (TIL) if the strength of the inversion, which is defined as the change in potential temperature across the tropopause, is large enough. The applicability of the linear estimate of the existence of trapped MWs for the TIL can be confirmed. For vertically constant wind, the strength of the TIL must be twice as large as for inversions in the troposphere due to the larger stability of the stratosphere. The TIL must be even stronger for higher wind speed. The horizontal wavelength of the interfacial waves decreases with increasing stability above the inversion. Moreover, the simulations showed that reflected waves exist downstream of the mountain in the troposphere even without a decrease of Scorer parameter with altitude, which is the classical condition for trapped waves in the troposphere. Their amplitudes are larger if an inversion is present at the tropopause than if there is just the jump from tropospheric to stratospheric stability. In addition, horizontal wavelengths of propagating, interfacial, and reflected waves increase with increasing wind speed.

The meteorological conditions at New Zealand (NZ) during DEEPWAVE were evaluated to investigate the propagation of MWs into the stratosphere in the real atmosphere. Local tropospheric climatological indices (SOI, SAO) suggest a tendency for southwesterly flows and blocking over NZ during DEEPWAVE (Sec. 4.2.1). A classification of the tropospheric flow regimes according to Kidson (2000) and Renwick (2011) revealed that the blocking regimes with an occurrence frequency of 36 % and the SW regime with a frequency of about 18 % were the most frequent ones which occurred in June/July/August (JJA) 2014. Compared to the values found by Renwick (2011) for JJA of 1958...2010, the occurrence frequency was twice as high in JJA 2014 for the HSE regime (21.7 % vs. 10.6 %) and enhanced for the SW regime (17.9 % vs.

11.3 %). Altogether, the trough group regimes were underrepresented compared to the 40-year climatology of Kidson (2000). Many DEEPWAVE aircraft MW missions were conducted during the TNW regime. On five out of seven days when the TNW regime occurred in June and July 2014 aircraft missions were devoted to observe deep propagating orographic GWs and in the majority of cases significant and strong MW activity was found (Tab. 4.3). During the flight planning process, the weak cross-mountain wind component at 700 hPa occurring during the SW regimes caused only weak forcing conditions, which often disqualified MWs as primary targets for selected missions. For the IOPs 6 and 10, which were conducted during the SW regimes, moderate and even strong MW activity was reported at flight level and also in the mesosphere and lower thermosphere.

The TIL was a dominant feature of the upper troposphere and lower stratosphere during the DEEPWAVE period but varied in strength (Fig. 4.9). A simplified reflection coefficient for hydrostatic GWs was calculated for JJA 2014 using both the representative buoyancy frequencies N_T and N_S from the troposphere and stratosphere and maximum values N_{MAX} attained within the TIL. The approximated hydrostatic reflection coefficient showed significant enhancement from reaching up to 0.6 when the N-peak of the TIL was taken into account. A reflection coefficient $r \geq 0.5$ was associated with a reduction of the vertical energy flux between 4 and 12 km altitude simulated by WRF and suggests significant partial reflection of vertically propagating GWs at the tropopause. In accordance with the climatology, the subtropical jet stream (STJ) was the dominant tropopause jet within the DEEPWAVE region and period. A double jet structure consisting of STJ to the north and polar front jet stream (PFJ) to the south was present on nearly all days in July and August 2014. The analysis of the positions and strengths of both jets revealed that the STJ was located south in the vicinity of NZ, e.g. south of 35 °S at 169 °E, most often in June while the PFJ was located in the vicinity of NZ, e.g. north of 52 °S at 169 °E, most often in July (Fig. 4.11b). The STJ was most often involved in strong forcing events of MWs at the Southern Alps. The PFJ was typically responsible for moderate and weak tropospheric forcing of MWs.

Mean GW activity in the stratosphere during DEEPWAVE from sounding data (Sec. 4.3) was 13.0 J kg^{-1}, 6.9 J kg^{-1} and 0.6 J kg^{-1} for the horizontal kinetic wave energy, potential wave energy, and vertical kinetic wave energy, respectively. The intrinsic frequencies of the waves in the horizontal velocity perturbations were close to the inertial frequency f. Moreover, rotary spectra and Stokes analysis show dominant upward propagation of wave energy in the stratosphere which suggests the source of those waves being in the troposphere or at the tropopause. The horizontal propagation direction of wave energy is dominated by the background winds and mainly to eastward directions in the stratosphere which suggests the source of those waves being somewhere to the west of Lauder. Vertical wavelengths of mainly 2 to 4 km and horizontal wavelengths of some hundreds kilometers are the scales found for the inertia-GWs in the stratosphere.

Analyses of vertical velocity perturbations determined from the ascent rate of the soundings revealed non-hydrostatic MWs having horizontal and vertical scales of tens of kilometers and downstream energy propagation. Although often evanescent in the upper troposphere, those non-hydrostatic MWs were also found in the lower and mid stratosphere which suggests their leakage from troposphere across the tropopause into the stratosphere. Those waves were found to occur together with hydrostatic MWs in ECMWF and orographic wave activity in aircraft measurements which strengthened their classification as MWs.

Coming back to the first hypothesis raised in the introduction (Sec. 1.3) which reads "measurements of GWs by radiosondes in a mountainous region can be uniquely assigned to orographic sources", it can be stated that the vertical velocity perturbations from soundings at NZ are dominated by MWs, namely non-hydrostatic MWs. It was found that the stratospheric horizontal velocity perturbations are largely connected to MWs but temporary influence of other sources which were present in the region of NZ during DEEPWAVE (i.e. the upper tropospheric jet, convection and fronts) is likely. The question whether this mountain related inertia-GWs are caused by adjustment of the large-scale flow due to the main MWs or whether they are hydrostatic MWs influenced by rotation (Sec. 3.2.4 and 4.3.2) remains open. If stationarity is assumed, the horizontal wavelength of the inertia-GWs in the troposphere are in the expected range of the horizontal scales of MWs over NZ which is up to 400 km as revealed by airborne data (Smith and Kruse 2017). However, the determined horizontal wavelengths reach values larger than 500 km for a large part of the soundings in the stratosphere. On the one hand, the results may reveal that the inertia-GWs in the stratosphere are not hydrostatic MWs. On the other hand, the results may reveal that the hydrostatic MWs are no longer stationary in the stratosphere for a large part of the soundings. The latter might be explained by the transience of the MW events at NZ due to the migrating weather systems (Sec. 4.2).

For the second hypothesis which reads "the impact of the tropopause on MW propagation as predicted by theory can be confirmed by radiosonde measurements", it was shown at first that model data (Sec. 2.2 and 4.2.2) show a clear influence of the TIL on MWs (reflection and trapping). The radiosonde measurements do not allow to directly observe the predicted wave reflection and wave trapping at the tropopause. However, they revealed conditions at the tropopause ($\Delta\theta$) over NZ which should cause reflection and likely also allow for trapping on the TIL. Multiple linear regression revealed at least a small dependence of the stratospheric MW activity in the sounding data on the strength of the TIL. In addition, the occurrence of non-hydrostatic MW in the stratosphere showed the propagation or leakage of these waves from the troposphere across the tropopause into the stratosphere.

Overall, it can be concluded that the GWs spectrum in the lower atmosphere (troposphere and lower stratosphere) in mountainous regions contains different modes of

MWs. Propagating, reflected, and interfacial MWs were simulated with highly idealized numerical simulations. Low to high frequency GW modes over NZ were quantified from radiosonde data with different analysis methods and their upward and downstream propagation was revealed for the stratosphere. A clear assessment of the influence of the tropopause on MWs in the real atmosphere requires particular case studies which make also use of additional measurements (e.g., airborne wind lidar measurements under favourable measurements conditions (Sec. 7)).

7 Outlook

Further insight into the impact of the tropopause on MWs by means of additional measurements is desirable not only because of the modification of the way wave energy is distributed in the atmosphere but also because commercial aircraft tend to fly in the tropopause region. Breaking and trapped MWs can cause turbulence (Sharman et al. 2012).

The DLR wind lidar is one instrument which allows for vertical velocity measurements of non-hydrostatic MWs. Trapped waves in the troposphere were already observed and analyzed successfully in the lee of isolated islands with the wind lidar (Chouza et al. 2016). The coverage of the wind lidar measurements was reduced due to missing backscatter, i.e. aerosols, during DEEPWAVE. Data of better coverage were gained during the GW-LCYCLE 1 & 2 campaigns in Scandinavia (Wagner et al. 2017, Witschas et al. 2017). A quicklook of vertical wind measured over Southern Scandinavia during a MW event is shown in Fig. 7.1a.

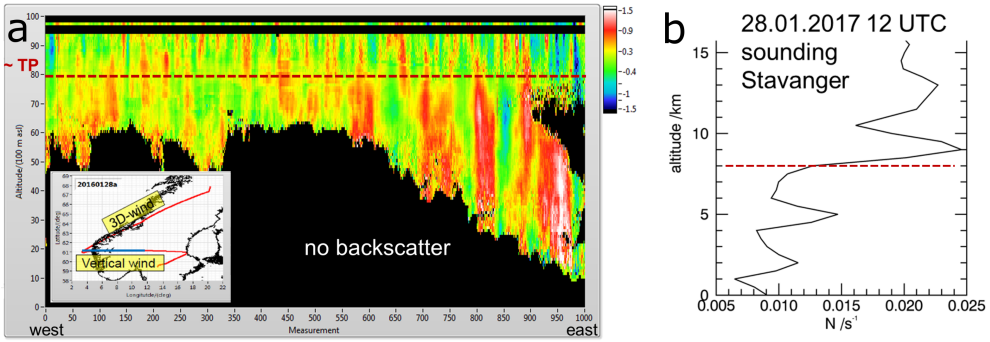

Figure 7.1: Quicklook of vertical velocity measured with the wind lidar along the blue line of the flight track from 0 to 9.5 km altitude and vertical velocity measured insitu at 9.8 km altitude created by B. Witschas (a) and Brunt-Vaisälä frequency of corresponding upstream sounding in Norway (b). Sounding data taken from http://weather.uwyo.edu/upperair/sounding.html.

An impressive change of the horizontal wave scales is found at the tropopause which shows some similarity with the idealized numerical simulation, i.e. shorter horizontal wavelengths of the waves on the inversion compared to the reflected waves in the

troposphere. The stability profile of an upstream sounding shows a peak right above the tropopause indicating the TIL (Fig. 7.1b) where trapping on the inversion and increased wave reflection likely happened. Since such measurements by research aircraft are limited to certain regions, they need to be combined and complemented with numerical simulations and globally available measurements (e.g., from radiosondes) to assess the influence of the tropopause globally.

A Appendix

A.1 Inertia-GWs

GW energy The average intrinsic frequency of low frequency GWs can also be estimated from horizontal kinetic and potential energies (Eqs. (3.10) and (3.11)) by

$$\Omega/f = \sqrt{\frac{\left\langle \overline{KE}/\overline{PE} \right\rangle + 1}{\left\langle \overline{KE}/\overline{PE} \right\rangle - 1}}, \tag{A.1}$$

(Geller and Gong 2010). Here, $\langle . \rangle$ denotes the mean over the soundings of an IOP.

As expected the intrinsic frequencies based on *KE* and *PE* are close to f with the mean values being $1.6f$ for troposphere and $1.7f$ for stratosphere. The results for average intrinsic frequency in terms of the inertial frequency (Ω/f) for all IOPs are given in Table A.1. Mean intrinsic frequencies equal to or higher than $2f$ are found for IOP 15, IOP 16 and IOP 21 in either the troposphere or the stratosphere or in both. The intrinsic frequencies determined from *KE* and *PE* lie around $1.6f$ for troposphere and $1.7f$ for stratosphere, which is similar to the results of Geller and Gong (2010) for soundings at northern hemispheric mid-latitudes in the United States. Only their tropospheric values tend to somewhat higher values between 1.7 and $2.8f$ with a mean value of approximately $2.5f$.

Table A.1: Ω/f determined using *KE* and *PE*

	IOP									
	3	4	6	8	9	10	13	15	16	21
troposphere	1.5	1.2	1.5	1.5	1.5	1.2	1.3	2.0	1.8	2.4
stratosphere	1.3	1.5	1.8	1.6	1.6	1.7	1.8	1.5	2.1	2.0

Table A.2: Mean degree of polarization (d) of the Lauder soundings for all IOPs

	IOP									
	3	4	6	8	9	10	13	15	16	21
troposphere	0.54	0.72	0.73	0.58	0.48	0.60	0.60	0.84	0.52	0.55
stratosphere	0.52	0.46	0.18	0.58	0.59	0.44	0.44	0.51	0.51	0.42

Stokes Analysis For the Lauder soundings the mean degree of polarization (d) calculated from Stokes parameter for every IOP is given in Table A.2.

The influence of the soundings with a lower degree of polarization is investigated by comparing the derived GW properties from all soundings to properties from the soundings with a degree of polarization larger than or equal to 0.5. In addition, results for soundings with d larger than or equal to 0.5 and an intrinsic frequency $\Omega/f < 10$ were computed as well. The latter precondition comes from the fact that the method is meant for low frequency waves. The number of soundings of an IOP fulfilling those conditions is given in Table A.3.

Table A.3: Number of soundings with a degree of polarization larger than or equal 0.5 (top lines) and with a degree of polarization larger than or equal 0.5 and in addition Ω/f smaller than 10 (bottom lines) for all IOPs

		IOP									
		3	4	6	8	9	10	13	15	16	21
$d \geq 0.5$	troposphere	4	2	1	5	4	10	11	3	2	2
	stratosphere	5	2	-	4	7	4	5	1	3	-
$d \geq 0.5$	troposphere	4	2	1	4	2	6	8	1	1	1
& $\Omega/f < 10$	stratosphere	5	2	-	4	7	3	5	1	3	-

The direction of horizontal phase propagation is determined for every sounding. Afterwards, the dominant propagation direction for every IOP is calculated by transforming the direction from polar coordinates (previously determined angle and a radius of 1) to Cartesian coordinates (x and y components). Then the mean is taken over the x and y components of the soundings of an IOP and retransformed to polar coordinates. For example, three directions 180, 170 and 10° then lead to a dominant direction of 161°. This is different from the arithmetic mean being 120° which does not have any meaning with respect to the dominant propagation direction. The dominant intrinsic horizontal phase propagation direction was found to be mainly towards NW in the troposphere

and towards W to S in the stratosphere (Table A.4). To test the sensitivity of the results on the soundings contributing to it, dominant propagation directions including only soundings with $d \geq 0.5$ and $d \geq 0.5$ and $\Omega/f < 10$ are also listed in Table A.4. Some changes can be seen but the overall directions stay roughly the same.

Table A.4: Dominant intrinsic horizontal propagation direction of the IOPs in degrees clockwise from North from all Lauder soundings (top lines), from soundings with a degree of polarization larger than or equal 0.5 (middle lines) and with a degree of polarization larger than or equal 0.5 and in addition Ω/f smaller than 10 (bottom lines).

		IOP									
		3	4	6	8	9	10	13	15	16	21
all	tropo	285	342	201	304	321	223	327	327	171	308
	strato	268	219	333	279	288	232	257	195	248	233
$d \geq 0.5$	tropo	262	315	201	321	322	230	322	327	200	294
	strato	278	190	-	288	282	216	279	183	242	-
$d \geq 0.5$	troposphere	262	315	201	266	304	229	336	314	196	251
& $\Omega/f < 10$	stratosphere	278	190	-	288	282	210	279	183	242	-

When the mean propagation directions of the IOPs as revealed by the two methods are compared (Table A.5), the mean difference is found to be smaller being 12°. The good agreement for nearly all IOPs between the two methods for the mean propagation directions increases the confidence in the results. Of course both methods are based on the same idea of determining the horizontal propagation direction but the technical implementation is different.

Table A.5: Difference between the two methods for mean horizontal propagation direction for all soundings for all IOPs in degree.

	IOP									
	3	4	6	8	9	10	13	15	16	21
tropo	5	4	3	8	8	10	7	54	4	17
strato	3	1	46	11	5	14	2	28	8	1

The determined frequencies tend to be more variable in the troposphere. This is also true, when looking at the mean values for the IOPs given in Table A.6. Again, to test

the sensitivity of the results, values only including soundings with $d \geq 0.5$, and with $d \geq 0.5$ and $\Omega/f < 10$ are also shown. In the stratosphere the intrinsic frequencies are reduced a little bit when only soundings with $d \geq 0.5$ are included. The restriction of $\Omega/f < 10$ only has a minor effect for the stratosphere since most of the values are smaller than 10 anyway. In the troposphere mean values are reduced when applying those restrictions but they are still higher than in the stratosphere. Overall, these intrinsic frequencies are larger than the intrinsic frequencies based on *KE* and *PE* (Tab. A.1). This bandwidth of the results is used to quantify the reliability of the deduced GW properties.

Table A.6: Mean intrinsic frequencies Ω/f from Stokes analysis for all Lauder soundings (top lines) and for soundings with a degree of polarization larger than or equal 0.5 (middle lines) and with a degree of polarization larger than or equal 0.5 and in addition Ω/f smaller than 10 (bottom lines) for all IOPs.

		IOP									
		3	4	6	8	9	10	13	15	16	21
all	tropo	2.8	7.0	6.0	16.0	7.4	10.4	12.3	13.6	7.7	7.1
	strato	2.0	2.0	3.4	3.6	2.0	3.6	2.0	35.4	5.3	13.5
$d \geq 0.5$	tropo	2.5	6.4	6.0	18.3	12.5	10.5	14.5	13.6	9.2	9.8
	strato	1.2	2.3	-	3.2	2.1	4.8	1.6	1.8	2.9	-
$d \geq 0.5$	tropo	2.5	6.4	6.0	3.2	2.4	5.0	5.3	4.1	6.0	6.6
& $\Omega/f < 10$	strato	1.2	2.3	-	3.2	2.1	1.6	1.6	1.8	2.9	-

Vertical and horizontal wave numbers/wavelengths The mean values for the vertical wavelength for all IOPs are given in Table A.7. The absolute deviations of the mean values depending on the soundings included ($d \geq 0.5$, $\Omega/f < 10$) lie below 700 m except for IOP 15 and IOP 16 in the troposphere.

The mean values of the horizontal wavelength for all IOPs based on the values of the single soundings are given in Table A.8. When the mean horizontal wavelength for the IOPs is determined directly using the mean vertical wavelength (Tab. A.7), the mean intrinsic frequency (Tab. A.6) and the mean Brunt-Vaisälä frequency the results are quite different as can be seen also in Table A.8. It was mentioned earlier that the difference in the derived intrinsic frequency from *KE* and *PE* (Tab. A.1) and from Stokes analysis can be used to test the reliability of the results. Therefore, horizontal wavelengths were also computed using the mean intrinsic frequency from *KE* and *PE*. Results are also listed in Table A.8. This comparison highlights the uncertainty of the determined horizontal wavelength of inertia-GWs from radiosoundings with

Table A.7: Mean vertical wavelengths λ_z in km for all IOPs for all Lauder soundings.

		IOP									
		3	4	6	8	9	10	13	15	16	21
all	tropo	3.2	5.8	3.5	4.1	5.2	3.7	4.1	5.9	4.1	5.9
	strato	2.9	4.3	2.8	3.3	3.3	2.8	3.4	2.2	2.7	3.7
$d \geq 0.5$	tropo	3.5	5.3	3.5	4.2	5.9	3.7	4.5	5.9	2.9	5.9
	strato	2.7	4.7	-	3.2	3.2	3.3	4.1	1.6	2.7	-
$d \geq 0.5$	tropo	3.5	5.3	3.5	4.4	4.7	3.8	4.4	3.5	3.5	7.0
& $\Omega/f < 10$	strato	2.7	4.7	-	3.2	3.2	3.3	4.1	1.6	2.7	-

these methods. The finding is in agreement with Zhang et al. (2004) who reported important uncertainties when deriving GW properties from radiosonde data. In the case of a mostly monochromatic inertia-GW packet, they found that estimates of vertical wavelength and intrinsic phase speed tend to be more accurate than that of intrinsic frequency and horizontal wavelength.

Table A.8: Mean horizontal wavelengths λ_h computed as mean over single soundings (top 6 lines), computed from mean values of vertical wavelength, intrinsic frequency and Brunt-Vaisälä frequency (lines 7-8) and computed from mean values but with intrinsic frequency from *KE* and *PE* (lines 9-10) in km for all IOPs for Lauder soundings.

		IOP									
		3	4	6	8	9	10	13	15	16	21
all	tropo	196	85	65	205	146	65	76	57	145	233
	strato	690	617	173	222	722	350	604	90	262	204
$d \geq 0.5$	tropo	283	89	65	231	157	68	71	57	44	64
	strato	1014	647	-	254	721	471	666	204	334	-
$d \geq 0.5$	tropo	283	89	65	288	284	98	93	90	69	100
& $\Omega/f < 10$	strato	1014	647	-	254	721	613	666	204	334	-
all	tropo	129	71	65	23	57	35	28	41	50	79
	strato	323	458	173	181	365	146	343	10	98	54
all	tropo	313	758	340	324	398	497	451	317	256	251
	stratoe	674	702	364	521	471	384	410	341	279	407

Phase speed and group velocity Mean values of absolute intrinsic horizontal phase speeds for all IOPs based on values from single soundings are given in Table A.9. There are only small changes (most often < 3 m s^{-1}) when the soundings are restricted by the degree of polarization and the intrinsic frequency. In addition, mean intrinsic phase speeds were computed using mean vertical wavelength (Tab. A.7), mean intrinsic frequency from *KE* and *PE* (Tab. A.1) and mean horizontal wavelength based on mean intrinsic frequency from *KE* and *PE* (Tab. A.8) for all IOPs. Overall there is a good agreement between the mean intrinsic horizontal phase speeds computed as mean over the intrinsic horizontal phase speeds of single soundings and the mean intrinsic horizontal phase speeds derived from mean quantities based on *KE* and *PE*. This suggests that the results for the mean horizontal intrinsic phase speeds is robust. Uncertainties in intrinsic frequency and horizontal wave number or wavelength cancel out.

Table A.9: Mean intrinsic horizontal phase speeds computed as mean over single soundings (top 6 lines) and computed from mean values based on *KE* and *PE* (bottom lines, for detailed description see text) for all IOPs for Lauder soundings.

		IOP									
		3	4	6	8	9	10	13	15	16	21
all	tropo	6.9	9.0	6.4	7.6	8.7	6.5	6.6	10.1	8.1	11.0
	strato	16.1	17.6	9.7	11.3	17.2	11.3	15.4	7.4	10.4	13.6
$d \geq 0.5$	tropo	8.4	8.4	6.4	8.1	10.5	6.6	7.1	10.1	5.3	8.7
	strato	19.4	19.1	-	11.2	17.2	14.0	17.6	6.1	10.8	-
$d \geq 0.5$	tropo	8.4	8.4	6.4	8.5	10.3	6.9	7.1	6.1	6.8	10.8
& $\Omega/f < 10$	strato	19.4	19.1	-	11.2	17.2	14.8	17.6	6.1	10.8	-
all	tropo	7.5	14.9	8.5	8.0	9.5	10.1	9.3	10.4	7.6	10.0
	strato	14.5	17.8	11.0	13.5	12.7	10.5	12.2	8.1	9.5	13.7

Table A.10 shows the mean values of the absolute intrinsic vertical phase speeds for all IOPs. The intrinsic vertical phase speed is affected stronger by the soundings included and also the values computed from mean values based on *KE* and *PE* are often smaller, especially in the troposphere. This is different to the horizontal phase speed and can be explained by the fact that m and Ω are determined independently while k_h is calculated using Eq. (2.14) in dependence of Ω.

For completeness Table A.11 and Table A.12 show the mean ground-based horizontal and vertical phase speeds as mean values for all IOPs. As for the overall values the ground-based horizontal phase speeds are an order of magnitude larger than the

Table A.10: Mean intrinsic vertical phase speeds computed as mean over single soundings (top 6 lines) and computed from mean values based on *KE* and *PE* (bottom lines, for detailed description see text) for all IOPs for Lauder soundings.

		IOP									
		3	4	6	8	9	10	13	15	16	21
all	tropo	0.15	0.66	0.35	0.93	0.74	0.61	0.98	1.48	0.42	0.57
	strato	0.11	0.15	0.16	0.19	0.10	0.19	0.11	1.96	0.25	0.93
$d \geq 0.5$	tropo	0.14	0.51	0.35	1.07	1.42	0.62	1.23	1.48	0.41	0.75
	strato	0.05	0.18	-	0.16	0.10	0.27	0.11	0.05	0.15	-
$d \geq 0.5$	tropo	0.14	0.51	0.35	0.20	0.23	0.31	0.40	0.24	0.35	0.76
& $\Omega/f < 10$	strato	0.05	0.18	-	0.16	0.10	0.09	0.11	0.05	0.15	-
all	tropo	0.08	0.11	0.09	0.10	0.12	0.07	0.08	0.19	0.12	0.23
	strato	0.06	0.11	0.08	0.08	0.09	0.08	0.10	0.05	0.09	0.12

ground-based vertical phase speeds. More importantly, Table A.13 shows the fraction of the soundings for which the intrinsic phase speeds and ground-based phase speeds are of different direction for all IOPs. It can be seen that there is a clear signal for the Doppler shift by the horizontal wind being strong enough to change the direction of the phase speed in the ground-based frame compared to the moving (intrinsic) frame except for IOP 4 and IOP 15. For IOP 15 this agrees with what was found earlier: that the mean dominant phase propagation being in the direction of the mean wind in the troposphere (Sec. 4.3.1) and no change in sign is possible overall.

Figure A.1 shows the amplitude and direction of all soundings with respect to the IOPs. Largest ground-based group velocities occurred for IOP 10 in the troposphere and for the IOPs 6, 13 and 21 in the stratosphere. While the direction of ground-based group velocities are similar for troposphere and stratosphere for the IOPs 3, 6, 10, 16 and 21, i.e. mainly SW, TSW and W circulation patterns (Sec. 4.2.1), larger differences of more than 50 degrees were found for the other IOPs, i.e. mainly HE and TNW circulation patterns.

Table A.11: Mean ground-based horizontal phase speeds computed as mean over single soundings (top 6 lines) and computed from mean values based on *KE* and *PE* (bottom lines, for detailed description see text) for all IOPs for Lauder soundings.

		IOP									
		3	4	6	8	9	10	13	15	16	21
all	tropo	5.8	7.1	19.0	15.3	6.5	24.5	7.6	15.7	12.9	20.5
	strato	9.2	13.4	2.9	4.6	11.5	7.2	8.1	3.9	7.2	13.5
$d \geq 0.5$	tropo	4.5	4.7	19.0	16.6	7.2	23.8	7.4	15.7	9.3	23.2
	strato	7.7	18.5	-	3.9	12.0	7.4	6.5	0.1	5.5	-
$d \geq 0.5$	tropo	4.5	4.7	19.0	15.5	6.4	24.1	8.1	19.9	11.9	23.2
& $\Omega/f < 10$	strato	7.7	18.5	-	3.9	12.0	8.7	6.5	0.1	5.5	-
all	tropo	5.8	1.3	17.0	9.2	8.7	18.6	6.3	25.3	2.5	20.3
	strato	11.3	7.9	1.5	2.4	7.3	8.3	11.9	3.0	10.9	12.5

Table A.12: Mean ground-based vertical phase speeds computed as mean over single soundings (top 6 lines) and computed from mean values based on *KE* and *PE* (bottom lines, for detailed description see text) for all IOPs for Lauder soundings.

		IOP									
		3	4	6	8	9	10	13	15	16	21
all	tropo	0.14	0.60	1.02	2.91	0.69	2.49	0.77	1.80	0.67	1.49
	strato	0.08	0.13	0.05	0.10	0.06	0.10	0.08	0.27	0.26	1.09
$d \geq 0.5$	tropo	0.09	0.34	1.02	3.41	1.13	2.37	0.85	1.80	0.73	2.15
	strato	0.03	0.18	-	0.07	0.06	0.10	0.04	0.001	0.09	-
$d \geq 0.5$	tropo	0.09	0.34	1.02	0.46	0.14	1.16	0.40	0.78	0.61	1.63
& $\Omega/f < 10$	strato	0.03	0.18	-	0.07	0.06	0.05	0.04	0.001	0.09	-
all	tropo	0.06	0.01	0.18	0.12	0.11	0.14	0.06	0.47	0.04	0.47
	strato	0.05	0.05	0.01	0.02	0.05	0.06	0.10	0.02	0.11	0.11

Phase speed Tropospheric intrinsic horizontal phase speeds are often smaller than 10 m s^{-1} with a mean value of 7.6 m s^{-1} (Fig. A.2a). For the ground-based horizontal phase speeds, one finds that the sign is negative for 76 % of the soundings in the troposphere (Fig. A.2b). This means, that the Doppler shift due to the horizontal wind causes a change of the direction of the phase speed relative to the ground compared to the direction of the intrinsic phase speed. The mean value of the absolute ground-based

Table A.13: Percentage of the soundings with different direction of intrinsic and ground-based phase speeds (top 2 lines) and different direction (yes or no) based on the mean results of *KE* and *PE* (bottom lines, for detailed description see text) for all IOPs for Lauder soundings.

		IOP									
		3	4	6	8	9	10	13	15	16	21
all	tropo	56 %	67 %	100 %	67 %	80 %	92 %	80 %	33 %	75 %	100 %
	strato	78 %	33 %	100 %	67 %	60 %	83 %	60 %	67 %	100 %	67 %
all	tropo	yes	no	yes	yes	yes	yes	yes	no	yes	yes
	strato	yes	no	yes	yes	yes	yes	yes	yes	yes	yes

phase speeds (sign neglected) are larger for the troposphere (12.4 m s^{-1}, Fig. A.2b) than for the stratosphere (8.4 m s^{-1}, Fig. 4.18b).

The negative and positive signs of the intrinsic vertical phase speed are based on the vertical energy propagation found by Stokes analysis. It revealed no dominant vertical propagation direction in the troposphere (Fig. A.2c). The mean values of the absolute values of the intrinsic vertical phase speeds are 0.70 m s^{-1} for the troposphere. As for the horizontal ground-based phase speed, one finds a change of the sign in the ground-based vertical phase speed compared to the intrinsic vertical phase speed for 76 % of the soundings in the troposphere. Because positive and negative intrinsic phase speed exists and one cannot directly see the change in sign in Figure A.2c, d. The direction of the ground-based vertical phase speed in the troposphere was checked for each sounding leading to a change in sign compared to the intrinsic vertical phase speed for 76 % of the soundings.

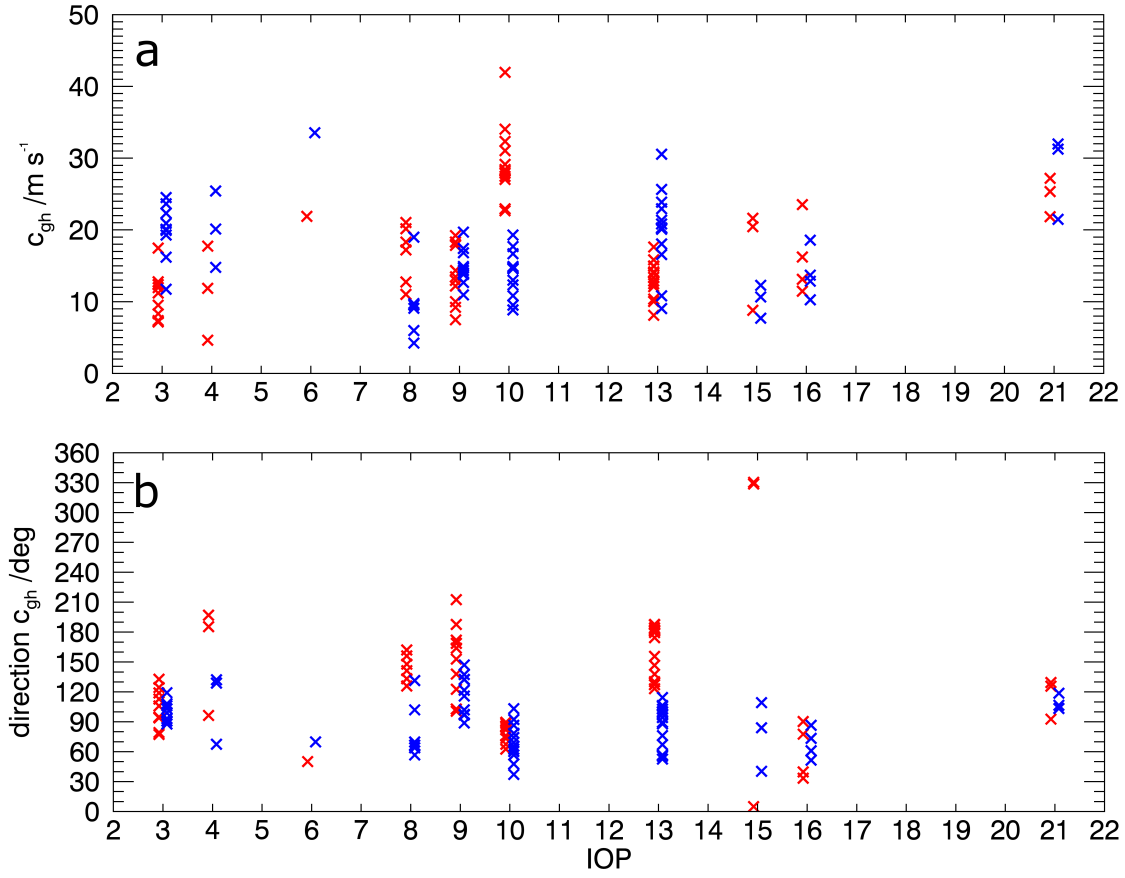

Figure A.1: Amplitude (a) and direction (b) of the ground-based horizontal group velocity for all soundings for all IOPs for troposphere (red ×) and stratosphere (blue ×). Direction is in degrees clockwise from North and gives the direction to which the group velocity vector points.

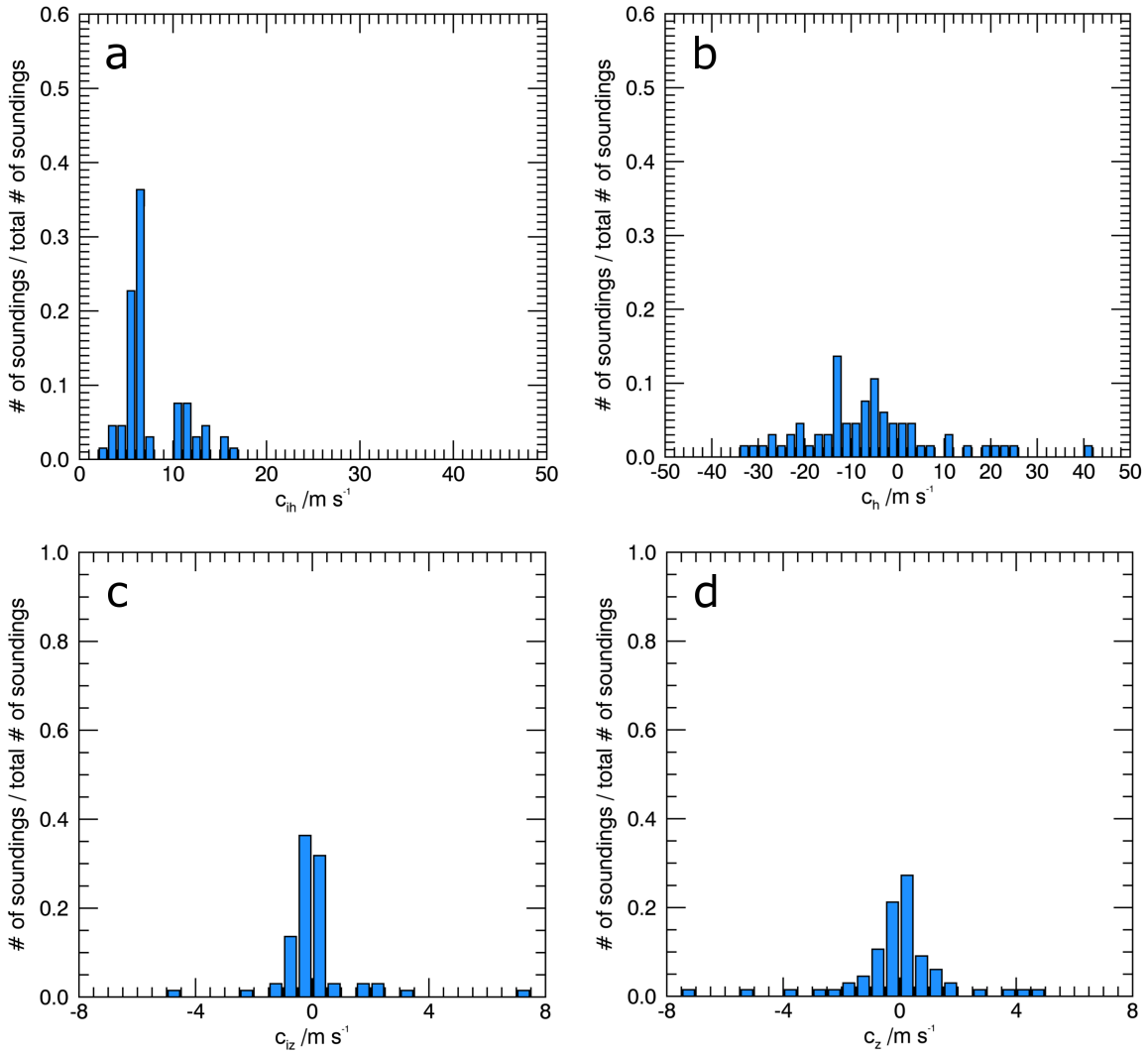

Figure A.2: Distribution of the intrinsic (left) and ground-based (right) horizontal phase speed (top) and vertical phase speed (bottom) in the troposphere for all Lauder soundings.

A.2 Non-hydrostatic MWs

Vertical wavelengths Mean values of the median vertical wavelengths for all IOPs and their distribution are shown in Fig. A.3. IOP 10 and GB 21 show the largest vertical wavelength in the troposphere due to the prevailing largest wind speed.

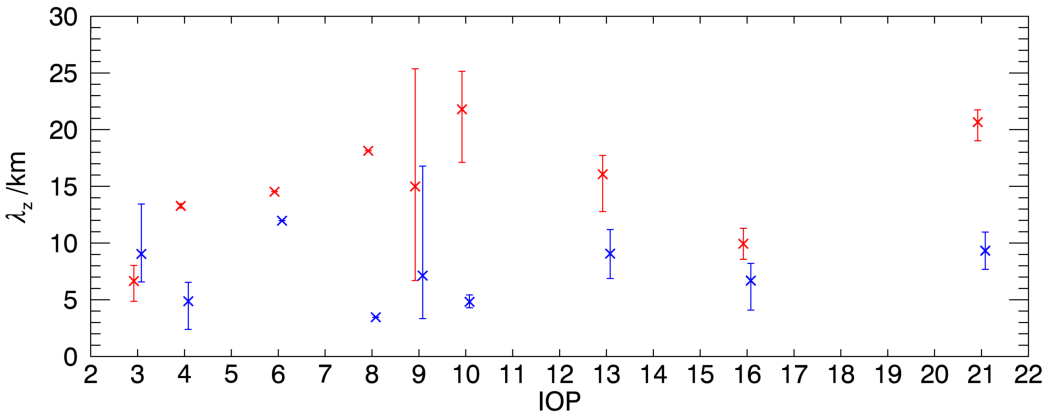

Figure A.3: Vertical wavelength (median of altitude dependent values) determined from horizontal wavelength as mean values for IOPs (x) for troposphere (red) and stratosphere (blue). Bars show the minimum and maximum values during an IOP.

Group velocity Ground-based horizontal (Fig. A.4a) and vertical (Fig. A.4b) group velocities for all IOPs. Mean values of the ground-based horizontal group velocity are about 8 and 6 m s^{-1} for troposphere and stratosphere, respectively. Similar values are found for the vertical group velocity being 9 m s^{-1} for troposhere and 7 m s^{-1} for stratosphere. Largest vertical group velocities in the troposphere were found for IOP 10 and GB 21 and in the stratosphere for IOP 6 and GB 21 (Fig. A.4b).

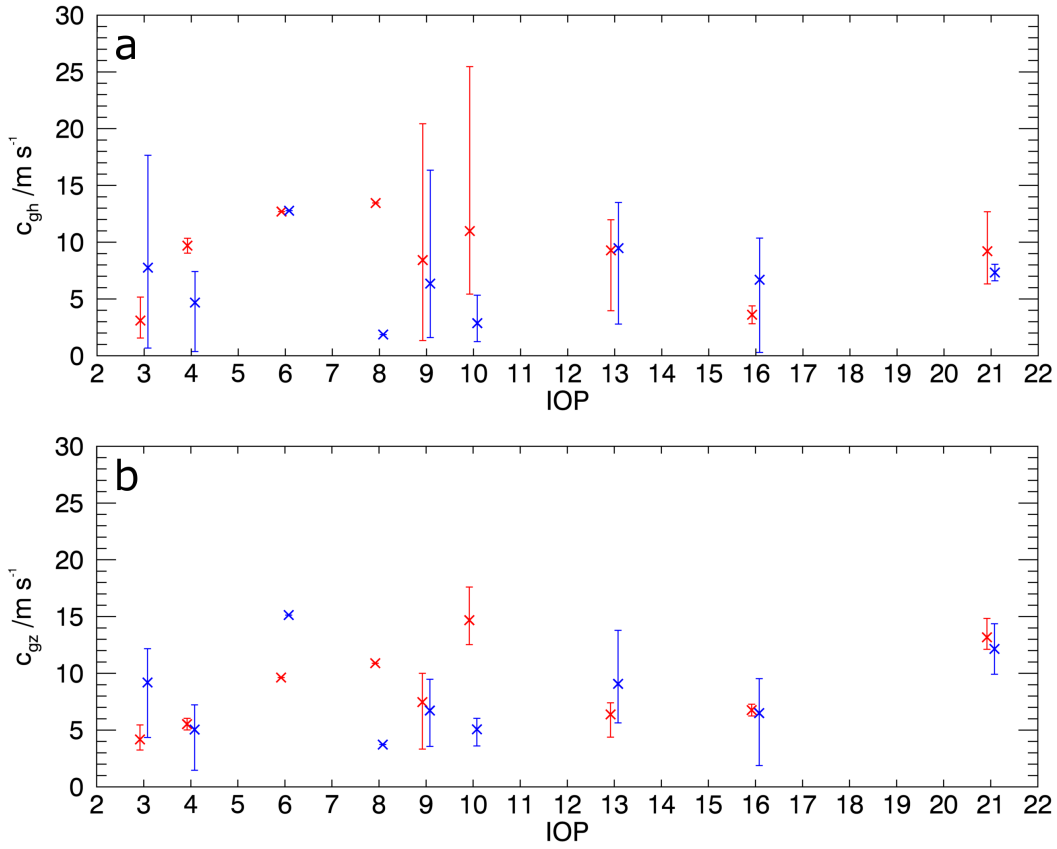

Figure A.4: Ground-based horizontal (a) and vertical (b) group velocity (median from altitude dependent values) as mean values for IOPs (x) for troposphere (red) and stratosphere (blue) for Lauder soundings. Bars show the minimum and maximum values.

Acronyms

AAO Antarctic Oscillation

ACINN Institute of Atmospheric and Cryospheric Sciences

CW convective wave

DEEPAVE Deep Propagating gravity WAVe Experiment

DLR German Aerospace Center

ECMWF European Centre for Medium-Range Weather Forecasts

EFz vertical energy fluxes

FF research flights of the DLR Falcon

FW frontal wave

GB ground-based measurements

GPS global positioning system

GV Gulfstream V

GW gravity wave

GW-LCYCLE Life Cycle of Gravity Waves

IFS Integrated Forecast System

IOP intensive observing period

JJA June/July/August

LMU Ludwig-Maximilians-University Munich

MIM Meteorological Institute Munich

MLT mesosphere and lower thermosphere

MSLP mean sea level pressure

MW mountain wave

NIWA New Zealand's National Institute of Water and Atmospheric Research

NZ New Zealand

PCC Pearson Correlation Coefficient

PF predictability flight

PFJ polar front jet stream

PSC polar stratospheric cloud

RF research flights of the NSF/NCAR GV

SAM Southern Annular Mode

SAO Semi-Annual Oscillation

SI South Island

SO Southern Ocean

SOI Southern Oscillation Index

STJ subtropical jet stream

T-REX Terrain-Induced Rotor Experiment

TIL tropopause inversion layer

TW trailing waves

UTLS upper troposphere and lower stratosphere

WRF Weather Research and Forecasting Model

Weather Regimes New Zealand

H, HNW, and W zonal group: high, high, northwest, and westerly flow

T, SW, TNW, and TSW trough group: trough, southwesterly flow, trough northwest, and trough southwest

HSE, HE, NE, HW, and R blocking group: high southeast, high east, northeasterly flow, high west, and ridge over NZ

Symbols

Sign	Description	Unit
A_θ	amplitude of potential temperature perturbation	K
A_p	amplitude of pressure perturbation	hPa
A_u	amplitude of zonal wind perturbation	m s^{-1}
A_v	amplitude of meridional wind perturbation	m s^{-1}
A_v	amplitude of vertical wind perturbation	m s^{-1}
A_H	amplitude of horizontal wind perturbation	m s^{-1}
B	buoyancy	m s^{-2}
F_i	Froude number	
H	density scale height	m
KE	horizontal GW kinetic energy	J kg^{-1}
L	mountain width	m
N	Brung-Vaisala frequency	s^{-1}
PE	GW potential energy	J kg^{-1}
R	ratio of the power of the upward propagating part of rotary spectra and the total power	
Ro	Rossby number	
Ri	Richardson number	
T'	temperature perturbation	K
T_0	background temperature	K
T	temperature	K
U_{kh}	horizontal wind speed along the direction of phase propagation	m s^{-1}
U	background zonal wind	m s^{-1}
VE	vertical component of GW kinetic energy	J kg^{-1}
V_H	horizonal wind speed	m s^{-1}
V	background meridional wind	m s^{-1}
$\overline{W}_B$	mean ascent rate of balloon	m s^{-1}
Ω	intrinsic frequency	s^{-1}
α	wind from direction	degree
ℓ	Scorer parameter	m^{-1}
ω	ground based frequency	s^{-1}
ϕ	horizontal direction of intrinsic phase propagation	degree
ρ_0	background density	kg m^{-3}

Sign	Description	Unit
θ_0	background potential temperature	K
θ	potential temperature	K
c_h	ground based horizontal phase speed	m s^{-1}
c_z	ground based vertical phase speed	m s^{-1}
c_{gh}	horizontal ground based group velocity	m s^{-1}
c_{gx}	zonal ground based group velocity	m s^{-1}
c_{gy}	meridional ground based group velocity	m s^{-1}
c_{gz}	vertical group velocity	m s^{-1}
c_{ih}	intrinsic horizontal phase speed	m s^{-1}
c_{iz}	intrinsic vertical phase speed	m s^{-1}
f	Coriolis parameter	s^{-1}
g	gravitational acceleration	m s^{-2}
h^*	non-dimensional mountain height	
h_0	mountain height	m
k_h	horizontal wavenumber	m^{-1}
k	zonal wavenumber	m^{-1}
l	meridional wavenumber	m^{-1}
m	vertical wavenumber	m^{-1}
p'	pressure perturbation	hPa
p_0	reference pressure (1000 hPa)	hPa
r	reflection coefficient	
u'	zonal wind perturbation	m s^{-1}
u_c	wind component in low level (1-3 km) direction	m s^{-1}
u	zonal wind	m s^{-1}
v'	meridional wind perturbation	m s^{-1}
v	meridional wind	m s^{-1}
w'	vertical wind perturbation with effect of density removed	m s^{-1}
w	vertical wind perturbation	m s^{-1}
z_i	altitude of inversion	m

Bibliography

Alexander, M. J., 1998: Interpretations of observed climatological patterns in stratospheric gravity wave variance. *J. Geophys. Res. Atmos.*, **103 (D8)**, 8627–8640, doi:10.1029/97JD03325.

Alexander, M. J., M. Geller, C. McLandress, S. Polavarapu, P. Preusse, F. Sassi, K. Sato, S. Eckermann, M. Ern, A. Hertzog, Y. Kawatani, M. Pulido, T. A. Shaw, M. Sigmond, R. Vincent, and S. Watanabe, 2010: Recent developments in gravity-wave effects in climate models and the global distribution of gravity-wave momentum flux from observations and models. *Quart. J. Roy. Meteorol. Soc.*, **136 (650)**, 1103–1124, doi:10.1002/qj.637.

Armi, L., and G. J. Mayr, 2015: Virtual and real topography for flows across mountain ranges. *J. Appl. Met. Clim.*, **54 (4)**, 723–731, doi:10.1175/JAMC-D-14-0231.1.

Baines, P. G., 1995: *Topographic effects in stratified flows*. 1st ed., Cambridge University Press.

Birner, T., 2006: Fine-scale structure of the extratropical tropopause region. *J. Geophys. Res. Atmos.*, **111 (D4)**, D04 104, doi:10.1029/2005JD006301.

Birner, T., A. Dörnbrack, and U. Schumann, 2002: How sharp is the tropopause at midlatitudes? *Geophys. Res. Lett.*, **29 (14)**, doi:10.1029/2002GL015142.

Bölöni, G., B. Ribstein, J. Muraschko, C. Sgoff, J. Wei, and U. Achatz, 2016: The interaction between atmospheric gravity waves and large-scale flows: An efficient description beyond the nonacceleration paradigm. *J. Atmos. Sci.*, **73 (12)**, 4833–4852, doi:10.1175/JAS-D-16-0069.1.

Bossert, K., D. C. Fritts, P.-D. Pautet, B. P. Williams, M. J. Taylor, B. Kaifler, A. Dörnbrack, I. M. Reid, D. J. Murphy, A. J. Spargo, and A. D. MacKinnon, 2015: Momentum flux estimates accompanying multiscale gravity waves over mount cook, new zealand, on 13 july 2014 during the DEEPWAVE campaign. *J. Geophys. Res. Atmos.*, **120 (18)**, 9323–9337, doi:10.1002/2015JD023197, 2015JD023197.

Bramberger, M., A. Dörnbrack, K. Bossert, B. Ehard, D. C. Fritts, B. Kaifler, C. Mallaun, A. Orr, P.-D. Pautet, M. Rapp, M. J. Taylor, S. Vosper, B. P. Williams,

and B. Witschas, 2017: Does Strong Tropospheric Forcing Cause Large-Amplitude Mesospheric Gravity Waves? A DEEPWAVE Case Study. *J. Geophys. Res. Atmos.*, **122 (21)**, 11,422–11,443, doi:10.1002/2017JD027371.

Burnett, A. W., and A. R. McNicoll, 2000: Interannual variations in the Southern Hemisphere winter circumpolar vortex: relationships with the semiannual oscillation. *J. Clim.*, **13 (5)**, 991–999, doi:10.1175/1520-0442(2000)013⟨0991:IVITSH⟩2.0.CO;2.

Chanin, M.-L., and A. Hauchecorne, 1981: Lidar observation of gravity and tidal waves in the stratosphere and mesosphere. *J. Geophys. Res. Oceans*, **86 (C10)**, 9715–9721, doi:10.1029/JC086iC10p09715.

Chouza, F., O. Reitebuch, M. Jähn, S. Rahm, and B. Weinzierl, 2016: Vertical wind retrieved by airborne lidar and analysis of island induced gravity waves in combination with numerical models and in situ particle measurements. *Atmos. Chem. Phys.*, **16 (7)**, 4675–4692, doi:10.5194/acp-16-4675-2016.

Domaradzki, J. A., Z. Xiao, and P. K. Smolarkiewicz, 2003: Effective eddy viscosities in implicit large eddy simulations of turbulent flows. *Phys. Fluids*, **15 (12)**, 3890–3893, doi:10.1063/1.1624610.

Doyle, J. D., and Q. Jiang, 2006: Observations and numerical simulations of mountain waves in the presence of directional wind shear. *Quart. J. Roy. Meteorol. Soc.*, **132 (619)**, 1877–1905, doi:10.1256/qj.05.140.

Dörnbrack, A., T. Birner, A. Fix, H. Flentje, A. Meister, H. Schmid, E. V. Browell, and M. J. Mahoney, 2002: Evidence for inertia gravity waves forming polar stratospheric clouds over scandinavia. *J. Geophys. Res. Atmos.*, **107 (D20)**, SOL 30–1–SOL 30–18, doi:10.1029/2001JD000452.

Dörnbrack, A., S. Gisinger, and B. Kaifler, 2017a: On the interpretation of gravity wave measurements by ground-based lidars. *Atmosphere*, **8 (3)**, doi:10.3390/atmos8030049.

Dörnbrack, A., S. Gisinger, M. C. Pitts, L. R. Poole, and M. Maturilli, 2017b: Multilevel cloud structures over Svalbard. *Mon. Weath. Rev.*, **145 (4)**, 1149–1159, doi:10.1175/MWR-D-16-0214.1.

Duck, T. J., J. A. Whiteway, and A. I. Carswell, 2001: The gravity wave-arctic stratospheric vortex interaction. *J. Atmos. Sci.*, **58 (23)**, 3581–3596, doi:10.1175/1520-0469(2001)058⟨3581:TGWASV⟩2.0.CO;2.

Dunkerton, T., 1978: On the Mean Meridional Mass Motions of the Stratosphere and Mesosphere. *J. Atmos. Sci.*, **35**, 2325–2333, doi:10.1175/1520-0469(1978)035⟨2325:OTMMMM⟩2.0.CO;2.

Durran, D. R., M. O. Hills, and P. N. Blossey, 2015: The Dissipation of Trapped Lee Waves. Part I: Leakage of Inviscid Waves into the Stratosphere. *J. Atmos. Sci.*, **72 (4)**, 1569–1584, doi:10.1175/JAS-D-14-0238.1.

Eckermann, S. D., 1995: Effect of background winds on vertical wavenumber spectra of atmospheric gravity waves. *J. Geophys. Res. Atmos.*, **100 (D7)**, 14 097–14 112, doi:10.1029/95JD00987.

Eckermann, S. D., 1996: Hodographic analysis of gravity waves: Relationships among stokes parameters, rotary spectra and cross-spectral methods. *J. Geophys. Res. Atmos.*, **101 (D14)**, 19 169–19 174, doi:10.1029/96JD01578.

Eckermann, S. D., J. Ma, D. L. Wu, and D. Broutman, 2007: A three-dimensional mountain wave imaged in satellite radiance throughout the stratosphere: Evidence of the effects of directional wind shear. *Quart. J. Roy. Meteorol. Soc.*, **133 (629)**, 1959–1975, doi:10.1002/qj.187.

Eckermann, S. D., and R. A. Vincent, 1989: Falling sphere observations of anisotropic gravity wave motions in the upper stratosphere over australia. *Pure Appl. Geophys.*, **130 (2)**, 509–532, doi:10.1007/BF00874472.

Eckermann, S. D., and R. A. Vincent, 1993: VHF radar observations of gravity-wave production by cold fronts over southern Australia. *J. Atmos. Sci.*, **50 (6)**, 785–806, doi:10.1175/1520-0469(1993)050⟨0785:VROOGW⟩2.0.CO;2.

Ehard, B., B. Kaifler, A. Dörnbrack, P. Preusse, S. D. Eckermann, M. Bramberger, S. Gisinger, N. Kaifler, B. Liley, J. Wagner, and M. Rapp, 2017: Horizontal propagation of large-amplitude mountain waves into the polar night jet. *J. Geophys. Res. Atmos.*, **122 (3)**, 1423–1436, doi:10.1002/2016JD025621.

Eliassen, A., and E. Palm, 1960: On the transfer of energy in stationary mountain waves. *Geofysiske Publikasjoner*, **22**, 1–23.

Elliott, J. R., and P. K. Smolarkiewicz, 2002: Eddy resolving simulations of turbulent solar convection. *Int. J. Numer. Methods Fluids*, **39 (9)**, 855–864, doi:10.1002/fld.333.

Evan, S., and M. Alexander, 2008: Intermediate-scale tropical inertia gravity waves observed during the TWP-ICE campaign. *J. Geophys. Res. Atmos.*, **113 (D14)**, D14 104, doi:10.1029/2007JD009289.

Fritts, D. C., and J. M. Alexander, 2003: Gravity wave dynamics and effects in the middle atmosphere. *Rev. Geophys.*, **41**, 1003, doi:10.1029/2001RG000106.

Fritts, D. C., and M. J. Alexander, 2012: Correction to "gravity wave dynamics and effects in the middle atmosphere". *Rev. Geophys.*, **50 (3)**, doi:10.1029/2012RG000409.

Fritts, D. C., B. Laughman, L. Wang, T. S. Lund, and R. L. Collins, 2018: Gravity Wave Dynamics in a Mesospheric Inversion Layer: 1. Reflection, Trapping, and Instability Dynamics. *J. Geophys. Res. Atmos.*, doi:10.1002/2017JD027440.

Fritts, D. C., R. B. Smith, M. J. Taylor, J. D. Doyle, S. D. Eckermann, A. Dörnbrack, M. Rapp, B. P. Williams, P.-D. Pautet, K. Bossert, and Coauthors, 2016: The Deep Propagating Gravity Wave Experiment (DEEPWAVE): An airborne and ground-based exploration of gravity wave propagation and effects from their sources throughout the lower and middle atmosphere. *Bull. Amer. Meteor. Soc.*, **97 (3)**, 425–453, doi:10.1175/BAMS-D-14-00269.1.

Gallego, D., P. Ribera, R. Garcia-Herrera, E. Hernandez, and L. Gimeno, 2005: A new look for the Southern Hemisphere jet stream. *Clim. Dyn.*, **24 (6)**, 607–621, doi:10.1007/s00382-005-0006-7.

Garcia, R. R., A. K. Smith, D. E. Kinnison, . de la Cámara, and D. J. Murphy, 2017: Modification of the Gravity Wave Parameterization in the Whole Atmosphere Community Climate Model: Motivation and Results. *J. Atmos. Sci.*, **74 (1)**, 275–291, doi:10.1175/JAS-D-16-0104.1.

Gardner, C. S., and N. F. Gardner, 1993: Measurement distortion in aircraft, space shuttle, and balloon observations of atmospheric density and temperature perturbation spectra. *J. Geophys. Res. Atmos.*, **98 (D1)**, 1023–1033, doi:10.1029/92JD02025.

Geller, M. A., and J. Gong, 2010: Gravity wave kinetic, potential, and vertical fluctuation energies as indicators of different frequency gravity waves. *J. Geophys. Res. Atmos.*, **115 (D11)**, D11 111, doi:10.1029/2009JD012266.

Georgelin, M., and F. Lott, 2001: On the transfer of momentum by trapped lee waves: Case of the IOP 3 of PYREX. *J. Atmos. Sci.*, **58 (23)**, 3563–3580, doi:10.1175/1520-0469(2001)058⟨3563:OTTOMB⟩2.0.CO;2.

Gettelman, A., P. Hoor, L. Pan, W. Randel, M. I. Hegglin, and T. Birner, 2011: The extratropical upper troposphere and lower stratosphere. *Rev. Geophys.*, **49 (3)**, RG3003, doi:10.1029/2011RG000355.

Gettelman, A., and T. Wang, 2015: Structural diagnostics of the tropopause inversion layer and its evolution. *J. Geophys. Res. Atmos.*, **120 (1)**, 46–62, doi:10.1002/2014JD021846.

Gill, A. E., 1982: *Atmosphere-Ocean Dynamics (International Geophysics Series, Volume 30) 1st Edition*. Academic Press.

Gisinger, S., A. Dörnbrack, and J. Schröttle, 2015: A modified Darcy's law. *Theor. Comput. Fluid Dyn.*, **29 (4)**, 343–347, doi:10.1007/s00162-015-0357-6.

Gisinger, S., A. Dörnbrack, V. Matthias, J. D. Doyle, S. D. Eckermann, B. Ehard, L. Hoffmann, B. Kaifler, C. G. Kruse, and M. Rapp, 2017: Atmospheric conditions during the deep propagating gravity wave experiment (DEEPWAVE). *Mon. Weath. Rev.*, **145 (10)**, 4249–4275, doi:10.1175/MWR-D-16-0435.1.

Gong, D., and S. Wang, 1999: Definition of Antarctic Oscillation Index. *Geophys. Res. Lett.*, **26 (4)**, 459–462, doi:10.1029/1999GL900003.

Gong, J., and M. A. Geller, 2010: Vertical fluctuation energy in united states high vertical resolution radiosonde data as an indicator of convective gravity wave sources. *J. Geophys. Res. Atmos.*, **115 (D11)**, D11 110, doi:10.1029/2009JD012265.

Gordon, N. D., 1986: The southern oscillation and new zealand weather. *Mon. Weath. Rev.*, **114 (2)**, 371–387, doi:10.1175/1520-0493(1986)114⟨0371:TSOANZ⟩2.0.CO;2.

GRAW, 2011: Graw brochure. http://figtree.us.com/pdfs/Graw_Brochure_2011.pdf, last access: 6 September 2017.

Grise, K. M., D. W. Thompson, and T. Birner, 2010: A global survey of static stability in the stratosphere and upper troposphere. *J. Clim.*, **23 (9)**, 2275–2292, doi:10.1175/2009JCLI3369.1.

Grubišić, V., and P. K. Smolarkiewicz, 1997: The effect of critical levels on 3D orographic flows: Linear regime. *J. Atmos. Sci.*, **54 (15)**, 1943–1960, doi:10.1175/1520-0469(1997)054⟨1943:TEOCLO⟩2.0.CO;2.

Grubišić, V., J. D. Doyle, J. Kuettner, R. Dirks, S. A. Cohn, L. L. Pan, S. Mobbs, R. B. Smith, C. D. Whiteman, S. Czyzyk, S. Vosper, M. Weissmann, S. Haimov, S. F. J. D. Wekker, and F. K. Chow, 2008: The Terrain-Induced Rotor Experiment. *Bull. Amer. Meteor. Soc.*, **89 (10)**, 1513–1533, doi:10.1175/2008BAMS2487.1.

Guest, F. M., M. J. Reeder, C. J. Marks, and D. J. Karoly, 2000: Inertia-gravity waves observed in the lower stratosphere over Macquarie Island. *J. Atmos. Sci.*, **57 (5)**, 737–752, doi:10.1175/1520-0469(2000)057⟨0737:IGWOIT⟩2.0.CO;2.

Hines, C. O., 1960: Internal atmospheric gravity waves at ionospheric heights. *Can. J. Phys.*, **38 (11)**, 1441–1481, doi:10.1139/p60-150.

Hoffmann, L., A. W. Grimsdell, and M. J. Alexander, 2016: Stratospheric gravity waves at Southern Hemisphere orographic hotspots: 2003–2014 AIRS/Aqua observations. *Atmos. Chem. Phys.*, **16**, 9381–9397, doi:10.5194/acp-16-9381-2016.

Jiang, J. H., S. D. Eckermann, D. L. Wu, and D. Y. Wang, 2006: Inter-annual variation of gravity waves in the arctic and antarctic winter middle atmosphere. *Adv. Space Res.*, **38 (11)**, 2418–2423, doi:10.1016/j.asr.2005.09.036.

Kaifler, B., N. Kaifler, B. Ehard, A. Dörnbrack, M. Rapp, and D. C. Fritts, 2015: Influences of source conditions on mountain wave penetration into the stratosphere and mesosphere. *Geophys. Res. Lett.*, **42 (21)**, 9488–9494, doi:10.1002/2015GL066465.

Kaifler, N., B. Kaifler, B. Ehard, S. Gisinger, A. Dörnbrack, M. Rapp, R. Kivi, A. Kozlovsky, M. Lester, and B. Liley, 2017: Observational indications of downward-propagating gravity waves in middle atmosphere lidar data. *Journal of Atmospheric and Solar-Terrestrial Physics*, **162**, 16 – 27, doi:10.1016/j.jastp.2017.03.003.

Keller, T. L., 1994: Implications of the hydrostatic assumption on atmospheric gravity waves. *J. Atmos. Sci.*, **51 (13)**, 1915–1929, doi:10.1175/1520-0469(1994)051⟨1915:IOTHAO⟩2.0.CO;2.

Kidson, J. W., 2000: An analysis of new zealand synoptic types and their use in defining weather regimes. *Int. J. Climatol.*, **20 (3)**, 299–316, doi:10.1002/(SICI)1097-0088(20000315)20:3⟨299::AID-JOC474⟩3.0.CO;2-B.

Kruse, C. G., and R. B. Smith, 2015: Gravity wave diagnostics and characteristics in mesoscale fields. *J. Atmos. Sci.*, **72 (11)**, 4372–4392, doi:10.1175/JAS-D-15-0079.1.

Kruse, C. G., R. B. Smith, and S. D. Eckermann, 2016: The midlatitude lower-stratospheric mountain wave "valve layer". *J. Atmos. Sci.*, **73 (12)**, 5081–5100, doi:10.1175/JAS-D-16-0173.1.

Küttner, J., 1938: Moazagotl und föhnwelle. *Beitr. Phys. fr. Atmosa*, **25**, 79–114.

Lane, T. P., M. J. Reeder, and F. M. Guest, 2003: Convectively generated gravity waves observed from radiosonde data taken during MCTEX. *Quart. J. Roy. Meteorol. Soc.*, **129 (590)**, 1731–1740, doi:10.1256/qj.02.196.

Lane, T. P., M. J. Reeder, B. R. Morton, and T. L. Clark, 2000: Observations and numerical modelling of mountain waves over the Southern Alps of New Zealand. *Quart. J. Roy. Meteorol. Soc.*, **126 (569)**, 2765–2788, doi:10.1002/qj.49712656909.

Lin, Y., 2007: *Mesoscale Dynamics*. Cambridge University Press.

Lindzen, R. S., 1981: Turbulence and stress owing to gravity-wave and tidal breakdown. *J. Geophys. Res. Atmos.*, **86**, 9707–9714, doi:10.1029/JC086iC10p09707.

Manney, G. L., M. I. Hegglin, W. H. Daffer, M. J. Schwartz, M. L. Santee, and S. Pawson, 2014: Climatology of upper tropospheric–lower stratospheric (UTLS) jets and tropopauses in MERRA. *J. Clim.*, **27 (9)**, 3248–3271, doi:10.1175/JCLI-D-13-00243.1.

McLandress, C., and J. F. Scinocca, 2005: The GCM Response to Current Parameterizations of Nonorographic Gravity Wave Drag. *J. Atmos. Sci.*, **62 (7)**, 2394–2413, doi:10.1175/JAS3483.1.

Moffat-Griffin, T., and S. R. Colwell, 2017: The characteristics of the lower stratospheric gravity wavefield above halley (75°S, 26°W), antarctica, from radiosonde observations. *J. Geophys. Res. Atmos.*, **122 (17)**, 8998–9010, doi:10.1002/2017JD027079.

Moffat-Griffin, T., R. E. Hibbins, M. J. Jarvis, and S. R. Colwell, 2011: Seasonal variations of gravity wave activity in the lower stratosphere over an Antarctic Peninsula station. *J. Geophys. Res. Atmos.*, **116 (D14)**, D14 111, doi:10.1029/2010JD015349.

Murphy, D., S. Alexander, A. Klekociuk, P. Love, and R. Vincent, 2014: Radiosonde observations of gravity waves in the lower stratosphere over Davis, Antarctica. *J. Geophys. Res. Atmos.*, **119 (21)**, 11,973–11,996, doi:10.1002/2014JD022448.

Nappo, C. J., 2012: *An introduction to atmospheric gravity waves*. 2nd ed., Academic Press.

Nastrom, G. D., and D. C. Fritts, 1992: Sources of mesoscale variability of gravity waves. Part I: Topographic excitation. *J. Atmos. Sci.*, **49 (2)**, 101–110, doi:10.1175/1520-0469(1992)049⟨0101:SOMVOG⟩2.0.CO;2.

Pautet, P.-D., M. J. Taylor, D. C. Fritts, K. Bossert, B. P. Williams, D. Broutman, J. Ma, S. D. Eckermann, and J. D. Doyle, 2016: Large-amplitude mesospheric response to an orographic wave generated over the Southern Ocean Auckland Islands (50.7s) during the DEEPWAVE project. *J. Geophys. Res. Atmos.*, **121 (4)**, 1431–1441, doi:10.1002/2015JD024336.

Pfenninger, M., A. Z. Liu, G. C. Papen, and C. S. Gardner, 1999: Gravity wave characteristics in the lower atmosphere at south pole. *J. Geophys. Res. Atmos.*, **104 (D6)**, 5963–5984, doi:10.1029/98JD02705.

Plougonven, R., and F. Zhang, 2014: Internal gravity waves from atmospheric jets and fronts. *Rev. Geophys.*, **52**, 33–76, doi:10.1002/2012RG000419.

Portele, T. C., A. Dörnbrack, J. S. Wagner, S. Gisinger, B. Ehard, P.-D. Pautet, and M. Rapp, 2018: Mountain Wave Propagation under Transient Tropospheric Forcing – A DEEPWAVE Case Study. *Mon. Weath. Rev.*, doi:10.1175/MWR-D-17-0080.1, in press.

Prusa, J. M., P. K. Smolarkiewicz, and R. R. Garcia, 1996: Propagation and breaking at high altitudes of gravity waves excited by tropospheric forcing. *J. Atmos. Sci.*, **53 (15)**, 2186–2216, doi:10.1175/1520-0469(1996)053⟨2186:PABAHA⟩2.0.CO;2.

Prusa, J. M., P. K. Smolarkiewicz, and A. A. Wyszogrodzki, 2008: EULAG, a computational model for multiscale flows. *Computers & Fluids*, **37 (9)**, 1193 – 1207, doi:10.1016/j.compfluid.2007.12.001.

Queney, P., 1948: The problem of air flow over mountains:{A} summary of theoretical studies. *Bull. Am. Meteorol. Soc.*, **29**, 16–26.

Ralph, F. M., P. J. Neiman, T. L. Keller, D. Levinson, and L. Fedor, 1997: Observations, simulations, and analysis of nonstationary trapped lee waves. *J. Atmos. Sci.*, **54 (10)**, 1308–1333, doi:10.1175/1520-0469(1997)054⟨1308:OSAAON⟩2.0.CO;2.

Rapp, M., F.-J. Lübken, A. Müllemann, G. E. Thomas, and E. J. Jensen, 2002: Small-scale temperature variations in the vicinity of nlc: Experimental and model results. *J. Geophys. Res. Atmos.*, **107 (D19)**, 4392, doi:10.1029/2001JD001241.

Reeder, M. J., N. Adams, and T. P. Lane, 1999: Radiosonde observations of partially trapped lee waves over Tasmania, Australia. *J. Geophys. Res. Atmos.*, **104 (D14)**, 16 719–16 727, doi:10.1029/1999JD900038.

Renwick, J. A., 2011: Kidson's synoptic weather types and surface climate variability over new zealand. *Weather and Climate*, **31**, 3–23.

Sachsperger, J., S. Serafin, and V. Grubišić, 2015: Lee waves on the boundary-layer inversion and their dependence on free-atmospheric stability. *Front. Earth Sci.*, **3**, 70, doi:10.3389/feart.2015.00070.

Sato, K., S. Watanabe, Y. Kawatani, Y. Tomikawa, K. Miyazaki, and M. Takahashi, 2009: On the origins of mesospheric gravity waves. *Geophys. Res. Lett.*, **36 (19)**, L19 801, doi:10.1029/2009GL039908.

Schmidt, T., A. de la Torre, and J. Wickert, 2008: Global gravity wave activity in the tropopause region from CHAMP radio occultation data. *Geophys. Res. Lett.*, **35 (16)**, L16 807, doi:10.1029/2008GL034986.

Scorer, R., 1949: Theory of waves in the lee of mountains. *Quart. J. Roy. Meteorol. Soc.*, **75 (323)**, 41–56.

Serafimovich, A., C. Zülicke, P. Hoffmann, D. Peters, P. Dalin, and W. Singer, 2006: Inertia gravity waves in the upper troposphere during the MaCWAVE winter campaign - part ii: Radar investigations and modelling studies. *Ann. Geophys.*, **24 (11)**, 2863–2875, doi:10.5194/angeo-24-2863-2006.

Sharman, R., S. Trier, T. Lane, and J. Doyle, 2012: Sources and dynamics of turbulence in the upper troposphere and lower stratosphere: A review. *Geophys. Res. Lett.*, **39 (12)**, doi:10.1029/2012GL051996.

Shibuya, R., K. Sato, Y. Tomikawa, M. Tsutsumi, and T. Sato, 2015: A study of multiple tropopause structures caused by inertia–gravity waves in the antarctic. *J. Atmos. Sci.*, **72 (5)**, 2109–2130, doi:10.1175/JAS-D-14-0228.1.

Smith, R. B., 1979: The influence of mountains on the atmosphere. *Adv. Geophys.*, **21**, 87–230, doi:10.1016/S0065-2687(08)60262-9.

Smith, R. B., and C. G. Kruse, 2017: Broad-spectrum mountain waves. *J. Atmos. Sci.*, **74 (5)**, 1381–1402, doi:10.1175/JAS-D-16-0297.1.

Smith, R. B., B. K. Woods, J. Jensen, W. A. Cooper, J. D. Doyle, Q. Jiang, and V. Grubišić, 2008: Mountain waves entering the stratosphere. *J. Atmos. Sci.*, **65 (8)**, 2543–2562, doi:10.1175/2007JAS2598.1.

Smith, R. B., A. D. Nugent, C. G. Kruse, D. C. Fritts, J. D. Doyle, S. D. Eckermann, M. J. Taylor, A. Dörnbrack, M. Uddstrom, W. Cooper, P. Romashkin, J. Jensen, and S. Beaton, 2016: Stratospheric gravity wave fluxes and scales during DEEPWAVE. *J. Atmos. Sci.*, **73 (7)**, 2851–2869, doi:10.1175/JAS-D-15-0324.1.

Smolarkiewicz, P. K., L. G. Margolin, and A. A. Wyszogrodzki, 2001: A Class of Nonhydrostatic Global Models. *Journal of the Atmospheric Sciences*, **58 (4)**, 349–364, doi:10.1175/1520-0469(2001)058⟨0349:ACONGM⟩2.0.CO;2.

Spiga, A., H. Teitelbaum, and V. Zeitlin, 2008: Identification of the sources of inertia-gravity waves in the andes cordillera region. *Ann. Geophys.*, **26 (9)**, 2551–2568, doi:10.5194/angeo-26-2551-2008.

Sutherland, B. R., 2010: *Internal Gravity Waves 1st Edition*. Cambridge University Press.

Trenberth, K. E., 1986: The signature of a blocking episode on the general circulation in the Southern Hemisphere. *J. Atmos. Sci.*, **43 (19)**, 2061–2069, doi:10.1175/1520-0469(1986)043⟨2061:TSOABE⟩2.0.CO;2.

Vadas, S. L., D. C. Fritts, and M. J. Alexander, 2003: Mechanism for the generation of secondary waves in wave breaking regions. *J. Atmos. Sci.*, **60 (1)**, 194–214, doi:10.1175/1520-0469(2003)060⟨0194:MFTGOS⟩2.0.CO;2.

VAISALA, 2013: VAISALA Radiosonde RS92-SGP, data sheet. http://www.vaisala.com/VaisalaDocuments/BrochuresandDatasheets/RS92SGP-Datasheet-B210358EN-F-LOW.pdf, last access: 6 September 2017.

Vincent, R., 1984: Gravity-wave motions in the mesosphere. *Journal of atmospheric and terrestrial physics*, **46 (2)**, 119–128, doi:10.1016/0021-9169(84)90137-5.

Vincent, R. A., and J. M. Alexander, 2000: Gravity waves in the tropical lower stratosphere: An observational study of seasonal and interannual variability. *J. Geophys. Res. Atmos.*, **105 (D14)**, 17 971–17 982, doi:10.1029/2000JD900196.

Vincent, R. A., S. J. Allen, and S. D. Eckermann, 1997: Gravity-wave parameters in the lower stratosphere. *Gravity Wave Processes*, K. Hamilton, Ed., Springer Berlin Heidelberg, Berlin, Heidelberg, 7–25, doi:10.1007/978-3-642-60654-0_2.

Vosper, S., 2004: Inversion effects on mountain lee waves. *Quart. J. Roy. Meteorol. Soc.*, **130 (600)**, 1723–1748, doi:10.1256/qj.03.63.

Wagner, J., A. Dörnbrack, M. Rapp, S. Gisinger, B. Ehard, M. Bramberger, B. Witschas, F. Chouza, S. Rahm, C. Mallaun, G. Baumgarten, and P. Hoor, 2017: Observed versus simulated mountain waves over Scandinavia – improvement of vertical winds, energy and momentum fluxes by enhanced model resolution? *Atmos. Chem. Phys.*, **17 (6)**, 4031–4052, doi:10.5194/acp-17-4031-2017.

Wallace, J. M., and P. V. Hobbs, 2006: *Atmospheric science: an introductory survey*, Vol. 92. Academic press.

Weinstock, J., 1996: Gravity wave activity at various latitudes and heights in the middle atmosphere. *Adv. Space Res.*, **17 (11)**, 57 – 66, doi:10.1016/0273-1177(95)00730-3.

Wirth, V., 2003: Static stability in the extratropical tropopause region. *J. Atmos. Sci.*, **60 (11)**, 1395–1409, doi:10.1175/1520-0469(2003)060⟨1395:SSITET⟩2.0.CO;2.

Wirth, V., 2004: A dynamical mechanism for tropopause sharpening. *Meteorol. Z.*, **13 (6)**, 477–484, doi:10.1127/0941-2948/2004/0013-0477.

Witschas, B., S. Rahm, A. Dörnbrack, J. Wagner, and M. Rapp, 2017: Airborne wind lidar measurements of vertical and horizontal winds for the investigation of orographically induced gravity waves. *J. Atmospheric Ocean. Technol.*, **34 (6)**, 1371–1386, doi:10.1175/JTECH-D-17-0021.1.

WMO, 1957: Meteorology - a three-dimensional science. *WMO Bull.*, **6**, 134–138, https://library.wmo.int/pmb_ged/bulletin_6-4_en.pdf.

Woods, B. K., and R. B. Smith, 2010: Energy flux and wavelet diagnostics of secondary mountain waves. *J. Atmos. Sci.*, **67 (11)**, 3721–3738, doi:10.1175/2009JAS3285.1.

Wurtele, M., R. Sharman, and A. Datta, 1996: Atmospheric lee waves. *Annu. Rev. Fluid Mech.*, **28 (1)**, 429–476, doi:10.1146/annurev.fl.28.010196.002241.

Wurtele, M., R. Sharman, and T. Keller, 1987: Analysis and simulations of a troposphere–stratosphere gravity wave model. Part I. *J. Atmos. Sci.*, **44 (21)**, 3269–3281, doi:10.1175/1520-0469(1987)044⟨3269:AASOAT⟩2.0.CO;2.

Wyszogrodzki, A. A., and P. K. Smolarkiewicz, 2010: Large-eddy simulation of urban flows: Porous-media analogy. *ASME 2010 3rd Joint US-European Fluids Engineering Summer Meeting: Volume 1, Symposia – Parts A, B, and C*, 2339–2346, doi:10.1115/FEDSM-ICNMM2010-30157.

Yoshiki, M., N. Kizu, and K. Sato, 2004: Energy enhancements of gravity waves in the antarctic lower stratosphere associated with variations in the polar vortex and tropospheric disturbances. *J. Geophys. Res. Atmos.*, **109 (D23)**, D23 104, doi:10.1029/2004JD004870.

Yoshiki, M., and K. Sato, 2000: A statistical study of gravity waves in the polar regions based on operational radiosonde data. *J. Geophys. Res. Atmos.*, **105 (D14)**, 17 995–18 011, doi:10.1029/2000JD900204.

Zhang, F., S. Wang, and R. Plougonven, 2004: Uncertainties in using the hodograph method to retrieve gravity wave characteristics from individual soundings. *Geophys. Res. Lett.*, **31 (11)**, L11 110, doi:10.1029/2004GL019841.

Zink, F., and R. A. Vincent, 2001: Wavelet analysis of stratospheric gravity wave packets over Macquarie Island: 1. Wave parameters. *J. Geophys. Res. Atmos.*, **106 (D10)**, 10 275–10 288, doi:10.1029/2000JD900847.

Danksagung

Hiermit möchte ich mich bei allen bedanken, die mir während meiner Promotion und Tätigkeit am DLR-IPA mit Rat und Tat zur Seite gestanden haben. Insbesondere bedanke ich mich bei meinen Betreuern Prof. Markus Rapp und Dr. Andreas Dörnbrack für ihr Interesse an der Arbeit, für die konstruktiven Diskussionen und für die abwechslungsreiche Zeit während der Promotion. Durch alle Abteilungen hindurch danke ich den Kolleginnen und Kollegen am IPA für die gute Stimmung, egal ob im Alltag, während der Kampagnen oder in der Freizeit. Ich danke Dr. Philipp Jeßberger und Dr. Henrike Wilms für ihre Anmerkungen zur ersten Rohfassung dieser Doktorarbeit. Schließlich möchte ich mich auch noch bei meiner Familie und meinen Freunden bedanken, die mich in den letzten Jahren unterstützt und motiviert haben.

Diese Arbeit entstand im Rahmen der Deutschen Forschungsinitiative “Role of the Middle Atmosphere in Climate” (ROMIC/01LG1206A) des BMBF und der DFG Forschergruppe MultiScale Dynamics of Gravity Waves (MS-GWaves, GW-TP/DO 1020/9-1).